WHOI-84-20

Dynamic Response of Electromagnetic Current Meters

by

David G. Aubrey, Wayne D. Spencer

Woods Hole Oceanographic Institution
Woods Hole, Massachusetts

John H. Trowbridge

University of Delaware
Newark, Delaware

June 1984

Technical Report

Approved for Distribution: R. Heirtzler (Acting Chairman)

Richard P. von Herzen, Chairman
Department of Geology & Geophysics

William D. Grant, Acting Director
Coastal Research Center

TABLE OF CONTENTS

SUMMARY

The dynamic response of electromagnetic current meters (manufactured by Marsh-McBirney, Inc.) has been clarified through a comprehensive laboratory measurement program combined with a thorough literature review. Elucidation of the behavior of these flowmeters under a variety of dynamic conditions has been neglected in the past. Since flow past a spherical body has considerable hydrodynamic complexity for different dynamic conditions, a careful laboratory study was carried out for pure steady, pure oscillatory (horizontal plane), and combined steady/oscillatory conditions at two test facilities. Test results indicate that flowmeter behavior under pure steady flow is excellent in the absence of high levels of free-stream turbulence, with an r.m.s. error of 1-5 cm/sec. These errors could be reduced with a higher-order polynomial regression fit. Pure oscillatory response was also excellent, with r.m.s. errors of 1-2 cm/sec, and sensitivity which is correlated with the oscillatory Reynolds number, $(Re)_o$, and the Keulegan-Carpenter number, (A/d). Combined steady/ oscillatory flows degraded current meter performance with larger residual errors (1-6 cm/sec) and significant differences in sensitivity (up to $20°/°$). Horizontal cosine response showed systematic deviations from pure cosine behavior, with a notable inter-cardinal undersensitivity and cosine "shoulder" at lower Reynolds numbers. Error analysis shows these current sensors are adequate for many kinematic measurements, but may lead to excessive errors when using velocity to calculate dynamical quantities (such as bottom friction, Reynolds Stress, or log-layer friction velocities). A careful error analysis must precede any use of these meters for estimating dynamical quantities. These studies pointed out a potential difficulty in using these meters in areas of large ambient turbulence levels ($20°/°$ turbulent intensities), which are characteristic of many near-bottom shallow water environments. Further study is needed to clarify this behavior.

INTRODUCTION

Field investigations of sediment transport in the nearshore zone have been hampered by the inability to make representative, quantitative measurements of sand transport in situ. This deficiency has been recognized and is being rectified with introduction of a variety of acoustic and optical devices designed to estimate particle flux in this nearshore zone. Once these devices are built, point measurements of flux must be extrapolated to estimate spatially- and temporally-averaged fluxes. Besides these direct measurement techniques, which are still in the development stage, there are a number of alternative methods for estimating nearshore sediment transport. Net transport is often inferred from beach profile analysis, where the difference between beach states is defined, but not the pathways for that change. Net transport is sometimes derived from measurements of sediment accumulation at sediment traps, structures designed to inhibit longshore sand transport locally. Finally, sediment transport is often derived by linking a sediment transport theory or empirical relationship with in situ measurements of fluid kinematical quantities. Common kinematic parameters measured include bottom pressure and water velocities. The derived transport values then depend on two possible sources of error: the inaccuracies in the measurement technique, and the shortcomings of the theoretical/empirical transport model.

Major studies such as the Nearshore Sediment Transport Study (NSTS), the field programs of the Coastal Engineering Research Center (CERC), and the upcoming Coastal Canadian Sediment Study (C^2S^2), all rely to some degree on the estimation of nearshore sediment transport using data derived from current meters and applied to some transport model, or used to verify or establish a new transport model. Besides the use of current data in sediment transport

2

models, flow data is also used to field test models of surf zone hydrodynamics, whereby kinematic quantities are used to estimate dynamical terms in the momentum equation. Examples of terms commonly calculated are advective terms ($u \frac{\partial u}{\partial x}$), frictional terms (f $u | u |$), and higher order moments of the velocity ($< u^3 >$).

Concern with current meter calibrations was motivated by an examination of the NSTS experimental data from Santa Barbara, CA, held in February 1980, in which the higher-order velocity moments from current meter measurements showed a time-variability not in keeping with time scales of change of the forcing conditions (e.g., wave groupiness), and by field studies which have shown a persistent offshore near-bottom flow which is not satisfactorily explained by nearshore circulation theories. Because of the importance of these quasi-steady flows and higher order velocity moments on sediment transport in the nearshore zone, a concern developed that measurement errors may introduce biases and aliases into the data which must be removed, especially for sediment transport modeling. A review of the literature on electromagnetic current meter (emcm) calibrations showed no thorough studies of the response of emcm's to combined steady and oscillatory flows, although some studies emphasizing various elements of this calibration have been performed (e.g., Appell, 1977; Cunningham, Guza and Lowe, 1979). The present study was designed to evaluate under carefully controlled laboratory conditions the response of emcm's typically used in the field for nearshore sediment transport studies to combined wave and current flows.

Current meter calibration can take place either in the field or laboratory. Field calibration requires a standard against which to intercalibrate; such an instrument does not exist yet which covers the dynamic range and broadband

3

spectrum required by such an instrument. Acoustic travel time current meters (e.g., Williams and Tochko, 1977) may provide such a standard in the future, but must be subjected to the same vigorous tests used in this study. The range of dynamic calibration conditions required to isolate the response of the flow meter to any particular dynamical forcing is difficult to achieve in the field. The alternative is to use a laboratory calibration, which does not have the same limitations as the field calibration. Laboratory calibrations can be performed under repeatable conditions, spanning the dynamic range of many dynamical variables of interest. Steady, oscillatory, and combined steady/oscillatory conditions can all be readily implemented in the laboratory. Laboratory conditions permit accurate measurement of the induced motion near the current meter (whether through towing or in a flume mode), so reliance on a standard velocity sensing instrument (which may differ in response time, averaging volume, etc.) is not necessary. Disadvantages of laboratory calibration exist, but in general are overidden by their advantages.

One disadvantage of laboratory calibration of the EMCM is the difference in ambient turbulence scales and intensities between the lab and field. If Reynold's and Strouhal effects are important to instrument calibration, then the ambient turbulent scales and intensities experienced in the field must be reproduced in the laboratory. If instrument calibration depends too critically on turbulent scales and intensities, then field use of the instruments would be questionable, given the variability in turbulent scales and intensity. For instance, in a rough turbulent flow the dominant turbulent scale varies with distance above the bottom boundary. Since flow meters are often employed at different (and varying) distances above the bed, extraction of useful velocity data in such a situation would be difficult. Because of this, we elected to calibrate the current sensors in a controlled laboratory environ-

4

ment, which represents the most noise-free situation (hydrodynamically) of any possible use of these meters. Field behavior would be at best as good as the laboratory behavior, and probably would be degraded somewhat. Laboratories can be difficult environments for calibration of emcm's because of electrical noise. Noise reduction in many labs is a matter of carefully grounding instruments, the water tank, and power sources. In order to achieve meaningful calibration results, the environment must be as free as possible from electrical and hydrodynamic noise.

In a preliminary effort to investigate the influence of scales and intensities of turbulence, one current sensor was towed behind screens with known grid density and thickness, which generated varying scales and intensities of turbulence. Results from this experiment provide some guidance for assessing this calibration-dependence on turbulent scales and intensities.

All current meters calibrated were electromagnetic, relying on Faraday's Law to obtain relative velocity information through use of a fluctuating magnetic field. All instruments were two-axis, with either a 0.040 m (1.6") or 0.105 m (4") diameter sphere, made by Marsh-McBirney, Inc., of Maryland. These instruments were chosen because they are frequently encountered surf zone measurement tools. All calibrations were performed by towing or oscillating the current sensor through the water column, instead of operating in a flume mode with associated boundary layer structures (sidewall and bottom effects). As discussed in a later section, all instruments were calibrated at one of two locations (Woods Hole Oceanographic Institution or Massachusetts Institute of Technology).

This report has adopted the following conventions for terminology dealing with calibration results:

sensitivity - A quantity relating the induced voltage from an EM sensor (dependent variable) to a tow speed or other dynamical grouping (independent variable). Sensitivity has units of volts/m/sec, and relates the response of the sensor to varying hydrodynamic flow fields.

gain - The inverse of sensitivity, with units of m/sec/volt. This quantity is used in reduction of field data, multiplied by the observed voltage to obtain a velocity estimate.

electronic offset - Current meter output at zero flow rate, with meter immersed in water.

numerical offset - An output of the regression equation, the numerical offset is the y-axis intercept for the linear regression of voltage versus velocity (or other dynamical quantity) when electronic offset has been subtracted. For a perfectly linear sensor, this numerical offset should be zero.

PREVIOUS WORK

Previous literature discussing application of Faraday's law to measurement of fluid flow dates back to more than a century, particularly with application to the gaging of ships' speeds. Williams (1930) was among the first to apply the technique to measurement of flow through an enclosed pipe. Since that time, many applications of the principle of electromagnetic induction have been introduced, to the point that measurement of fluid flows on many scales is accomplished routinely using instruments based on this principle. Measurement of flows in the ocean, under a variety of different conditions, represents one of these many applications. With every application, there is a desire to

6

relate the induced electric potential to some parameter of the flow field, generally fluid velocity or mass flux. This requires a knowledge of the physics of the flow sensor, as well as a careful laboratory evaluation of the instrument. In this review of previous work, we discuss part of the voluminous literature covering the theory and calibration of electromagnetic flow sensors, omitting some articles for sake of brevity. Almost every user of electromagnetic flow sensors has performed some cursory calibrations of these sensors, which generally remain unpublished and at best vaguely referenced in a 'methods' section of a scientific publication. The following discussion centers on articles culled from the scientific and grey (technical) literature.

The operating principle for electromagnetic current meters is described by the equation (McCullough, 1974):

$$E = \int (\underline{U} \times \underline{B} - \underline{J}/\sigma) \cdot d\underline{\ell}$$

where E is the induced voltage produced by the vector cross product of the velocity vector $\underline{U}$ and the magnetic field $\underline{B}$. If either the velocity or magnetic field is non-uniform, then currents $\underline{J}$ flow in the conductive medium (conductivity $= \sigma$) so as to reduce the induced emf $\underline{E}$ along the pathlength $d\underline{\ell}$. Thus the signal voltage depends not only on the local vector velocity but also on the local electric current density $\underline{J}$, whose source may be dependent or independent on $\underline{U}$ and $\underline{B}$. Those ambient currents associated with a local test facility may degrade calibrations, and must therefore be eliminated from calibration facilities.

Guelke (1944) discussed an electromagnetic device used to measure the velocity of currents in the sea. The instrument consisted of a flat circular coil carrying an electric current, deployed on the sea bottom. Flow through the resulting magnetic field induced an electric potential measured by electrodes placed in the fluid. Based on this report, Longuet-Higgins and Barber

7

(1946) presented a theoretical analysis of the properties of electromagnetic flow meters. They discuss the effect of different sensor geometries, the effect of mounting an instrument near a sea-bed or other medium of different electrical conductivity, and the effect of velocity shear on the measurements. They propose the use of insulators on the sensor adjacent to the electrodes to magnify the sensitivity of the instrument, defining sensitivity as the ratio of the greatest electric potential difference observable in the water to the velocity of the water in the far field (outside the boundary layer surrounding the measuring device). Electrodes are recommended to be placed on the surface of an insulating sheath. Alternating current driving the coils is recommended to minimize the effects of local steady (DC) electric fields. Symmetry in the instrument is suggested to minimize measurement bias due to varying horizontal angles of attack of the current relative to the sensor. Two mutually orthogonal pairs of electrodes were suggested to measure both components of flow in the plane of the electrodes. The error induced by placing the sensor close to the sea bed is greatest when the sea-bed is a good conductor compared to the water; the error is least when the sea-bed is a relatively good insulator. Thus a conducting sea-bed reduces the sensitivity of the sensor, while an insulating sea-bed increases the sensitivity. This error will be not much greater than 1 percent when the sensor is more than one sensor diameter away from the sea-bed. Shear in the water column can produce a change in sensitivity as well. If the velocity varies linearly with height, this error is zero due to the antisymmetry of the velocity deviation from the mean stream. For specified conditions of shearing flow near a sea-bed, the error due to shearing motion is less than 10 percent if the sensor is more than a diameter away from the bed. Errors due to other velocity distributions can be calculated from formulae provided in this article. Longuet-Higgins and

8

Barber (1946) contend a spherical sensor "is unlikely to be of much practical use first because of the turbulence and instability, in fact, of the waterflow round a sphere, and second ...". Prolate and oblate spheroids were recommended for use instead of normal spheroids.

Progress in the theory and practice of electromagnetic flow measurement over the ensuing 15 years was described in Shercliff (1962). Bevir (1970) presented a theory for flow meter assessment based on use of a weighting function, to determine the conditions under which a flow meter output is a function only of the flow rate, independent of the velocity distribution. This article concentrates on pipe flow, not on unbounded fluid flow. The critical conclusion in this paper is that an instrument utilizing point electrodes will never be ideal; that is, the instrument with point electrodes will always be sensitive to the shape of the velocity profile, and not just the mass flux past the sensor.

Bivins (1975), Bivins and Appell (1976), and Mero, Appell and McQuivey (1977) discuss the effects of free stream turbulence on current measurement. They report tests run on electromagnetic current meters of cylindrical config- uration (Model 750 Marsh-McBirney). Grids were used to generate turbulent fluctuations in a submerged jet. Grids had different solidities and dimen- sions, generating turbulent intensities of from 2.5°/° to 12°/°. Mean flows and turbulence characteristics were measured independently of the instrument tested, using a hot film anemometer. Steady flow speeds ranged from 0.25 to 1.0 m/sec, and 0.25 m/sec increments. Because of the small size of the submerged jet facilities, measurements were made much closer to the grid than the 40 mesh-lengths suggested by grid turbulence experiments. The sensors therefore were not located in the near-isotropic field of turbulence normally used in these experiments. Relative errors of as high as 20°/°

were observed for the EM sensor when exposed to turbulent intensities of 11°/₀ with scales of about 2 cm. Mero et al. (1977) report on turbulence tests run on 1.0 cm and 3.8 cm diameter spherical EMCM Marsh-McBirney MMI-551 current meters, with turbulent scales of 2 cm and intensities of 4°/₀. Maximum error reached 18°/₀, with a mean error of closer to five percent for the 3.8 cm spherical sensor. Under similar conditions, the smaller probe had smaller errors, averaging about 2°/₀.

Marsh-McBirney, Inc. (1976) discuss the vertical and horizontal cosine (tilt and azimuth) response of their 10.5 cm diameter spherical electromagnetic flow sensor. They improved the cosine response over earlier models by extending the electrodes past an insulating spherical jacket. Azimuthal response was determined for seven different Reynold's numbers (9,300, 23,000, 46,000, 93,000, 185,000, 231,000, and 259,000). For low Reynolds numbers (Re), results show an inter-cardinal undersensitivity; that is, sensitivity to flows off the electrode axes is less than that near the electrode axes. There is also a slight flattening of the response near the cardinal directions. These two effects become less obvious at higher Reynolds numbers. Vertical cosine response was determined for two unstated Reynolds numbers; these data are difficult to interpret quantitatively because of the plotting option chosen by MMI. Qualitatively the results show a variable sensitivity near the cardinal directions, and intercardinal oversensitivity. Finally, test results are shown for heave response of steady flow, where a vertical oscillation was superimposed on a steady motion. For the test situations presented (at Reynolds numbers of 19,000 and 37,000), heave-induced error was as large as 10 percent, depending on the ratio of the maximum vertical heave velocity to the

10

horizontal flow speed. Tests were run with three different strokes (0.81 and 1.1 m). These latter results were for an instrument 'that most nearly represents the configuration presently built by Marsh-McBirney,' presumably referring to both the sensor and the housing. Because of the data presentation format, no quantification of root-mean-square error can be made for these data.

Cushing has produced a series of papers treating induction flowmeters (1961, 1965, 1974, and 1976), in which he addresses many of the problems arising from various configurations of electromagnetic induction flow sensors. Discussing several different sensor geometries, he evaluates the effects of various electrode lengths and magnet types on the sensitivity of the instrument. In particular, Cushing (1976) discusses the difference in sensitivity of instruments with flush versus protruding electrodes. Concentrating on a spherical sensor with a short magnet and protruding electrodes, Cushing (1976) draws the following conclusions:

1) Sensitivity decreases with increasing boundary layer thickness.

2) Cosine response is a function of Re; as Re increases, cosine response improves.

3) For the sensor under discussion, intercardinal undersensitivity is displayed for horizontal cosine response.

4) Presence of a nearby boundary (sea-bed or water surface) degrades the sensitivity of the instrument. This effect is likely small when the sensor is removed two or more diameters from the boundary. Errors of up to fifteen percent have been determined for some cylindrical sensors removed one diameter from the air/water boundary.

5) Cosine response is good for a spherical sensor, except for the influence of the sensor and electronics housing (which can seriously degrade the vertical response), and the intercardinal undersensitivity

11

in the horizontal cosine response. These two factors degrade the vertical cosine response in an instrument specific manner, reflecting both flow blockage and circulation about the housing.

Considerable testing of these and other current meter systems has been carried out at the Test and Evaluation Laboratory of the NOAA/National Ocean Survey. Appell (1977) and Kalvaitas (1977) discuss some of the test results on EMCM's to evaluate their utility in near-surface current observation experiments. Kalvaitas (1977) and Mero et al. (1977) presented results of combined steady/oscillatory calibrations, indicating that for values of steady/oscillatory velocity ratio near zero, the error in the steady estimate was at most 12 cm/sec, for a circular velocity of 77 cm/sec. For increasing steady/oscillatory ratio, the errors became smaller. Although not graphed in the article, it was stated that non-coplanar steady/oscillatory errors were similar to those using coplanar steady/oscillatory motion. Appell (1977) reports on tests performed at the David Taylor Naval Ship Research and Development Center (DT-NSRDC) in a tank 274 m long, with variable combined steady/oscillatory flow conditions. His study is based on results from more than one Marsh-McBirney model 555 spherical 10.5 cm (4-inch) diameter EM sensor. Steady calibrations for a single cardinal axis are generally good, with a characteristic calibration curve for the meters examined. Steady gain decreases over the range from 0 to 20 cm/sec (Re of 0 to 20,000), where the trend reverses to gain increase until it reaches a constant level at about 120 cm/sec (Re=1.2x10^5). The best-fit linear regression yields a worst case residual error of $\pm$ 1 cm/sec through a range of 0 to 250 cm/sec. However, for all four cardinal calibrations (two axes with two directions) combined to obtain an average sensor performance, the residual standard error (RSE--defined as the root-mean-square of all residual calibration errors over the test range)

is approximately 3 cm/sec over the range of 0 to 250 cm/sec. This difference is due to gain imbalances in the two axes, and differences in the positive and negative outputs of the sensors (due perhaps to electrode alignment errors). If the regression is performed using an offset of zero (instead of determining the offset from the data), in accord with the calibration provided by the manufacturer, considerable increase in errors results. Linearity errors of 2 percent to 10 percent result from this procedure. Zero levels for instruments fluctuated in the laboratory, with a zero offset of approximately $\pm$ 2-4 cm/sec, versus the offset of zero stated by the manufacturer.

For the sensors evaluated by Appell (1977), error is encountered in the vertical cosine response when the tilt angle exceeds 10°. Predicted vertical cosine response errors peak at 30 percent at a 70° relative angle, due primarily to instrument mounting hardware and electronics housing.

Heave motion, as discussed by both Kalvaitas (1977) and Appell (1977), introduces errors of less than 5 percent in the steady component under most circumstances. However, when larger oscillatory velocities (up to 78 cm/sec) were superimposed on low (about 10 cm/sec) steady flows, positive residual errors of from 35 percent to 85 percent resulted, depending on the orbital velocity angle relative to the steady velocity. The conclusion of Appell (1977) was that improvements were underway on noise and zero-offset character-istics of the spherical sensor, but that further tests were needed on the long-term stability and reliability of the EMCM's.

McCullough (1978) evaluated the performance of a number of current sensors for near-surface (wave-influenced) measurements of low frequency flow fields. Included amongst these sensors were spherical EMCM's, which were evaluated for their cosine response and steady response under combined steady/oscillatory flow fields. In particular, McCullough was concerned with the vertical cosine

response imposed by surface gravity waves superimposed on a mean flow field. Because of imperfect cosine response, the mean flow is either underestimated or overestimated under these combined flows. The vertical cosine response for a cylindrical EMCM exhibits intercardinal undersensitivity, so the mean flow is underestimated. With large ratios of oscillatory to steady velocities, the EMCM's show a relatively large error (up to 40 percent in gain) when the wave velocity is twice that of the steady. Even though McCullough's (1978) study emphasizes vertical cosine response, horizontal cosine response similarly will affect mean flow estimates if not corrected during data reduction.

Lavelle, Young, Swift and Clarke (1978) briefly describe some steady calibration results using a Marsh-McBirney Inc. model 511 flow meter. Utilizing a recirculating flow tunnel, they state that no differences in calibrations were observed for either axis or between the two directions of flow for each axis, so no distinction was made in the analysis between axes or orientation. They found a break in the calibration curve at 80 cm/sec (Reynolds number of 77,000), attributing this break in slope to separation in the boundary layer surrounding the sphere. Because of this break, they best fit their calibration results to three straight line segments, providing no rationale for selecting three instead of two segments. Presumably three segments will yield a better fit than two segments, although the statistics of the fit are not provided to evaluate whether this improvement was statistically significant or not. It can be misleading to fit calibration curves to either a large number of line segments or to too high an order polynomial without examining the statistics of the fit closely, and carefully assessing calibration errors. With this three-line fit, maximum error was less than 2.5 cm/sec, with an rms error not provided. Flow speeds of up to 155 cm/sec were used, at approximately 10 cm/sec increments. On the actual deployment frame, errors were encountered due to interference from the nearby presence of their turbidimeter.

Griffiths (1979) studied the effect of turbulence on EMCM sensor response, using four different types of EMCM including a 13.4 cm diameter sensor with electrodes protruding 1 cm above the surface. To avoid blockage effects (since no independent in situ measurement of flow speed was made), turbulence was produced by towing a circular cylinder upstream of the sensor. For the low turbulent intensities studied, Griffiths (1979) found no systematic errors in measurement. Griffiths (1979) also determined the averaging length of the sensor is of the order of the electrode separate, confirming previous work.

Cunningham, Guza and Lowe (1979) examined some dynamic characteristics of Marsh McBirney, Inc., EMCM's as part of the preliminary work for the Nearshore Sediment Transport Study. Using a mechanical device for this calibration, they examined the flowmeter gain under oscillatory conditions only, with broad-band spectral motion produced by their mechanical arm. The probes examined were Marsh-McBirney model 512/OEM, with 4.0 cm diameter spherical probes, mounted remotely from their electronic housing. Results from their study indicated that flowmeter gain depended on the frequency content and amplitude spectrum of the forcing function, with a variation in gain of about 20 percent over the runs reported in their study. However, they estimate that if one uses a DC gain (steady flow), a maximum error of 7 percent would result over a frequency range of 0-0.25 hz, and rms velocities of 0-0.6 m/sec. Spurious (induced) mean flows in the presence of symmetric and asymmetric oscillatory forcing were examined, with a maximum observed 'mean flow' error of 5 cm/sec, using a highly asymmetric oscillatory ramp function. For a sinusoidal flow field, errors were typically less than 4 cm/sec. Cunningham et al. (1979) also reported an accuracy of 2 cm/sec in the offset of the current meters due to the noisy calibaration environment they used. This study did not present data

15

in terms of non-dimensional dynamical groupings to systematically search for Reynolds number or Strouhal-related errors. Their study does indicate, however, the possibility of spurious mean flows induced by large oscillatory flow components, although not presenting the sense of these measured flows (the induced flows can be either in-line or orthogonal to the oscillatory component).

Dibble and Sollitt (1981) present a combined theoretical and experimental determination of the amplitude and frequency response of current meters, including phase shift information. The motivation was to obtain correct phase information for waves and heave motion of current meters mounted on moorings. They model the current sensors as variable order linear differential equations with constant coefficients in an effort to determine time constants, slew rate limit, static sensitivity, natural frequency, damping ratio, and other factors affecting sensing of ocean currents. Although not tested on a spherical probe Marsh-McBirney current sensor, the analytical and laboratory methods may be of interest for further extensive calibrations of these sensors. Though not providing information on the steady/oscillatory calibration of current sensors, the technique provides a way to estimate maximum decelerations and accelerations which permit accurate estimation of flow speed.

Finally, Aubrey (1983) presents some preliminary results of EMCM calibrations performed at the Woods Hole Oceanographic Institution and the Massachusetts Institute of Technology which showed a definite nonlinearity in the calibration of the current meters under steady flow conditions, with a break in gain at an Re of approximately 61,000, lower than the 77,000 found by Lavelle et al. (1978). In addition, results for oscillatory calibrations were presented, showing considerable nonlinearity in gain with oscillatory Reynolds

Number (Re_0). For the steady case, where a break in gain was observed, the best-fit two segment line has gains differing by 18 percent, considerably larger than the manufacturer's error specifications. A basis for dimensional analysis of the steady and oscillatory flow results was also outlined in this paper.

FLOW AROUND A SPHERE

This section summarizes past work on flow around spheres. Although some of the discussion may appear esoteric, we present a detailed overview of flow complexities about spheres to indicate why EMCM response might be expected to be non-linear. A number of factors affect boundary layer and wake formation around blunt bodies; the present synthesis illustrates the intricacies of these factors. The casual reader may wish to skip this review section.

Because the electrodes of the electromagnetic current meters examined extend into the flow field from the surface of a sphere (figure 1), the flow sensor is sensitive in some poorly defined manner to the effects of the sphere on the flow field. Unfortunately, flow pattern around a sphere is complicated, varying with the structure of the incident flow field. For instance, at low Reynolds numbers the flow around a sphere is laminar, and attached to the sphere around the entire perimeter. As Re increases (Re >10 or so), the flow is still laminar, but it separates from the sphere at an angle of $80°$, from the axis of flow. In the range 70< Re < 5000, a regular von Karman vortex street is present, with periodic vortices shedding from the sphere. Over the range 5000 < Re < 3×10^5, the wake is fully turbulent. When the Reynolds number exceeds 3×10^5, the boundary layer itself becomes partly turbulent, moving the point of separation to the rear, at an angle of about $120°$. This causes the familiar rapid decrease in drag coefficient observed in laboratory environments. When Re >3×10^5, the character of the boundary layer changes even more.

17
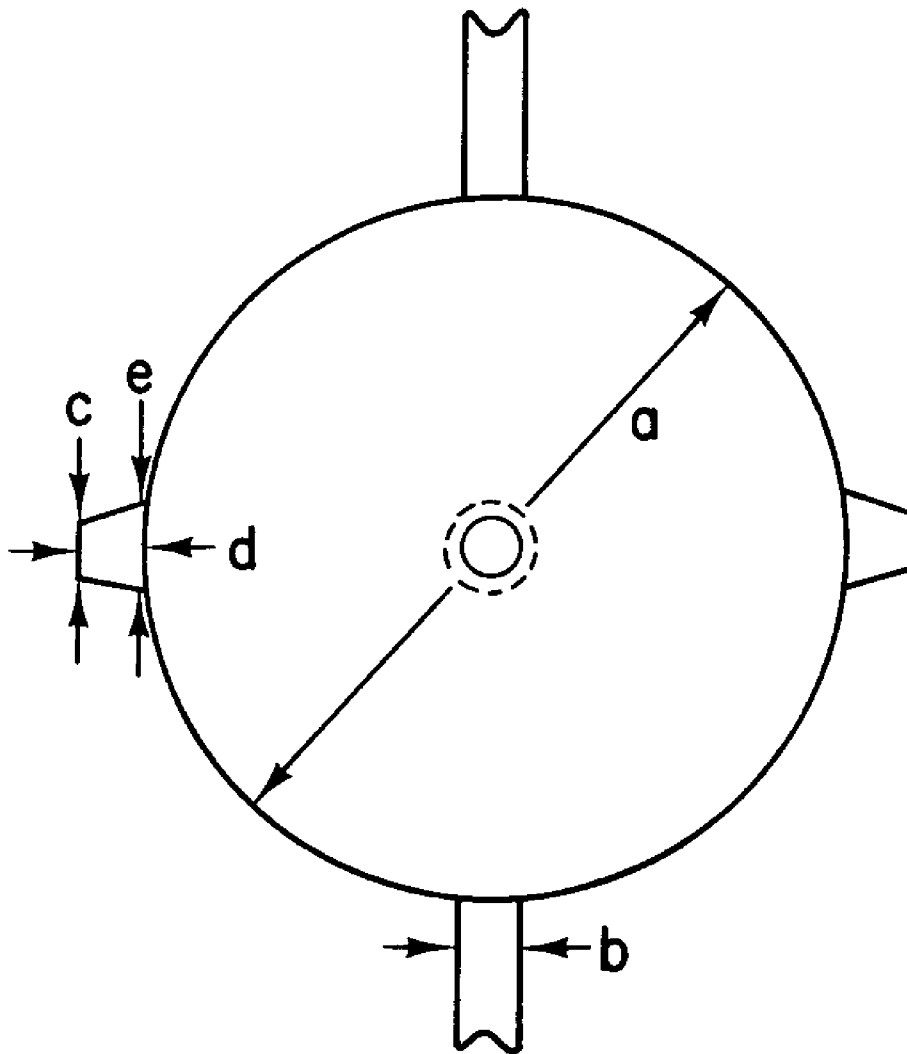
	551 M 512/0EM	551
a	4.05 cm	10.53 cm
b	0.96 cm	2.54 cm
c	0.50 cm	1.15 cm
d	0.43 cm	1.13 cm
e	0.68 cm	1.75 cm

Figure 1. Schematic of the large diameter and small diameter Marsh-McBirney electromagnetic current sensors, showing primary dimensions and location of roughness elements.

As described in the above example, flow around a smooth sphere is compli-
cated, even in uniform steady flow. Additional factors increase the flow
complexity even further, including: oscillatory flows, distributed or three-
dimensional surface roughness on the sphere, presence of high ambient levels
of turbulence at scales of the order of the sensor diameter, and presence of
mounting brackets, pressure case, or other hardware. In this section we
briefly review some of the literature on flow around spheres, paying special
attention to boundary layer separation and wake formation. Because of the
complexities of flow past a sphere with variable roughness and incident
turbulence levels, much of the applicable work is empirical. Numerical
solutions to flow around a sphere have been developed only for limited and
simplified flow conditions.

The Reynolds number dependence of the drag coefficient past a smooth sphere
provides a useful perspective of boundary layer behavior in the region of the
sphere. Behavior of the drag coefficient can be classified into four distinct
regions (see figure 2, from Roshko, 1961 and Achenbach, 1974) in the high
Reynold's number regime:

a)   Subcritical regime: the flow around the sphere is laminar, and flow
separation is laminar. The separation point is near $80°$, measured along the
axis of flow from the stagnation point. In the Reynold's number regime of
interest, the separated wake structure is highly turbulent, with less organiza-
tion than in the lower Reynolds number regime associated with regular von
Karman vortex streets. In the subcritical range, as Re increases, the wake
decreases in thickness from a value of $b>d$ (b = wake thickness, d = sphere
diameter) to $b<d$.

19
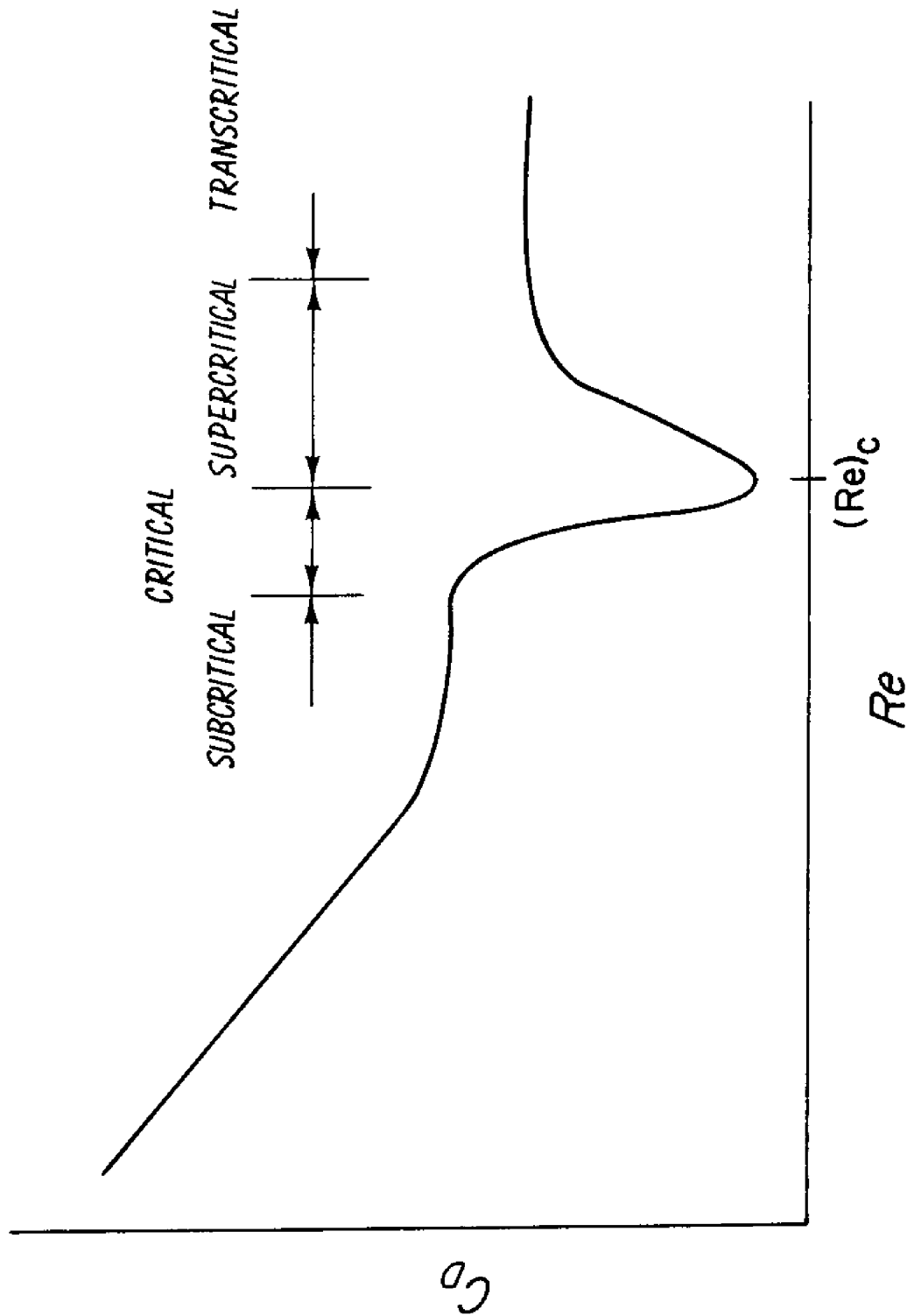
Figure 2. Schematic of the behavior of the drag coefficient C_D for flow
past a sphere, illustrating the four primary Reynolds number
ranges descriptive of different flow regimes (after Roshko, 1961).

b) Critical range: This is the beginning of transition from laminar to turbulent boundary layer structure. Here laminar separation begins, but results in turbulent reattachment rather than complete separation, followed by a delayed final turbulent separation. The separation point moves towards the rear of the sphere.

c) Supercritical range: An initial laminar boundary layer becomes turbulent along the perimeter of the sphere. As Re increases, the transition point moves closer to the stagnation point. Separation has moved aft of the laminar separation point, from $80°$ to $120°$. Flow behavior is still Re-dependent in this range: as Re increases, the wake width increases, although wake width is never as large as the sphere diameter.

d) Transcritical range: This regime is characterized by a transition to turbulent boundary layer structure sufficiently close to the stagnation point that the flow is largely independent of Re. Separation in this regime is purely turbulent.

As was discussed by Nakamura and Tomonari (1982), the definition of each of the above ranges is not necessarily properly defined by the drag coefficient curve. In particular, presence of roughness elements can alter the bounds of the physical regimes from the more descriptive bounds shown on the drag curve. Based on the objections, Nakamura and Tomonari (1982) rely heavily on the shape of the drag curve to define these boundaries, rather than on the physical descriptions described above. We use the drag curve as an indicator of boundary layer and wake structure.

Steady flow over a smooth sphere:

For Re less than Re_c (critical Reynolds number at which transition occurs), laminar flows are developed on the sphere up to the point of separation. Since separation for $Re<Re_c$ is near $80°$, then two or three

21

electrodes in a spherical EMCM will always be in the wake of the separated region. Flow in these wakes is complex, and poorly defined in spite of numerous models describing these features (see for example, Landau and Lifshitz, 1959, and Schlichting, 1968). The width of a laminar wake varies as the square root of x, the distance from the point of separation. For a turbulent wake around a sphere, the width of the wake increases as $x^{1/3}$. As discussed before, the wake in the subcritical region can be either laminar or fully turbulent; for most flow situations encountered using EMCM's, the wake will be turbulent. These simple relationships, however, only hold for large values of x. Closer to the sphere and to the electrodes, the flow is likely very different.

For subcritical flows, the boundary layer up to the point of separation will be laminar. Growth of the laminar boundary layer is a function of the Reynold's number, varying approximately as (Schlichting, 1968):

$$\delta/\ell = 5 \ Re^{-1/2}$$

where δ is the boundary-layer thickness (point at which the boundary layer velocity is 99°/₀ of the free-stream velocity), and ℓ is the distance from the stagnation point. Although derived for a flat plate, this equation can be used to estimate boundary layer thickness on spheres. For a 4.0 cm diameter sphere, the boundary layer thickness at separation is approximately 0.15 cm for a flow of 25 cm/sec. For a 10.5 cm diameter sphere, the boundary layer thickness at separation is approximately 0.4 cm thick for a flow of 10 cm/sec.

A turbulent boundary layer is thicker, but depends on the magnitude and structure of boundary roughness. For a smooth sphere, the turbulent boundary-layer thickness can be shown to be (Schlichting, 1968):

$$\delta/\ell = 0.37 \ Re^{-1/5}$$

For Re = 3×10^5 (transition), δ = 0.03 cm. These boundary layer thicknesses are less than the height of protruding electrodes from the Marsh-McBirney EMCM's (figure 1).

For Reynolds' numbers in the range of about 50 to 3000, flow past a sphere has an associated natural shedding frequency, the Strouhal frequency f_s. Table 1 lists the Strouhal frequencies for two characteristic sphere diameters at the limits of the natural Re bounds for Strouhal shedding. Natural frequencies range from two seconds to hundreds of seconds for these spheres. For steady flows, the primary influence of Strouhal shedding is to lower the value of Re_c for transition to turbulent flow if it introduces movement in the instrument. For rigidly mounted spheres, such deflections should be negligible, and shedding should have little influence on Re_c. For non-rigid mounts, such shedding may present changes in wake structure which could affect instrument response to incident flows.

Effects of boundary roughness on flow around spheres:

Structure of the flow field around a sphere can be substantially modified by the presence of roughness elements on the surface of the sphere. Roughness has three primary effects on the flow field:

a) Changes Re_c for boundary layer transition from laminar to turbulent flow, hence the character of the wake for any particular Re.

b) Changes the boundary layer thickness in the region of the roughness elements.

c) For turbulent flows, roughness can determine whether flows are smooth turbulent or rough turbulent. In the transcritical regime, the relative roughness determines the overall flow characteristics.

TABLE 1: Strouhal Periods*

Sphere Diameter

	4.0 cm	10.5 cm
Re = 50	117 sec.	833 sec.
Re = 3000	1.9 sec.	14.1 sec.

*Assuming St = 0.25 (Seymour, 1974)

Table 1. Strouhal periods for spheres.

Much work has been performed on determining the effect of roughness elements on characteristics of fluid flow. Wooding et al. (1973) present a useful summary of the effects of regular arrays of roughness elements of varying geometries. Drag partitioning (between skin friction and form drag) is discussed, as is the effect of the dimensions and concentration of roughness elements on the drag in a turbulent boundary layer. Our concern here is primarily for sparsely distributed roughness elements, so we will discuss primarily that concentration limit. Wooding et al. (1973) discuss flow over flat plates, while we are concerned with flow past spheres with considerable curvature.

The effect of roughness elements on transition from laminar to turbulent flow (Re_c) has been well documented experimentally, although we still lack a coherent theory to describe this phenomenon in detail (Tani, 1969). For the transition problem as applied to sparsely distributed roughness, the critical factor is the relative height of the roughness element to a dimension characteristic of the flow. The relative roughness can be defined as k/d, where k is the roughness height and d is the sphere diameter. Because the height of the element relative to the boundary layer thickness is critical for tripping the boundary layer, a better definition of relative roughness for the transition problem is k/ℓ, where δ_ℓ is the laminar boundary layer height, which varies as a function of distance from the stagnation point. For $k/\delta_\ell \geq O(1)$, transition is likely to occur at the roughness element, rather than at its normal downstream location. It will also occur at a lower Reynolds' number than for the purely smooth situation. The presence of roughness favors transition such that a rough wall will undergo transition at an Re_c less than that for a smooth wall. For single, cylindrical roughness elements, the critical height of roughness elements (that height not affecting transition), is (Schlichting, 1968):

$$\frac{u_{*k}\, k_{crit}}{\nu} = 7$$

where $u_{*k} = \sqrt{\tau_{ok}/\rho}$ is the friction velocity, and τ_{ok} is the shear stress at the wall at the position of the roughness element (Schlichting 1968). Tani et al. (1940) provide a minimum height at which transition will occur at the element itself:

$$\frac{u_{*k} \, k_{crit}}{\nu} = 20.$$

Alternatively, the criterion for transition can be expressed as:

$$U_1 \, k/\nu = 600 \quad (Tani, 1969)$$

where U_1 is the free stream velocity. This value is derived for three-dimensional roughness elements, with a height-to-width ratio of 1. This critical roughness Reynolds number varies approximately proportionally to the two-fifths power of the height-to-width ratio of the roughness element. For a Reynolds number of 40,000, these parameters have been calculated for a 4.0 and 10.5 cm. sphere (table 2). Calculations show that surface roughness of less than a mm are required to cause transition at the position of the roughness element itself. The Marsh-McBirney electromagnetic current meters have electrodes protruding one cm or more above the insulating, hydrodynamically smooth sphere, which will cause transition at the roughness element. The transition will result is a wedge-shaped wake extending downstream (Tani, 1969), merging in some fashion with the wake generated from the mounting hardware along the axis normal to the plane of the electrodes.

Once the flow separates at the roughness element and becomes fully turbulent, flow behavior is more difficult to predict. For a certain roughness concentration (density) along the perimeter of the sphere, the entire boundary layer will become either fully turbulent or separated, depending on the orientation of the roughness elements with the flow field, and the Reynolds

TABLE 2

Critical Height and Minimum Height for Transition

(Re = 40,000)

	d = 4.0 cm	d = 10.5 cm
Critical Height	0.013 cm	0.034 cm
Minimum Height	0.060 cm	0.16 cm

Table 2. Critical roughness height and minimum roughness height for transition to turbulent flow.

number. This type of behavior is poorly understood theoretically and empirically, deserving further study in the future. Since the two-dimensional turbulent wake behind a separated flow expands as the one-third power of downstream distance (Schlichting, 1968), the roughness concentration along the perimeter transverse to the flow direction would have to be order of 0.5 to have a uniform turbulent boundary layer or wake immediately downstream of the roughness elements. Since this is not the case for EMCM's, the resulting flow field will include a strong tangential flow nonuniformity downstream of roughness elements. The turbulent separated flow may remain separated (bringing the separation point to the roughness element), or may reattach to the sphere downstream, depending in a poorly understood manner on the flow Reynolds number and roughness Reynolds number. The result of these roughness elements is to cause earlier transition to turbulent boundary layer flow, and probably earlier turbulent separation about the sphere.

If the boundary layer flow is fully turbulent, its character will depend on the relative size of the roughness elements. For spheres, the non-dimensional roughness is often given as k/d, where k is the physical roughness height. However, a more physical description of relative roughness is k/δ_ℓ, where δ_ℓ is the viscous sublayer thickness. As discussed by Wooding et al. (1973) and many others, boundary layer behavior (including boundary layer thickening and drag partitioning) is a function not only of the roughness height but also its aspect ratio, frontal cross-sectional area, and concentration. For the low concentrations of roughness on EMCM spheres, we can simplify the problem to include only the roughness height, and determine flow characteristics close to these elements.

Turbulent boundary layers can be characterized as hydraulically smooth, transitional, or rough, depending on the ratio of the roughness scale to the viscous sublayer thickness, δ_ℓ. Since the thickness of the viscous sublayer is given as:

$$\delta_\ell = \text{constant} \cdot \nu/u_*,$$

the relative roughness becomes:

$$\frac{k}{\delta_\ell} = \frac{u_* k}{\nu}$$

where u_* is the friction velocity. Because this convention is generally used for distributed roughness, rather than point roughness, the physical roughness k is generally replaced by the Nikuradse equivalent sand roughness, k_s. Relations between k_s and k are discussed in Wooding et al. (1973), including effects of roughness concentration and aspect ratio.

The three roughness regimes are:

a) Hydraulically smooth regime: here the roughness is small compared to the sublayer thickness, so the resistance is dependent on the external flow Reynolds number. The range for this regime is:

$$0 \le \frac{k_s u_*}{\nu} \le 5 \qquad\qquad C_D = f(Re)$$

b) Transition regime: Here the protrusions are the same order as the sublayer thickness, so the drag coefficient (C_D) is a function of both the external flow and the relative roughness. The regime is defined by:

$$5 \le \frac{k_s u_*}{\nu} \le 70 \qquad\qquad C_D = f(\frac{k_s}{d}, Re)$$

where ($\frac{k_s}{d}$) is the roughness relative to a characteristic length scale of the body.

c) Fully rough regime: Roughness elements extend beyond the viscous sublayer thickness, disrupting the sublayer structure. Form drag becomes more important than skin friction, so the drag is a function of the roughness characteristics, not the external flow. This regime is defined by:

$$\frac{k_s u_*}{\nu} > 70 \qquad C_D = f(\frac{k_s}{d})$$

As an example of this behavior, drag coefficients for spheres with varying types of roughness at high Reynolds numbers have been determined (figure 2). For smooth spheres, Bailey (1974) has compiled measurements of drag behavior, discussing differences between observations and measurement techniques. Achenbach (1974) presented measurements of surface roughness on flow past spheres. As relative roughness increases, the critical Re for transition to turbulent boundary layer occurs at successively lower Re, and the behavior of the drag coefficient in the transcritical regime is a function only of relative roughness, not of Re (figure 3 and 4). As k/d increases, the drag coefficient increases in the transcritical regime, and it remains nearly constant with no further dependence on Re (figure 5). C_D for a hydraulically smooth sphere, however, varies as a function of Re throughout the transition regime, at least up to Re $= 3 \times 10^6$. Angle of boundary layer separation (ϕ) varies as a function of both Re and the relative roughness (figure 6). As relative roughness increases, separation occurs further aft due to earlier separation, then further forward as one approaches the transcritical regime. Strouhal number also fluctuates slightly according to the relative roughness (Achenbach, 1974), but remaining within the range of 0.18 to 0.20 for 2×10^5 >Re>2×10^4.
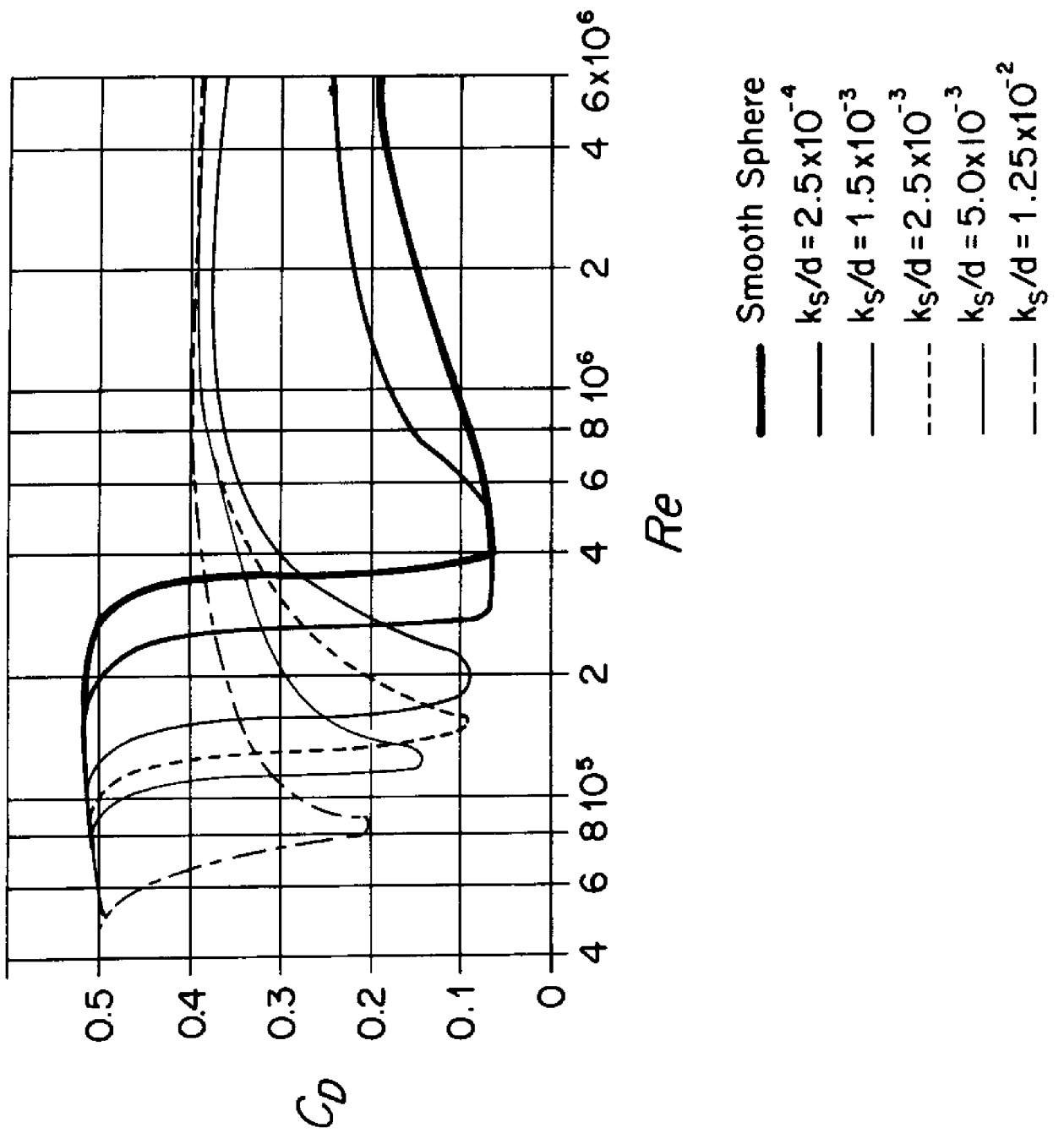
Figure 3. Drag coefficient versus Reynolds number for a sphere with varying surface roughnesses (after Achenbach, 1974).
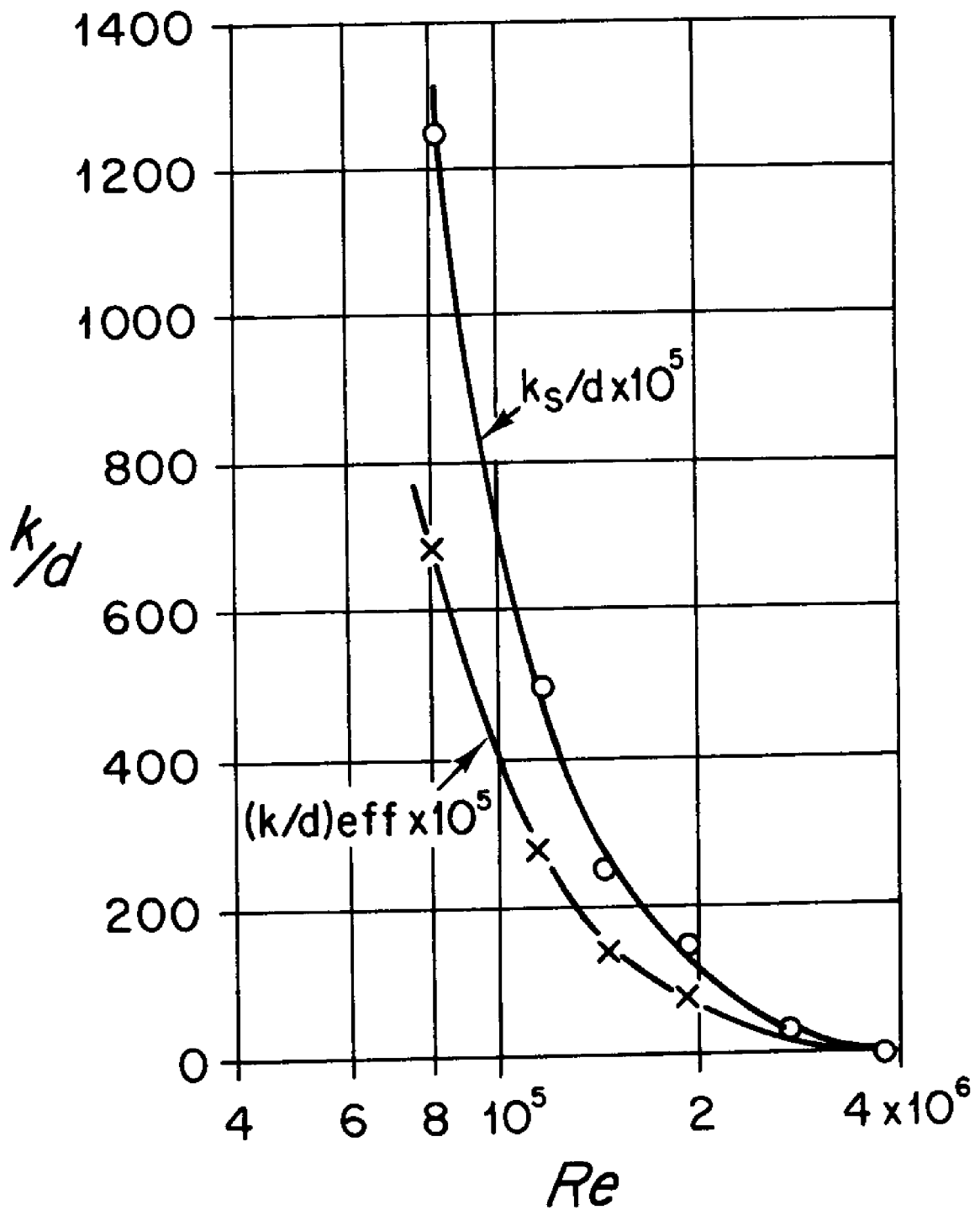
Figure 4. Roughness parameter k/d versus critical Reynolds number for flow around spheres (after Achenbach, 1974).
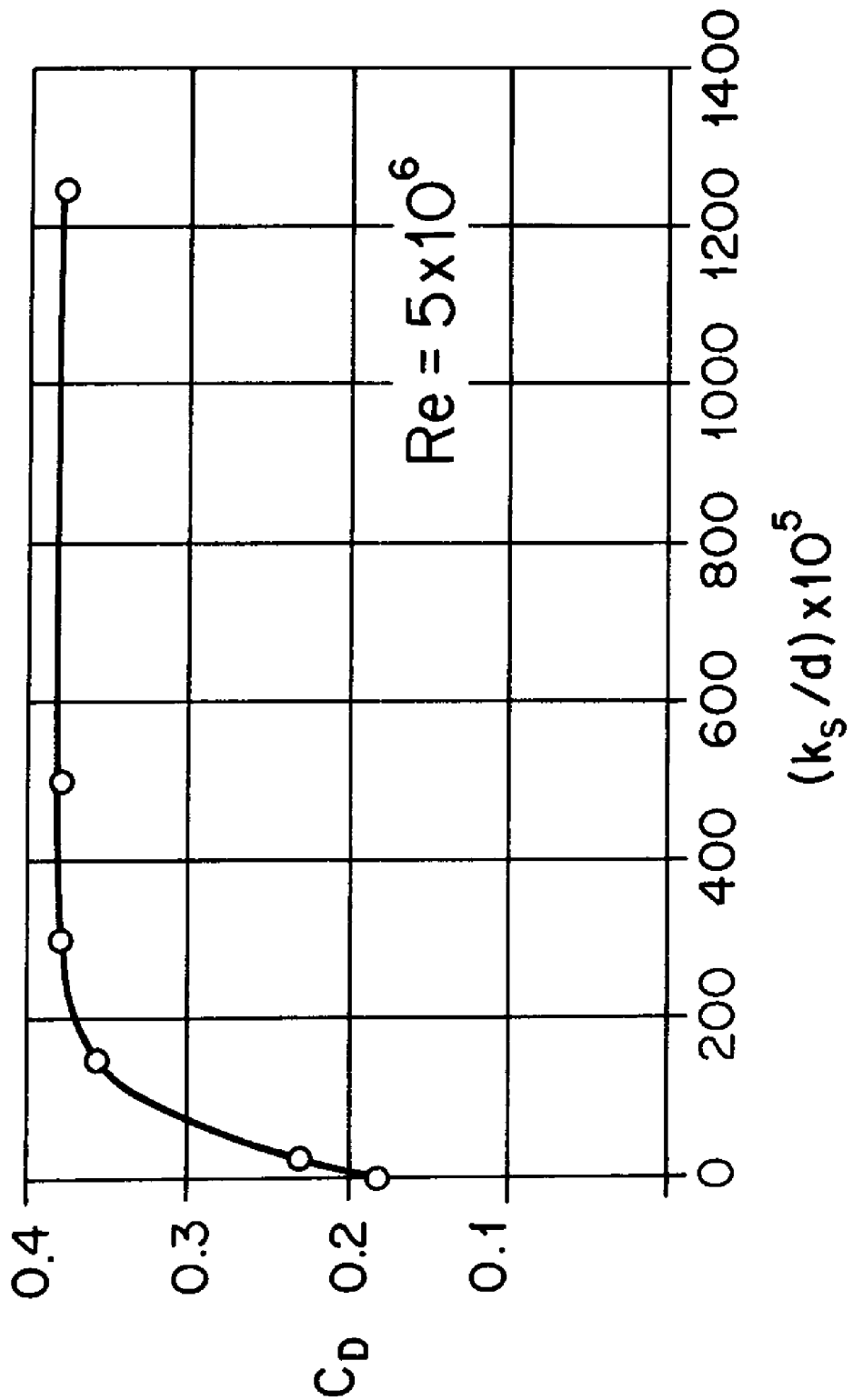
Figure 5. Asymptotic transcritical drag coefficient versus roughness parameter for a sphere at a Reynolds number of 5×10^6 (after Achenbach, 1974).
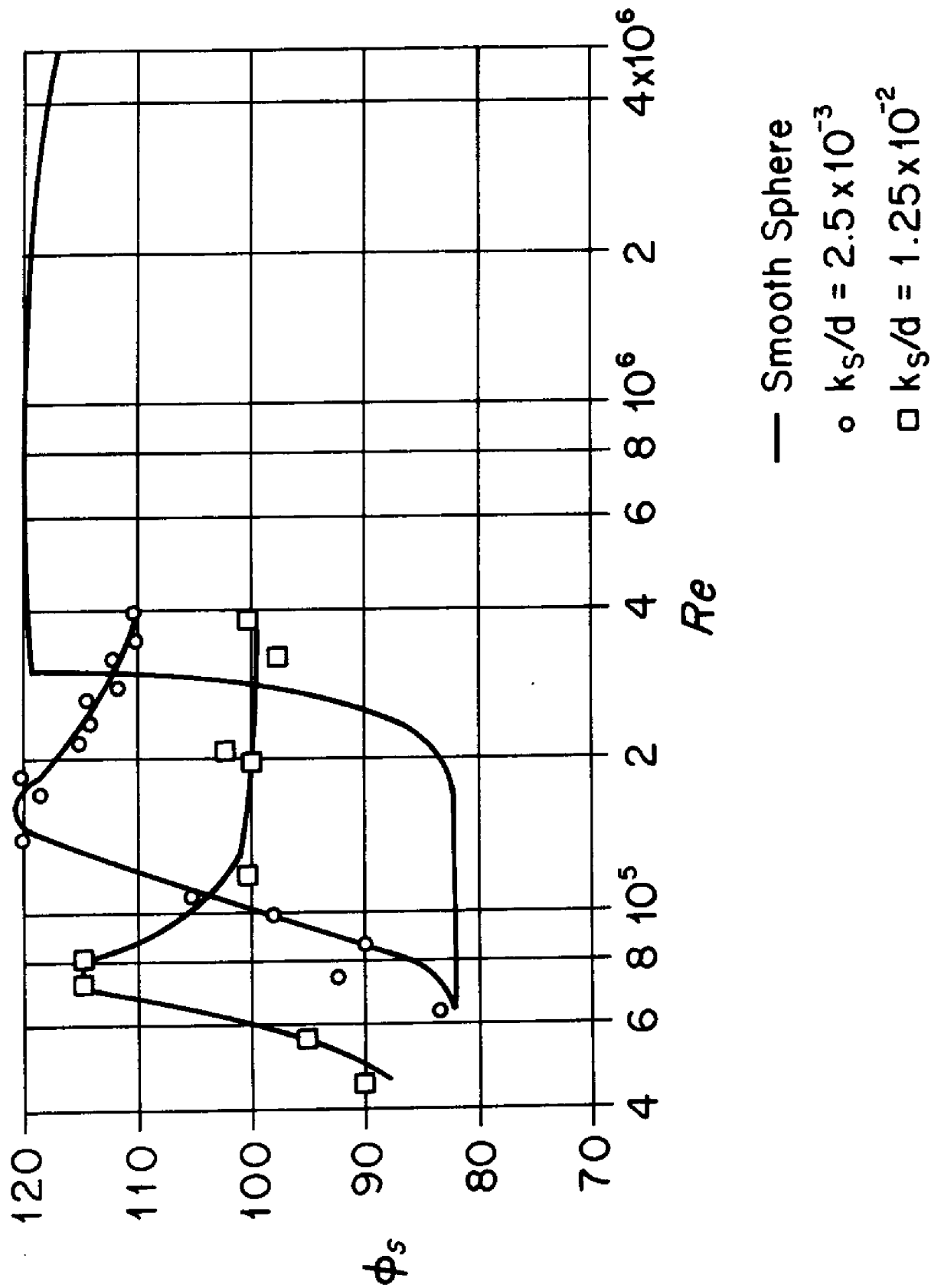
Figure 6. Angle of boundary layer separation, φ, versus Reynolds number for a sphere, as a function of roughness parameter (after Achenbach, 1974).

34

Admissable roughness, defined as the maximum height of individual roughness elements which causes no increase in drag compared to the hydraulically smooth flow, is a useful concept for determining the allowable tolerance in constructing a "smooth" insulating sphere. Empirically, the admissable roughness, k_{adm}, has been determined as:

$$\frac{U \; k_{adm}}{\nu} \approx 100$$

For spheres of diameter 4.0 and 10.5, values of k_{adm} have been calculated for Re of 40,000, at a point transverse to the incident flows ($90°$ from stagnation point table 3). Schlichting (1968) states that the admissable height of roughness elements is independent of the length of the plate, and is determined solely by the free-stream velocity and kinematic viscosity. For Marsh-McBirney EMCM's, the surface of the sphere is at least this smooth in factory-fresh condition. Once biological fouling occurs, however, this condition is exceeded and any turbulent flow would become rough turbulent quickly. The turbulent boundary layer is more sensitive to boundary roughness for transition to rough turbulence than a laminar boundary layer for transition to smooth turbulent.

In summary, a spherical EMCM sensor with protruding electrodes will cause the transition to turbulence at a lower Re than a smooth sphere. It will also increase the drag, partly through form drag and partly by moving the separation point further forward than in the smooth case. The resulting turbulent wake will alter the flow field around the downstream electrodes, perhaps altering their sensitivity. This behavior is dependent on the relative angle between the flow and the cardinal current sensor directions (defined by electrode axes), so the EMCM will have some non-cosine response to off-axis flow.

TABLE 3

Admissable Roughness Values

	d = 4.0 cm	d = 10.5 cm
Re = 40,000	0.0075 cm	0.020 cm
Re = 80,000	0.0037 cm	0.010 cm

Table 3. Admissable roughness scale for hydraulic 'smoothness'.

The two prototype Marsh-McBirney sensors evaluated in this study have protruding electrodes with large surface roughness (figure 1). Relative roughness (k/d) for the 4.0 cm probe is approximately 0.10, and for the 10.5 cm diameter probe is about 0.09. These relative roughness values are large and should cause early transition to turbulence, as well as increased form drag and wake turbulence at higher Re.

Unsteady Effects

All discussion to this point has described steady flow around a sphere with variable surface roughness. Addition of unsteady, oscillatory behavior in the flow field considerably complicates the boundary layer and near-surface flow field. We consider pure oscillatory motion first, then evaluate its impact on a superimposed steady incident flow.

A laminar oscillatory boundary layer on a flat plate has a thickness, δ_0, given as:

$$\delta_0 \sim \sqrt{\nu T} \quad \text{where } T = \text{period of oscillation}$$

Because of the external time-scale imposed on the oscillatory boundary layer, it is generally much thinner than the steady boundary layer. As an example, the laminar oscillatory boundary layer under a ten second wave reaches a maximum thickness of about 0.3 cm. Around a blunt body like a sphere, the unsteadiness in the flow causes a complicated wake structure. As the flow accelerates in the positive direction, separation will occur at the downstream stagnation point. As time progresses, separation will occur closer to the separation point for steady flows ($\sim 110^\circ$). The time required for separation scales with the maximum oscillatory flow speed, U_m, but with an unknown coefficient. For a sphere started impulsively from rest, the time for separation to begin is (Schlichting, 1968):

$$\tau_s = 0.392 \frac{d}{U_\infty}$$

Investigation of this transient separation deduced for impulsive motions of spheres as applied to oscillatory flow development evidently has not been completed.

A sphere oscillated in a fluid at rest or a fixed sphere exposed to surface wave motion will exhibit a steady streaming which may affect steady flow estimates. At small values of A/d (where A = peak-to-peak amplitude of oscillation, d = sphere diameter), Jenkins (1980) exhaustively described the complex flow around the sphere. For the case of a sphere oscillating in a fluid at rest, with the condition of A/d <<1, Schlichting (1968) derived a simple form for the streaming velocity:

$$U_s(x) = -\frac{3}{4n} U_0 \frac{d\,U_0}{dx}$$

where U_0 is the amplitude of motion of the sphere, x is coordinate in the line of motion, and n is the frequency of motion. This steady flow is seen only at second order, and is due to the interaction of inertia and viscosity. The result is not particularly applicable to shallow water use of EMCM's, where A/d >1, but may be applicable for mid-water moorings in deeper water, particularly for large d.

The parameter A/d (sometimes called the Keulegan-Carpenter number) is an important one for oscillatory flows, as it is the ratio of nonlinear inertial terms to linear inertial terms (convective to unsteady terms):

$$\frac{u\partial/_{\partial x}}{\partial/_{\partial t}} \sim \frac{A}{d}$$

Other terms of importance are the unsteady Reynolds number R_0:

$$R_0 = \frac{Ud}{\nu}$$

38

and the Strouhal parameter, S_s:

$$S_s = \frac{df}{U}$$

If U is replaced by U_m, we have an unsteady Strouhal parameter (S_o):

$$S_o = \frac{df}{U_m} \simeq d/A$$

which is the inverse of the Keulegan-Carpenter parameter.

Seymour (1974) discusses the resistance of spheres in oscillatory flows, determining the drag coefficient and added mass coefficient for unsteady flows at different ranges of A/d, including those ranges of use in field experiments. He showed the resistance due to oscillatory motion to be higher than that for steady flow.

Mercier (1973) considered the problem of combined steady/oscillatory flows past a circular cylinder, over a range of A/d. Similar work for flow past a sphere evidently has not been carried out. Because of the similarity between flows past circular cylinders and spheres, we will discuss some of Mercier's results. Experiments were run on oscillations transverse to the steady motion, on oscillations inline with the steady motion, as well as on pure oscillatory motion. Results of these experiments are discussed below:

a) Pure oscillatory: Transverse forces on the cylinder were observed for A/d ratios of 1 to 4. These forces, due to vortex generation and separation, can cause oscillations in the cylinder with concommittent increase in drag.

b) Oscillation transverse to steady flow: Increased drag coefficients are observed for even small oscillatory motions. The eddy shedding associated with transverse oscillatory motion gives rise to a transverse force at twice the frequency of oscillation. Separation due to oscillatory motion disrupts

the normal boundary layer separation expected for steady motions alone. When the frequency parameter S_0 is close to the Strouhal number, St, the possibility exists for self-excited oscillations of the sphere, for A/d <1. This is not observed for A/d >1.

c) Oscillations in-line with the steady motion show very high lift forces, at frequencies of $\frac{1}{2}\omega$, $\frac{3}{2}\omega$ and $\frac{5}{2}\omega$. There is a critical frequency parameter S_0 where the coefficient of drag (C_D) and of added mass (C_m) undergo sharp changes. There is no indication of self-excited oscillation (where S_0 = St) for the inline steady/oscillatory situation.

Mercier's results demonstrate the importance of oscillations on the flow structure associated with a steady flow, if only by demonstrating intense changes of drag coefficients with oscillatory motion. The physical picture of vortex shedding or separation due to oscillatory flow combined with that due to steady motion demonstrates the complexity of boundary layer flows in combined steady/oscillatory motions. The wake region in these flows is complex, as both steady and oscillatory wakes interact; separation in each of these flow structures is a function of the structure of the wake due to the companion flow, as well as to the distribution of surface roughness elements. Since the roughness elements on an EM sensor are not symmetrical for all flow directions, angular response should be significantly different from cosine for particular combinations of Reynolds number and Kuelegan-Carpenter number.

Effects of free-stream turbulent scales and intensity:

Experiments have verified the importance to boundary layer behavior of free-stream levels and scales of turbulent flow. Most experiments on flow separation, drag partitioning, and transition to turbulent flow on spheres have been performed under ambient flow conditions whose turbulent intensities

are very low. For example, turbulence intensities in the free stream are often of the order of 0.12°/o (Nakamura and Tomonari, 1981) to 0.7°/o (Achenbach, 1968), where turbulence intensity, I, is defined as:

$$I = \frac{\overline{(u')^2}^{1/2}}{U_\infty}$$

u' is the fluctuating component of the free-stream velocity and U_∞ the steady component. As discussed by Fernholz (1978), the free-stream turbulence level drastically influences boundary layer flows. An increase in turbulence level, I, from 0.2°/o to 5°/o results in an increase in growth of boundary layer thickness by about 50°/o, and that of skin friction of about 20°/o. Bradshaw (1974), as quoted in Fernholz (1978), discusses semi-empirical relationships for the outer law, skin friction, shape parameters, etc., as a function of free-stream turbulence. The scale of turbulence examined was comparable to the thickness of the boundary layer. The effect of turbulence of much larger or smaller scales is not yet known.

Bailey (1974) states that the critical Re for transition to turbulence decreases with increasing free-stream turbulence. In fact, previous studies of transition to turbulence for spheres are in better agreement once the effects of free-stream turbulence are accounted for. Achenbach (1974) reports on a series of experiments studying the effect of free-stream turbulence on separation phenomena. Although performed under conditions of high blockage (large ratio of sphere diameter d_s to tube diameter d_t), the results clearly show that increased turbulence level in the free-stream decreases the critical Reynolds number (figure 7).
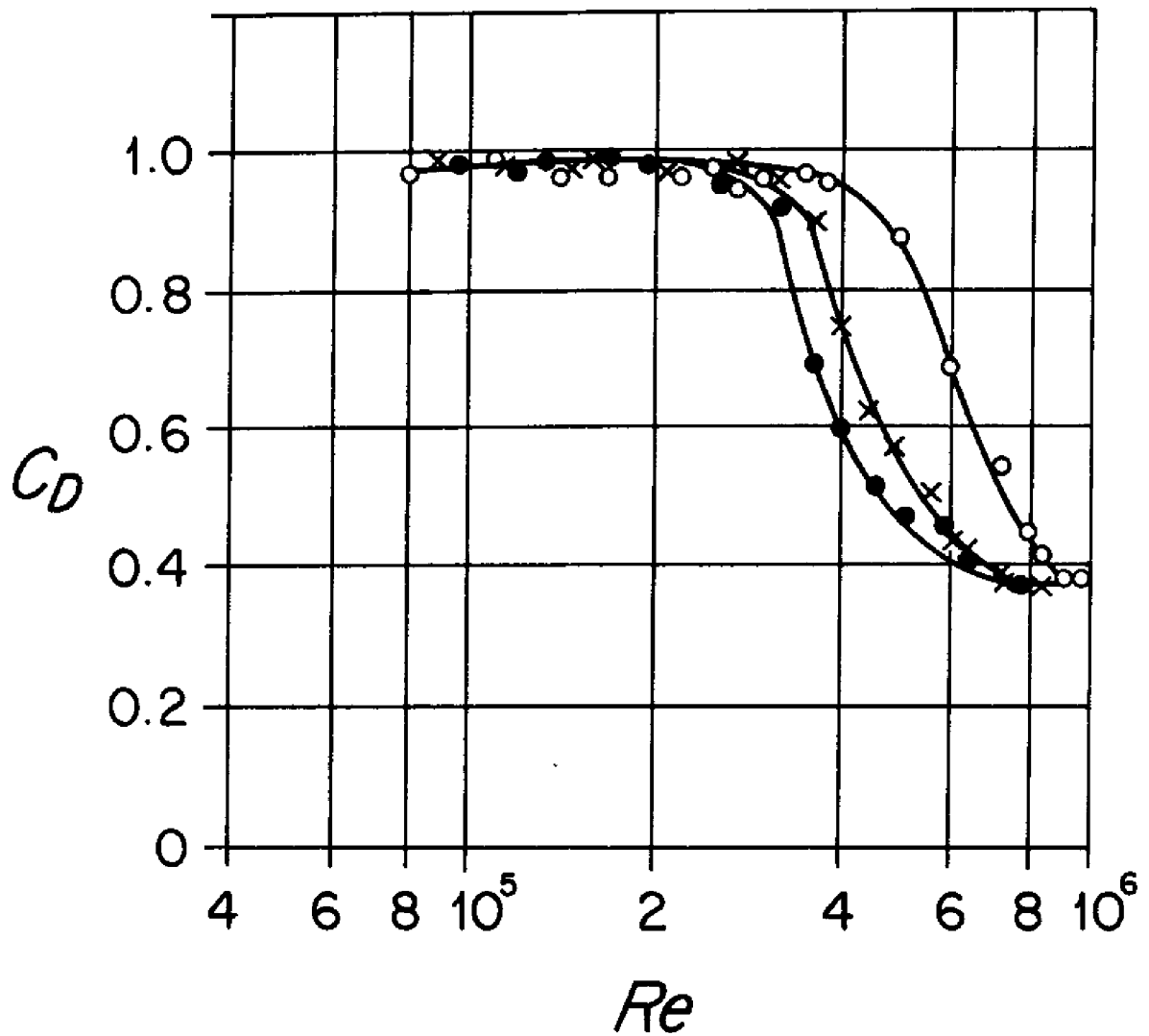
Figure 7. Influence of free-stream turbulence intensity, I, on the drag for a smooth sphere, at a blockage ratio d_s/d_t = 0.9 (after Achenbach, 1974).

Turbulence intensities in the natural environment vary widely. Most reported values are for mid-water measurements, where $I<0.1°/°$. Heathershaw (1976) measured turbulent intensities of up to $18°/°$ in the Irish Sea at 1.0 m off the bottom. Grant (personal communication) typically finds turbulent intensities of $10°/°$ or more in water depths of 20 to 40 m on the shelf. Gross and Nowell (1983) show data indicating turbulent intensities of up to $20°/°$ at a distance 70 cm from the bottom in a tidal flow in Puget Sound. In the surf zone, shear-generated turbulence combines with turbulence associated with breaking waves, probably increasing turbulent intensities over large parts of the surf zone. No measurements of turbulence intensity have been found for this region, however.

Implications of this finding on the behavior of EMCM sensors may be profound. First, free-stream turbulence is ubiquitous in nearshore environments. Second, scales and intensities of such turbulence vary greatly, as a function of position from the breaker zone, and as a function of distance off the bottom. Since it has been demonstrated that turbulence scales on the order of boundary layer thickness are important to turbulent transition, near-bottom measurements might be particularly sensitive to this effect. If boundary layer growth and separation are so sensitive to turbulent scales and intensities, the sensitivity of instruments may change with position in the surf zone and with distance from a boundary. This aspect of current meter sensitivity was briefly addressed during this study. Some previous experimental work on this subject was performed by Bivins (1975), Bivins and Appell (1976), and Griffith (1979).

Boundary layer behavior around a bluff body in a steady or oscillatory flow is strongly dependent on free-stream turbulence. In a poorly defined fashion, both the scales and intensities of free-stream turbulence contribute to this dependence (see previous section). In an attempt to assess the degree of EMCM sensor sensitivity dependence on ambient turbulence levels, we performed some rudimentary experiments on this feature of the calibration. To generate fields of turbulence with various scales and intensities, we used two grids with distinct grid parameters (figure 8) to generate turbulence ahead of the towed sensor in steady flows only. Scale of turbulence was controlled largely by mesh size, while intensity was controlled by tow speed. Tests were not exhaustive, because this task was not originally part of the calibration study. Results strongly suggest the need to perform a more detailed calibration under carefully controlled conditions to determine empirically the scale/intensity dependence of flow around a roughened sphere.

Study of grid-generated turbulence has been largely empirical, motivated by the need to generate well-behaved turbulence for basic studies of this phenomenon in wind tunnels, tow tanks and flumes. Since grid-generated turbulence can approximate isotropic conditions, this technique has been useful for studying the basic properties of isotropic turbulence. Literature on this field is voluminous; we will discuss only a few of the many contributions.

We are interested in generating a shear-free, stationary field of turbulence with definable turbulence intensity and scales. We refer the reader to Corrsin (1963), Comte-Bellot and Corrsin (1966), Naudascher and Farell (1970), Laws and Livesey (1978), and Tan-Atichat, Nagil, and Loehrke (1982) for details of grid-turbulence theory. Although many of the turbulence studies have employed grid-generated turbulence, some have used turbulence
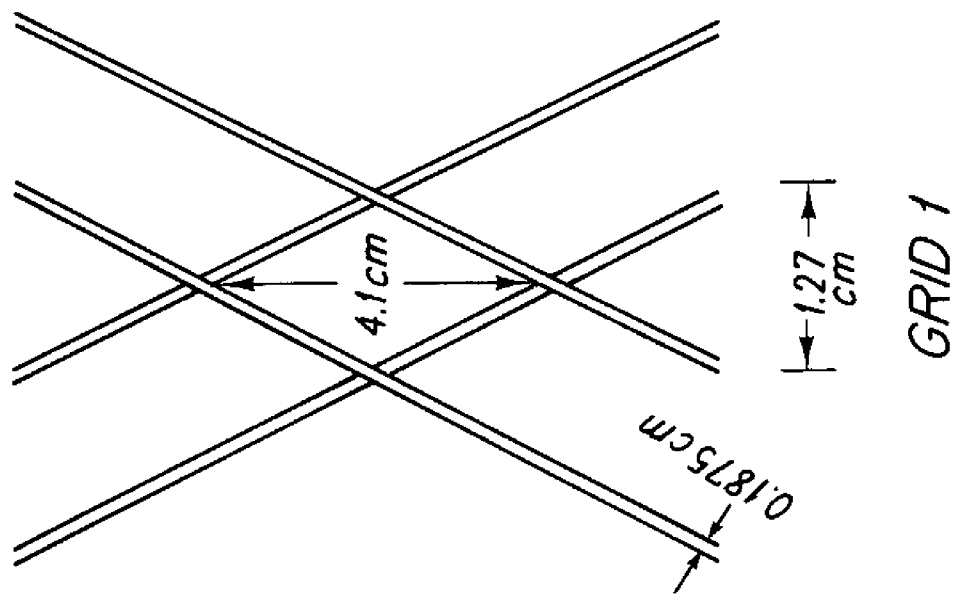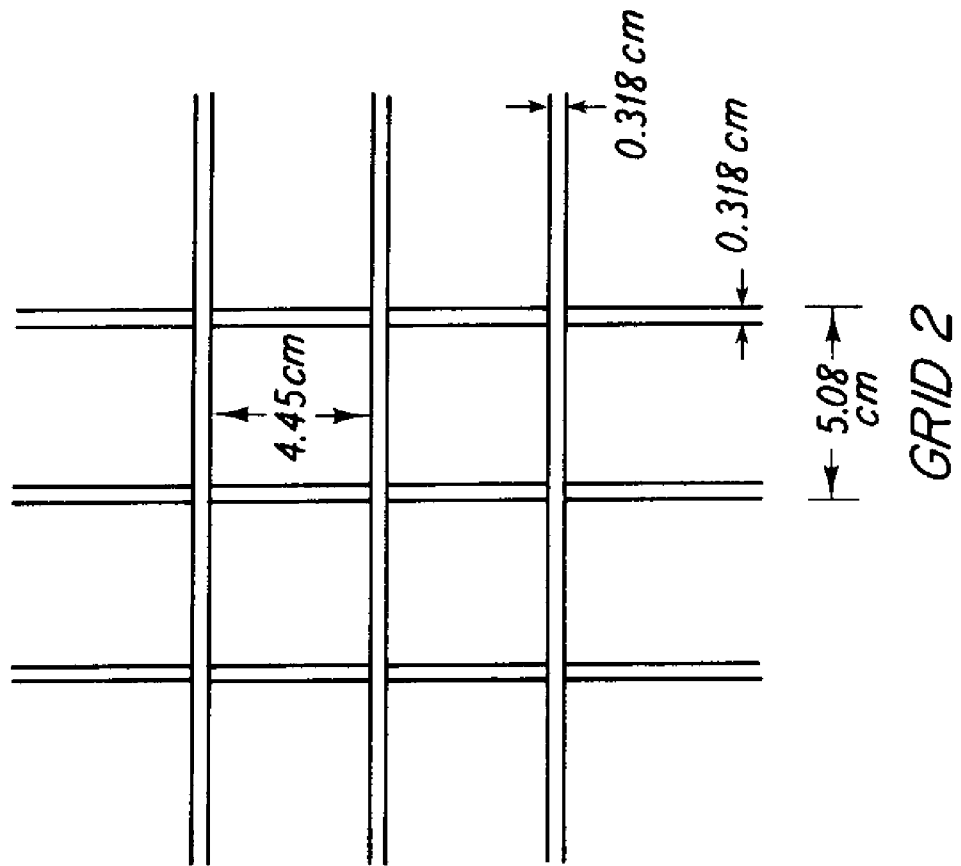
Figure 8. Schematic of grid configuration for two grids used in the grid turbulence experiments.

generated behind a circular cylinder. In particular, Griffiths (1979) used a circular cylinder to minimize effects of flow blockage in the flume. This cylinder-generated turbulence is not shear-free, however, so its use must be carefully designed with sensor averaging volume in mind.

Grid-turbulence can be generated in either a flume or tow-tank. Bivins (1975) and Bivins and Appell (1976) used a submerged jet with a turbulence-generating grid appended to the flow entering the test section. In this situation, it was not possible to avoid near-field effects of grid-generated flow due to the small size of the test section. The present study generated turbulence in a tow-carriage, towing a turbulence grid in front of the flow sensor.

Parameters necessary to define the characteristic scales and intensities of grid-generated turbulence are defined below:

M = mesh size = distance between grid rod centerlines

σ = solidity = projected solid area to total area

 = $\frac{d}{M}$ $(2 - \frac{d}{M})$ for rectangular grid.

d = diameter of grid rod.

L = dominant turbulent length scale.

R_M = mesh Reynolds number.

 = $\dfrac{U_0 \, M}{\nu}$

U_0 = velocity upstream of grid.

u = turbulent fluctuation.

ℓ = wire spacing.

U = free-stream velocity behind grid.

β = porosity = open area/total area.

$\beta = (1-d/\ell)^2$ for rectangular grid.

R_d = local Reynolds number.

$$= \frac{U_o d}{\beta \nu}$$

S = solid area of mesh.

$$= (1-\beta)_\ell^2$$

x = distance downstream from grid.

X_o = virtual origin of grid.

$$\simeq 5M \text{ to } 10M$$

Values of the above parameters for the two grid sections used in this study are provided in table 4.

Experiments show that approximate isotropic conditions in the turbulent flow are achieved when $X/M > 40$. Decay continues in an approximate isotropic form until $X/M = 500$, where X is the downstream coordinate. Generally, when $R_d > 80$, turbulent conditions are satisfied; that is, the individual wakes shed from the biplane grid elements coalesce to form a large turbulent structure. For our flow conditions and geometry, the wake structure is turbulent ($R_d > 80$).

Laws and Livesey (1978) present forms for downstream turbulence intensity and length scale for particular situations. They show:

$$\frac{u^2}{\overline{u'^2}} = b\ (x-x_o)/MK \quad \text{for} \quad M/d \simeq 5$$

Appropriate values for variables in this case are b ~ 100, X_o ~ 10M, K ~ 2.8. For these conditions, $u'/U \simeq 16°/\circ$ for grid 2, and $8°/\circ$ for grid 1. The turbulent length scale, L, is defined as

$$\frac{L}{M} = 2\ (X-X_o)^{1/2}M^{-1/2} \quad \text{for} \quad \frac{M}{d} \sim 5$$

Again, for $X_o \simeq 10M$, we obtain $L \simeq 12$ cm for grid 1, and L ~ 10 cm for grid 2.

TABLE 4

GRID PARAMETERS

	GRID 1	GRID 2
d	0.30 cm	0.32 cm
M	2.3 cm	4.8 cm
ℓ	2.0 cm	4.5 cm
β	0.59	0.86
S	3.6 cm^2	2.6 cm^2
σ	0.34	0.13
M/d	8	15
R_d	51(U_o)	37(U_o)
R_m	230(U_o)	480(U_o)
x/M	19	11

Table 4. Grid parameters for two grids used in grid turbulence studies.

48

These calculations assume a separation of 43 cm between grid 1 and the sensor, and a separation of 53 cm between grid 2 and the sensor. Since $X/M < 40$ in both of these cases, near-isotropic conditions have not been achieved.

Naudascher and Farell (1970) present forms of the turbulence dissipation equations which enable one to calculate turbulence levels behind biplane grids. Calculations using their more complete formulation yield for grid 2 a turbulent intensity $u'/U \sim 8°/°$, at the proper M/d ratio. For grid 1 these levels are lower, close to $3°/°$. This latter reference presents length and intensity measurements as a function of R_d', a grid Reynold's number defined as

$$R_d' = U_o d / \nu$$

$$= \beta' R_d$$

As stated before, blockage is a major problem in tow cart tests utilizing turbulent-generating grids. In such a case, it is desirable to have an independent measure of local velocity so tow cart speed is not used as an indicator of local mean velocity behind the grid. Because this aspect of the study was preliminary, these independent velocity measurements were not obtained. However, data runs where considerable blockage was observed (build-up of fluid on the upstream side of the screen) were not used in this analysis.

CALIBRATION METHODOLOGY

Sixteen current measuring instruments were calibrated as part of this study (table 5), representing five different types of instruments. Instruments were all calibrated eitner at the flume/tow tank facility at WHOI or the ship model test basin at the Ralph Parsons Laboratory at MIT (both described below).

49

Table 5

C/M Type	Probe S/N	Calibration Dates	Calibration Location	Sensor Diameter (cm)	Type of Calibration				
					Steady	Oscillatory	Horizontal Cosine Resp.	Steady and Oscillatory	Steady with Grid
MM551	B498	16/3/82, 12-13/2/83	MIT	10.5	x		x		
"	B499	7/10/82	"	"	x				
"	B500	7/10/82	"	"	x				
"	B501	13/3/82	"	"	x	x		x	
MM 551M	S-468	15-16/9/82	WHOI	4.0	x				
"	S-469	16/9/82, 17/11/82	WHOI/MIT	"	x				
"	S-471	17/9/82, 14/2/83	WHOI	"	x				
"	S-472	16/9/82	"	"	x				
"	S-473	17/9/82	"	"	x				
"	S-538	12/2/83	MIT	4.0	x				
"	S-563	30/10/82, 17-19/11/82, 12/2/83	MIT	"	x	x	x	x	x
512 OEM	S-110	17/12/79	MIT	"	x	x		x	
"	S-112	17/12/79	"	"	x				
"	S-114	17/12/79	"	"	x				
635-9		28/5/82	WHOI	4.0	x				
635-12F	B532	8/10/82, 29/10/82, 30/10/82	MIT	10.5	x	x			

Table 5. Current meter description and calibration tests.

Description of Current Meters

a) MM551: Four Marsh McBirney MM551 current meters were calibrated as part of this program. The MM551 consists of a 10.5 cm diameter electromagnetic sensing sphere (figure 1) which is rigidly connected to a stainless steel pressure case containing signal and power conditioning electronics. Power and recording capabilities are external to the MM551. These were all calibrated at the MIT facility because of their greater sensitivity to ambient electronic noise. A subtle variation in electric field within the WHOI calibration facility (since corrected by Marsh-McBirney, Inc.) prevented their calibration to the desired degree of accuracy.

b) MM551M: Seven Marsh McBirney 551M current meters were calibrated as part of this study. The MM551M is a modified version of the MM551, differing in the use of a 4.0 cm diameter sensing sphere (figure 1) instead of a 10.5 cm sphere. The 4.0 cm diameter sphere is connected to the stainless steel electronics case by a shielded polyurethane-jacketed cable. Similar to the MM551, power and recording are supplied external to the basic sensor and conditioning electronics. Six of the MM551M were calibrated at the WHOI flume facility, while two (including one calibrated at WHOI) were calibrated at the MIT facility.

c) MM512/OEM: Three MM512/OEM current meters were calibrated, and results used for this study. The MM512/OEM is similar to the MM551M, with the main differences being input supply voltage, and instrument sensitivity. Physical dimensions of the MM512/OEM are the same as for the MM551M (figure 1). The MM512/OEM were all calibrated at the MIT facility.

d) Sea Data 635-12F and 635-9: These units are internally powered and recording directional wave gauges, consisting of an electromagnetic flow sensor (Marsh Mcbirney MM551 and MM512/OEM, respectively), a Paroscientific

quartz oscillator pressure sensor, a Sea Data cassette tape recorder, batteries, and electronics. The electronics, cassette tape drive, and batteries are housed inside an aluminum pressure case. The electromagnetic sensors are spherical, with a 10.5 cm diameter sphere for the -12F, and a 4.0 cm diameter sphere for the -9. The Sea Data 635-9 is described in more detail in Aubrey (1981), and its behavior in a field intercomparison described in Grosskopf, Aubrey, Mattie and Mathiesen (1983). One of each of these two units was calibrated, with results used in this analysis. The 635-9 was calibrated at the WHOI facility, while the 635-12F was calibrated at the MIT facility.

Calibration Facilities

Two calibration facilities were used for this study: one at Woods Hole Oceanographic Institution (WHOI) and one at the Massachusetts Institute of Technology (MIT). Both facilities lacked a positive drive system which would assure uniform tow speeds along the tow path; however both have electronic timing systems which measured elapsed time over a specified tow length. In addition, both calibration facilities were carefully observed to assure that there were no significant speed variations along the tow path which would negate the calibration results by introducing a bias through the time constant of the instrument. The drag on the towed current sensors which is transmitted as a torque to the tow cart was not significant enough to cause large deviations in tow speed, except at high velocities (>1.3 m/sec) in the MIT facility. Those runs affected by such instability (shown by large unsteadiness in tow speeds) were not used in the analysis.

a) WHOI calibration facility: The WHOI flume and tow tank facility (figure 9) is 1.2 m wide, 21.3 m long. The tow cart is a self-propelled platform riding on two aluminum rails attached to the top of the tank side
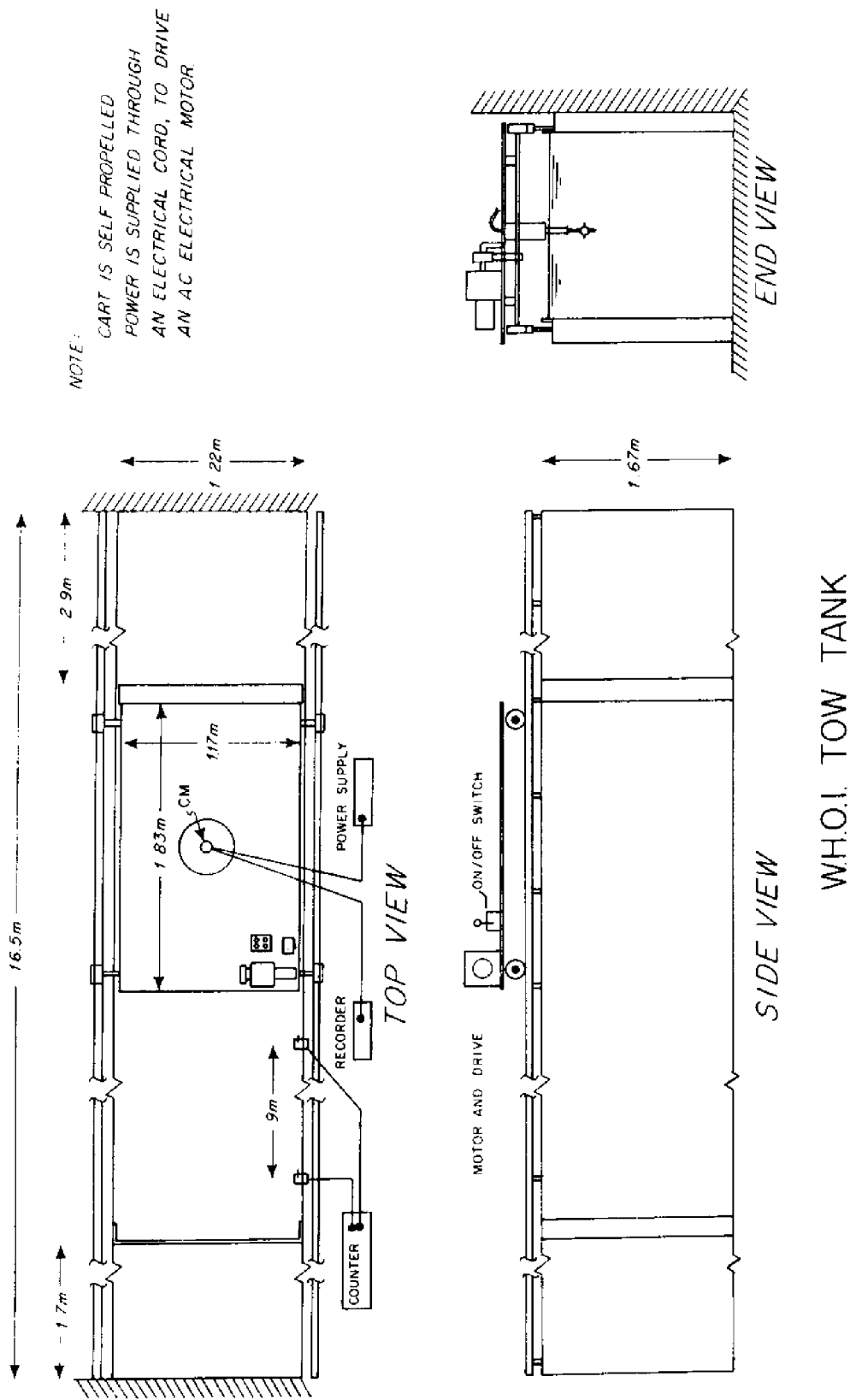
Figure 9. Tow tank and flume facility at the Woods Hole Oceanographic Institution.

53

walls. Power is provided to the cart by an electrical cord pulled by the cart in a shallow trough near the side of the tank. Motion is achieved by frictional contact of two rubber drive wheels with the aluminum rails. Propulsion is provided by a variable speed electrical motor and analog reducing transmission. Cart speed is determined from elapsed time electronically measured between two points along the tank. Two mechanical switches, 9 meters apart, control the start/stop input gates of a Hewlett Packard model No. 5245L frequency counter, yielding elapsed time measurements. The tow cart has a speed range of 0-1.18 m/sec, over the test section of 9 meters. The remainder of the tank length is used to bring the cart to speed, and to slow it down.

The tow tank is 1.67 m high, and calibrations were run with a water depth of between 1.25 and 1.5 m. The flow sensor was attached to the cart via a mounting device which allowed angular rotation about the vertical axis. Orientation in the horizontal plane was performed by aligning the axis defined by a pair of electrodes along channel; to do this orientation, a special tool was designed for use at WHOI. For orientation in the vertical plane, the tow platform was carefully surveyed to assure it was horizontal, and all connecting devices used in this study carefully machined to assure they maintained this horizontal orientation.

b) MIT Calibration Facility: The MIT facility (figure 10) is a ship model test tank, operated by the Ocean Engineering Department of MIT, and located in the basement of the Ralph M. Parsons Laboratory. The tank is 2.61 m wide, 32.93 m long, with a normal water depth of 1.22 m. The test section length is 16.0 m, with a pair of optical sensors determining elapsed time at either end of the test length. The tow cart is a platform suspended above the tank on two metal cylinders running the length of the tank. Propulsion is by

Figure 10. Ship model test facility at the Ralph M. Parsons Laboratory at the Massachusetts Institute of Technology, Cambridge, MA.

55

a tensioned steel band connected to an electric motor by way of three gear boxes in series. Speed changes are performed by changing the gear ratio in one or more of the gear boxes. Power is supplied to the cart via cables towed by the cart; this connection causes some high speed jitter in the cart when the cables are not properly located. Data was carefully checked for such speed instability; if detected the data were not used in the analysis.

Maximum speed possible in the tow tank is four meters/second, although for calibration purposes we did not exceed two meters/second due to the short length of the test section. Signal from the current meters were carried from the tow carriage to the control room via the towed cables, where they were recorded on an analog recorder. This recorder was calibrated thoroughly before each use, from the input jacks on the tow cart through the analog recorder.

Horizontal attitude is referenced to the plane of the tow cart which is parallel to the tow direction. All spacers and mounting devices were carefully machined to assure that this horizontal plane is maintained down to the sensor.

Rotation about the vertical axis is controlled in a manner similar to that used at the WHOI facility. A special tool allows us to orient the axis defined by two electrodes parallel to the tow direction. A machined spacer assembly allows us to rotate the current meter at increments of $5°$ (figure 11).

Oscillatory flow calibration is performed at this MIT tow tank facility using an in-line oscillatory device capable of rotation in the horizontal plane to any desired angle with respect to the mean flow (figure 12). The peak-to-peak amplitude of the horizontal oscillatory motion is 0.5 m maximum, with a variable period from about 1 second to 12 seconds, yielding a maximum

TOP VIEW

END VIEW

M.I.T. SHIP MODEL TEST TANK

Figure 10. Ship model test facility at the Ralph M. Parsons Laboratory at the Massachusetts Institute of Technology, Cambridge, MA.

a tensioned steel band connected to an electric motor by way of three gear boxes in series. Speed changes are performed by changing the gear ratio in one or more of the gear boxes. Power is supplied to the cart via cables towed by the cart; this connection causes some high speed jitter in the cart when the cables are not properly located. Data was carefully checked for such speed instability; if detected the data were not used in the analysis.

Maximum speed possible in the tow tank is four meters/second, although for calibration purposes we did not exceed two meters/second due to the short length of the test section. Signal from the current meters were carried from the tow carriage to the control room via the towed cables, where they were recorded on an analog recorder. This recorder was calibrated thoroughly before each use, from the input jacks on the tow cart through the analog recorder.

Horizontal attitude is referenced to the plane of the tow cart which is parallel to the tow direction. All spacers and mounting devices were carefully machined to assure that this horizontal plane is maintained down to the sensor.

Rotation about the vertical axis is controlled in a manner similar to that used at the WHOI facility. A special tool allows us to orient the axis defined by two electrodes parallel to the tow direction. A machined spacer assembly allows us to rotate the current meter at increments of $5°$ (figure 11).

Oscillatory flow calibration is performed at this MIT tow tank facility using an in-line oscillatory device capable of rotation in the horizontal plane to any desired angle with respect to the mean flow (figure 12). The peak-to-peak amplitude of the horizontal oscillatory motion is 0.5 m maximum, with a variable period from about 1 second to 12 seconds, yielding a maximum

OSCILLATING
MECHANISM

REFERENCE PLATE

10°

GRADUATED PLATE

MOUNTING
SPACER

10 cm

FRICTION DISK ROTATOR

Figure 11.   Spacer designed for horizontal cosine response studies.
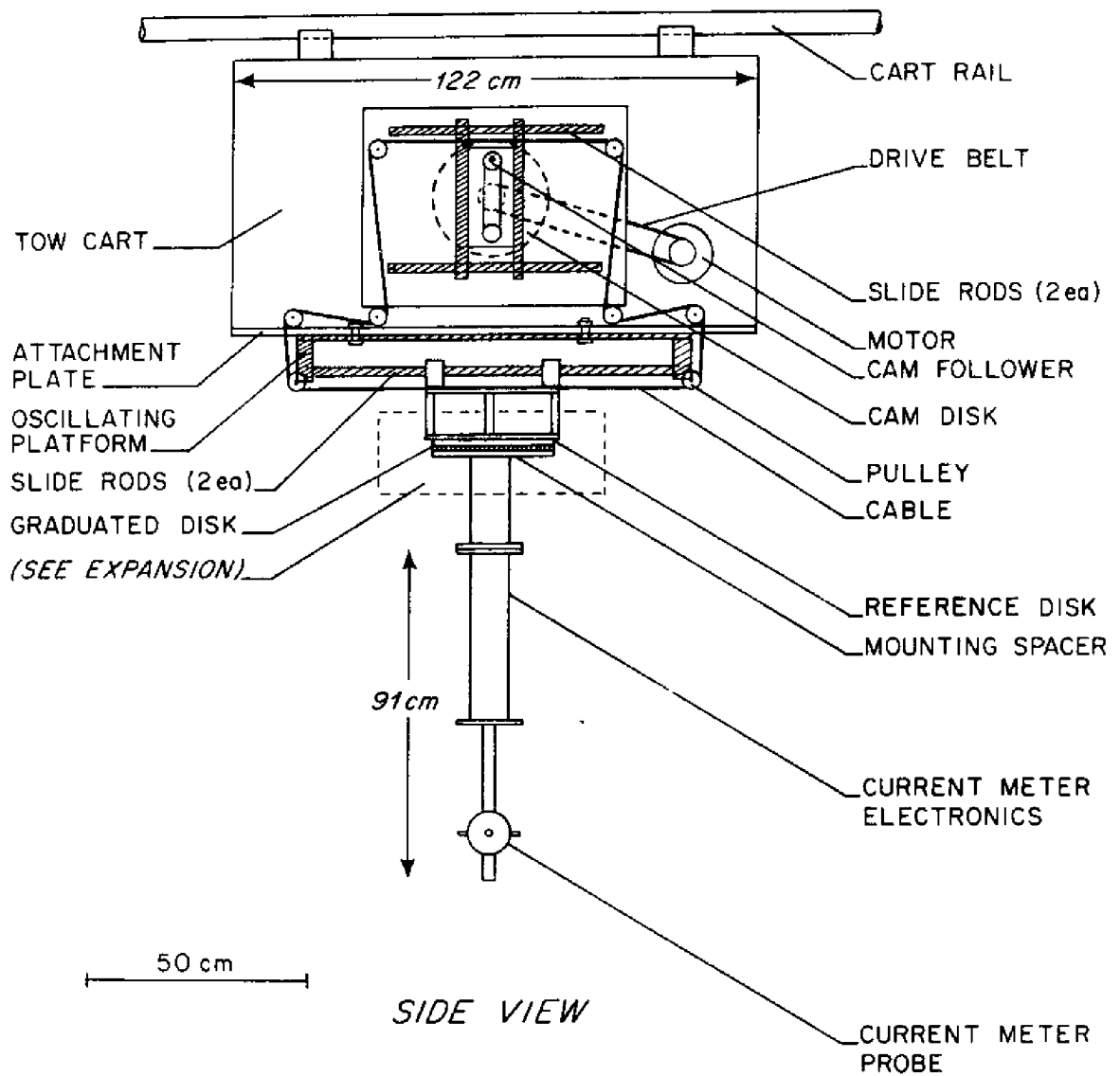
Figure 12. Slosher for generating horizontal oscillatory flows in the MIT
ship model test facility.

orbital velocity of about 1 m/sec. Although it is possible to oscillate the instrument in a vertical plane, this was not performed in the present study. Period control for the oscillator allows a continuum of periods through use of a variable speed motor, but amplitude control is through a cam arrangement which allows 25 distinct peak-to-peak amplitudes of oscillation.

Calibration Errors

Calibration errors can arise from a variety of sources, and ultimately limit the utility of any calibration. Estimates for calibration errors (which must be assessed for each tow geometry as well for each individual instrument) at the WHOI and MIT facilities are included as part of Table 6. Since the WHOI facility was not used for oscillatory calibrations, error estimates are not provided for this situation. Other errors which are instrument specific must be evaluated for each individual current meter.

Errors have been broken up into a variety of types. Construction errors include those associated with the instrument itself, specifically in the orientation of the electrodes and the insertion of the mounting bracket, if any. Orientation errors arise from placing the instrument into the tow tank, with associated hardware for connecting the current sensor to the tow carriage. It also includes the error in determination of cross-channel orientations. Tow cart errors are associated with mechanical problems of the tow cart itself, as well as the depth/width of the channel through which the current meters are towed. Especially for EMCM's, the water depth/channel width must be sufficient to avoid disturbance of the magnetic field in the near-field of the sensor probe (approximately 3 probe diameters away). Instrument electronic errors are generally negligible over the time periods of the calibrations, although improperly specified time constants can affect the higher Reynolds Number

Table 6. Possible Error Sources in Calibration Runs

	WHOI Facility	MIT Facility
A. Construction Deficiencies		
Sensor Alignment		±1° at best
Mount Alignment		±2° in general
B. Orientation Errors		
Rotation about vertical axis	±2°	±2°
Misalignment from horizontal plane	±2°	±2°
Mount motion	negligible	negligible
C. Tow Cart Errors		
Unsteady tow speed	Function of Reynold's number and total drag, less than 1.0 percent rms deviation	
Deviation of tow path from horizontal	negligible	negligible
Wobble in tow cart	"	"
Proximity to sidewall or bottom affecting gain	"	"
Time base errors	"	"
D. Instrument Electronics		
Drift in time	"	"
Time constant affecting high speed runs	"	"
	(for meters and speeds calibrated)	
E. Sampling or Recording Errors		
Inadequate resolution	Function of analog recorder or digitizer; errors less than 1 percent in all cases here.	
Dynamic range constraints	No error for instruments used.	
F. Data Reduction Errors		
Operator bias in reducing data	Same assistant reduced all analog data	
G. Oscillator Errors (Wave Motion)		
Drift in oscillator frequency	—	negligible
Drift in oscillator amplitude	—	"
Oscillator affecting steadiness of tow cart motion	—	Generally negligible, data screened for this effect
H. Cosine Response Errors		
Absolute alignment error	±2°	±2°
Relative alignment error	<1°	<1°

Table 6. Calibration errors for current meters.

calibration runs by averaging over start-up and slow-down portions of the calibrations. These can be difficult to correct. Sampling and recording errors can be either digital or analog, and involve the dynamic range and resolution of the measurements. Data reduction errors can be either analog or digital as well, with operator bias in analog recording being the primary source of these errors. Errors associated with the oscillatory motion (the slosher) are generally mechanical. The stability of the variable speed motor driving the motion must be checked before and after each data run. The oscillator amplitude must be carefully controlled. Finally, for combined steady/oscillatory calibrations, the oscillator must not introduce additional unsteadiness in the steady tow speed which might bias the steady flow results. Cosine response errors can be minimized by using precision machined spacers and other hardware. Although the absolute error due to alignment of the sensor down-channel is still large (order of $\pm 2°$), the relative error between subsequent angles can be reduced by precision machining of angular spacers.

Estimates of the size of each of these errors for the two facilities used in this study have been estimated or calculated based on test results. The two facilities are accurate (within a few percent) enough for the present study, although some improvements could be made. In particular, a positive tow linkage to prevent unsteady cart motions during steady flow calibration is preferred over the less positive linkages present at the WHOI and MIT facilities. In addition, an independent measure of oscillator behavior is preferred over the present assumption (based on observation) of uniform unsteady oscillatory flows. Finally, a longer tow section is required for high Reynolds number flows.

DATA REDUCTION

Most data were obtained from calibrated strip chart recordings of analog voltage derived from instrument response. Two exceptions were the WES 635-9 and the Sea Data 635-12 'F'; which were internally recording onto cassette tapes. For these latter two instruments, data reduction followed different procedures.

For all analog records, any individual run was divided into eight different quantities (figure 13). These were used to relate the various voltages to different kinematical quantities, as follows:

UF = steady forward voltage

$= 0.5 (R7 + R8 - R5 - R6)$

UR = steady reverse voltage

$= 0.5 (R1 + R2 - R3 - R4)$

VR = oscillatory voltage (reverse)

$= 0.5 (R3 - R4)$

VF = oscillatory voltage (forward)

$= 0.5 (R7 - R8)$

V = oscillatory voltage (at rest)

$= 0.25 (R1 + R5 - R2 - R6)$

U = steady voltage (total)

$= 0.25 (R_7 + R_8 - R_3 - R_4)$

where the R_i refer to voltage levels defined in Figure 13. In figure 13, which represents combined steady/oscillatory flows, the steady velocity is initially zero, followed by a reverse steady run, another zero, then a forward steady tow, followed by a final zero. Oscillatory motion is always present in the example. Note that by these definitions, we eliminate all electronic gains
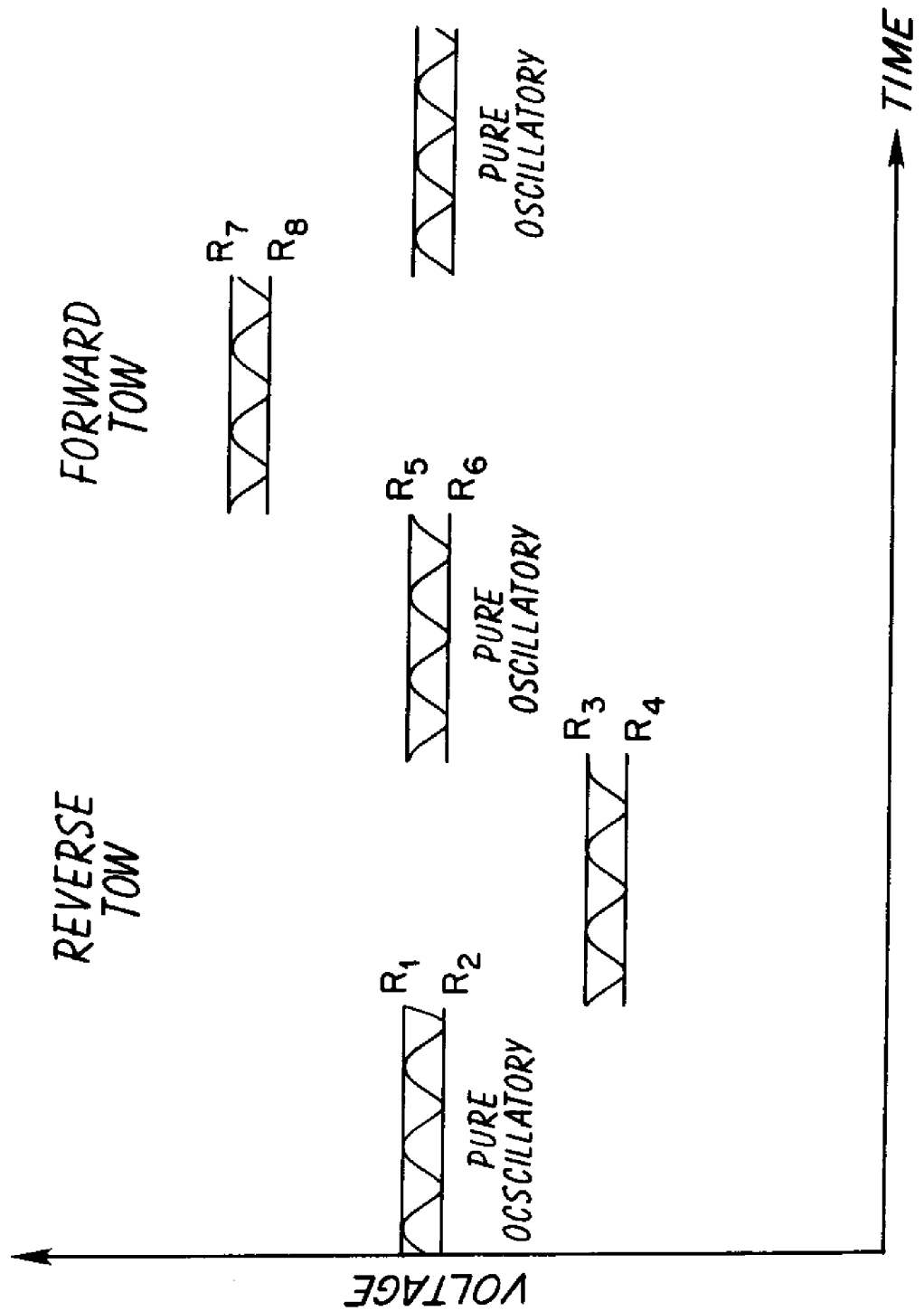
Figure 13. Schematic of data reduction convention for interpreting
stip chart recordings of current meter analog voltage.

since voltages are defined only by relative values, not absolute values. If the data reduction and analysis then yields an apparent (or numerical) offset, this indicates a non-uniform gain. We chose to eliminate electronic offset primarily because this is expected to vary according to deployment location, and thus should be measured carefully during each experimental use.

The above data reduction procedure works regardless of whether the calibration test is for pure steady, pure oscillatory, or combined steady/oscillatory. In the first two cases, some of the eight values will be identical. To minimize differences in calibration resulting from individual bias in strip-chart reading, all strip-charts were interpreted by the same person.

Data analysis for digital data proceeded in a slightly different manner. Steady voltages were calculated from arithmetic means of all data points in the interval of interest. Oscillatory values were derived from calculated variances, $\langle u^2 \rangle$, derived for the interval of interest. If:

$$\langle u^2 \rangle = \text{calculated variance}$$

then: $\quad V = \text{r.m.s. oscillatory voltage}$

$$= (2 \langle u^2 \rangle)^{1/2}$$

STATISTICAL METHODS

The present section discusses statistical techniques applied to calibration data. Emphasis is placed on linear models with one or more independent variables (x), where voltage is the dependent variable (y). Draper and Smith (1966) present a more thorough discussion of these concepts. Independent variables are generally dynamical terms from the equations of motion (see next section), assumed to be known perfectly. The dependent variable is voltage,

which is imperfectly measured with errors assumed to be random. We therefore use univariate rather than multivariate statistical analysis. The simplest model is:

$$y = \sum_{i=0}^{m} \alpha_i \, x_i + \epsilon$$

where m is the number of independent variables, x_0 is unity, and ϵ is an error term.

$$E(\epsilon) = 0$$

$$VAR(\epsilon) = \sigma^2 = \text{constant.}$$

If we have a sample of n observations of each of the variables, we must determine the sample quantities α_m which provide some optimal fit. We choose to minimize the square error:

$$E = \sum_{j=1}^{n} \left\{ \sum_{i=0}^{m} \hat{\alpha}_i \, x_{ij} - y_j \right\}^2$$

where the circonflex ($\hat{ }$) implies an estimated quantity. This minimization proceeds by calculating partial derivatives with respect to each of the coefficients α, and equating each to zero. If we define a mean as follows:

$$\overline{Y} = \frac{1}{n} \sum_{j=1}^{n} Y_j$$

the solution can be represented in matrix form:

$$\underline{\hat{\alpha}} = \underline{a}^{-1} \underline{c}$$

where

$$\underline{\hat{\alpha}} = \begin{bmatrix} \hat{\alpha}_1 \\ \hat{\alpha}_2 \\ \hat{\alpha}_m \end{bmatrix}$$

$$\underline{a} = \begin{bmatrix} (\overline{x_1 x_1} - \overline{x}_1 \overline{x}_1) & (\overline{x_1 x_2} - \overline{x}_1 \overline{x}_2) & \cdots & (\overline{x_1 x_m} - \overline{x}_1 \overline{x}_m) \\ (\overline{x_2 x_1} - \overline{x}_2 \overline{x}_1) & (\overline{x_2 x_2} - \overline{x}_2 \overline{x}_2) & \cdots & (\overline{x_2 x_m} - \overline{x}_2 \overline{x}_m) \\ \vdots & \vdots & & \vdots \\ (\overline{x_m x_1} - \overline{x}_m \overline{x}_1) & \cdot & \cdot & \cdot & (\overline{x_m x_m} - \overline{x}_m \overline{x}_m) \end{bmatrix}$$

$$\underline{c} = \begin{bmatrix} \overline{x_1 y} - \overline{x}_1 \overline{y} \\ \overline{x_2 y} - \overline{x}_2 \overline{y} \\ \vdots \\ \overline{x_m y} - \overline{x}_m \overline{y} \end{bmatrix}$$

Note that estimates of $\underline{\hat{\alpha}}$ are unbiased: $E(\underline{\hat{\alpha}}) = \underline{\alpha}$

where $E(\hat{\gamma})$ represents the expectation of $\hat{\gamma}$. As defined above,

$$E(\epsilon_i \epsilon_j) = \sigma^2 \qquad i=j$$
$$= 0 \qquad i=j$$

We can define a new error matrix $\underline{e}$,

where:

$$\underline{c} = \underline{a}\,\underline{\alpha} + \underline{e}$$

then:

$$\underline{e} = \frac{1}{n} \begin{bmatrix} \displaystyle\sum_{i=1}^{n} (x_{1i} - \overline{x}_1)\,\epsilon_i \\ \vdots \\ \displaystyle\sum_{i=1}^{n} (x_{mi} - \overline{x}_m)\,\epsilon_i \end{bmatrix}$$

Calculating the variance of $\underline{e}$:

$$E(\underline{e}\,\underline{e}^T) = \frac{\sigma^2}{n^2} \begin{bmatrix} \sum\limits_{i=1}^{n} (x_{1i} - \bar{x}_1)(x_{1i} - \bar{x}_1) \cdots \\ \vdots \\ \sum\limits_{i=1}^{n} (x_{mi} - \bar{x}_m)(x_{1i} - \bar{x}_1) \cdots \end{bmatrix}$$

$$= \frac{\sigma^2}{n}\,\underline{a}$$

We can now calculate the variance of our estimates $\underline{a}$:

$$E\left\{ [\underline{\hat{a}} - E(\underline{\hat{a}})][\underline{\hat{a}} - E(\underline{\hat{a}})]^T \right\} = \frac{\sigma^2}{n}(\underline{a}^T)^{-1}$$

Similarly we can determine the variance of a_0:

$$E\left\{ [\hat{a}_0 - E(\hat{a}_0)]^2 \right\} = \frac{\sigma^2}{n}\left\{ 1 + \underline{\bar{x}}\,(\underline{a}^T)^{-1}\,\underline{\bar{x}}^T \right\}$$

Model 1: For the case of one independent variable, $y = \alpha + \beta x + \varepsilon$

where α, β are constants,

ε is a normally distributed error term with zero mean and variance σ^2 (constant). With n observed pairs (x_i, y_i), we estimate α, β, and σ^2. As before we find estimates $\hat{\alpha}$, $\hat{\beta}$ by minimizing the mean square error:

$$MSE = \frac{1}{n} \sum_{i=1}^{n} \left\{ y_i - (\hat{\alpha} + \hat{\beta}\,x_i) \right\}^2$$

The results are:

$$\hat{\alpha} = \bar{y} - \hat{\beta}\,\bar{x}$$

$$\hat{\beta} = \frac{\bar{x}\,\bar{y} - \overline{xy}}{(\bar{x}^2) - \overline{x^2}}$$

The last equations can be rewritten as:

$$\hat{\beta} = \sum_{i=1}^{n} c_i y_i$$

where

$$c_i = \frac{\bar{x} - x_i}{n\bar{x}^2 - n(\overline{x^2})}$$

and

$$\hat{\alpha} = \frac{1}{n} \sum_{i=1}^{n} (1 - c_i n \bar{x}) y_i$$

Defining:

$$S_{xx} = \frac{1}{n} \sum_{i=1}^{n} (x_i - \bar{x})^2 = \overline{(x - \bar{x})^2}$$

Then:

$$c_i = \frac{x_i - \bar{x}}{n S_{xx}}$$

To estimate the variance of $\hat{\beta}$, we rewrite:

$$\hat{\beta} = \sum_{i=1}^{n} c_i (\alpha + \beta x_i + \epsilon_i) = \beta + \sum_{i=1}^{n} c_i \epsilon_i$$

$$VAR(\hat{\beta}) = \frac{\sigma^2}{n S_{xx}}$$

To determine the variance of $\hat{\alpha}$, we write:

$$\hat{\alpha} = \alpha + \frac{1}{n} \sum_{i=1}^{n} \epsilon_i - \bar{x} \sum_{i=1}^{n} c_i \epsilon_i$$

so,

$$VAR(\hat{\alpha}) = \frac{\sigma^2}{n} + \frac{\sigma^2}{n} \frac{\bar{x}^2}{S_{xx}}$$

$$= \frac{\sigma^2}{n} (1 + \frac{\bar{x}^2}{S_{xx}})$$

We can also calculate the covariance of $\hat{\alpha}$ and $\hat{\beta}$:

$$\text{COV}(\hat{\alpha}, \hat{\beta}) = -\frac{\sigma^2}{n} \frac{\bar{x}}{S_{xx}}$$

The sample variance, $\underline{\sigma}^2$, can be determined from:

$$\hat{\epsilon}_i = y_i - \hat{y}_i$$

$$\text{VAR}(\hat{\epsilon}_i) = \hat{\sigma}^2 = \frac{1}{n-2} \sum_{i=1}^{n} (y_i - \hat{y}_i)^2$$

$$= \frac{1}{(n-2)} \sum_{i=1}^{n} (y_i - \hat{\alpha} - \hat{\beta} x_i)^2$$

$$= (\frac{n}{n-2}) \text{VAR}(y) \left\{ 1 - \frac{[\text{COV}(x, y)]^2}{\text{VAR}(x)\ \text{VAR}(y)} \right\}$$

This estimate is unbiased as it can be shown that

$$E(\hat{\sigma}^2) = \sigma^2$$

Model 2:   The second regression model regresses two line segments to a data set, with a cut-off separating two segments at a value x_c. The model takes the simple form:

$$y = \alpha_1 + \beta_1 x + \epsilon_1 \qquad \text{for } x \leq x_c$$
$$y = \alpha_2 + \beta_2 x + \epsilon_2 \qquad \text{for } x > x_c$$

where α_1, α_2, β_1, β_2 are constants, and

$$E(\epsilon_1) = 0 \qquad\qquad \text{VAR}(\epsilon_1) = \sigma_1^2$$

$$E(\epsilon_2) = 0 \qquad\qquad \text{VAR}(\epsilon_2) = \sigma_2^2$$

x_c can be defined in one of two ways.   The first method is to define it as the intersection of the two line segments:

$$x_c = \frac{\alpha_2 - \alpha_1}{\beta_1 - \beta_2}$$

A criterion for determining x_c could be when an _a priori_ guess of x_c yields a solution with x_c close to the iterated value. A better definition of x_c is that which minimizes the total mean square error in the fit. This presents an objective method of determining the location of x_c, while the variances of $\hat{a}_1$, $\hat{a}_2$, $\hat{\beta}_1$ and $\hat{\beta}_2$ allow one to determine if there is any significant difference between $(\hat{a}_1, \hat{\beta}_1)$ and $(\hat{a}_2, \hat{\beta}_2)$. The iterative technique for determining x_c selects velocity increments of 0.10 m/sec up to 1.0 m/sec, calculating σ_T^2 for each. A finer grid is calculated near the minimum value of σ_T^2, to improve the estimate of x_c. The minimum σ_T^2 is found with its associated x_c. These values are compared with a single line segment fit to determine if the coefficients $\hat{a}_1$, $\hat{a}_2$, $\hat{\beta}_1$ and $\hat{\beta}_2$ are significantly different from $\hat{a}$ and $\hat{\beta}$.

Model 3: A bivariate model is also used, of the form:

$$y = \alpha + \beta_1 x_1 + \beta_2 x_2 + \epsilon$$

where x_1 and x_2 are two independent variables, and ϵ is normally distributed with zero mean and variance σ^2.

σ^2 can be related to other statistical parameters to determine the degree of fit, and statistically test the confidence of that parameter. $\hat{\sigma}^2$ is the variance related to the mean square error by a factor of $(\frac{n-2}{n})$, due to the zero mean of ϵ.

σ^2 can be related to the correlation coefficient, R, as follows:

$$\sigma^2 = \frac{n}{n-2} (1 - R^2) VAR(y)$$

Since: $$R^2 = \frac{[COV(x,y)]^2}{[VAR(x) \cdot VAR(y)]}$$

Statistics for R^2 are determined from the F - test:

$$F_{N-p}^{p-1} = \frac{R^2 (N-p)}{(1-R^2)(p-1)}$$

where p is the number of variables (two in the case of a single regression). Tables for the F - test at various significance levels can be found in Abramowitz and Stegun (1972).

An equivalent test can be performed on the estimate of the sensitivity, $\hat{\beta}$, to determine if the fit is significant. Assuming variations of observations about the regression line are normally distributed with a variance given by VAR($\hat{\beta}$), the 100 $(1-\gamma)$°/° confidence limits can be calculated according to the t-test:

$$\hat{\beta} \pm t(N - 2, 1 - \frac{1}{2}\gamma) \sqrt{VAR(\hat{\beta})}$$

t-statistics are calculated in Abramowitz and Stegun (1972).

We can also test the null hypothesis that $\hat{\beta}$ is equal to β_0, where β_0 is some specified value (which could be zero). To do this, we calculate the t-statistic:

$$\tau = (\hat{\beta} - \beta_0) / \sqrt{VAR \hat{\beta}}$$

and compare this calculated $|\tau|$ with t $(n-2, 1-\frac{1}{2}\gamma)$ from a t-table with $(n-2)$ degrees of freedom, for confidence limits of $100(1-\gamma)$°/°.

Similarly, the confidence interval for $\hat{\alpha}$ can be calculated, such that the $100(1-\alpha)$°/° confidence limits for $\hat{\alpha}$ are:

$$\hat{\alpha} \pm t(n-2, 1-\frac{\gamma}{2}) \sqrt{VAR(\hat{\alpha})}$$

We test the null hypothesis that $\hat{\alpha}$ is different from α_0 at the $100(1-\gamma)$°/° level by calculating:

$$\tau = (\hat{\alpha} - \alpha_0) / \sqrt{VAR(\hat{\alpha})}$$

and comparing $|\tau|$ with the t $(n-2, 1-\frac{\gamma}{2})$ found from a table.

Similarly, confidence intervals for $\hat{\beta}$, $\hat{\beta}_2$ can be derived for multiple regression, as well as the fields of confidence for $\hat{\alpha}$, $\hat{\beta}$, $\hat{\beta}_2$, . . . (see Draper and Smith, 1966). We are using a univariate model in our analysis, since we assume the x_i to be independent (and perfectly known), while the y_i are dependent, and imperfectly measured. Consequently, estimates $(\hat{\alpha},\hat{\beta})$ and associated statistics rely on sample variances and correlations. If both x_i and y_i were considered independent, and random, the statistical model would change significantly (in estimating variance of $\hat{\alpha},\hat{\beta}$), and the above formulation would be incorrect.

DIMENSIONAL ANALYSIS

To design an appropriate calibration strategy and interpret the results, we consider the dynamical terms responsible for influencing flow behavior past a sphere. One method for presenting these terms is through ratios of each relevant term with every other term. Another approach is to use dimensional analysis, making use of the Buckingham-π theorem, to select various combinations of dimensionless variables with which to represent the data (see Yalin, 1972, for example). Often the non-dimensional groupings resulting from these methods of analysis can be related to the equations of motion in a straightforward manner.

For mechanical systems, there are generally three parameters which have independent dimensions, since mass (M), length (L), and time (T') are the fundamental independent variables in the equations of motion. We choose to eliminate the dependence on mass (through density, ρ) by dividing through the Navier-Stokes equations to combine the dynamic viscosity (μ) with density to yield a kinematic viscosity (ν). For systems where external pressure

gradients are important, such a manouver is not always appropriate. With the two remaining dimensions, we can always reduce a system with n characteristic parameters to (n-2) independent dimensionless variables. These dimensionless variables are not necessarily unique: additional dimensionless variables can be generated which are dependent on our particular (n-2) variables.

For steady flow, we select as our characteristic parameters the free-stream velocity (U), the kinematic viscosity (ν) and the diameter of the current meter probe (d). One dimensionless grouping is derived from these three variables.

$$\bar{U} = U \cdot f(U, d, \nu)$$

$$\bar{U} = U \cdot f(Ud/\nu)$$

where Ud/ν is the steady Reynolds number (Re) and $\bar{U}$ is an average velocity sensed by the current meter.

For pure oscillatory flow, we have four characteristic parameters: peak-to-peak amplitude of oscillation (A), period of oscillation (T), dimension of current meter (d) and kinematic viscosity (ν). From these parameters, we can choose any two of the following three dimensionless groupings to represent our functional dependence:

$$A/d, \qquad Ad/\nu T, \qquad \nu T/d^2$$

We could choose, for instance:

$$\bar{U} = \frac{A}{T} \ f \ (\frac{A}{d}, \ \nu T/d^2)$$

Each of these dimensionless groupings has a physical significance:

73

a) A/d is the ratio of the unsteady to convective terms (linear vs. nonlinear inertial terms) in the governing equations:

$$\partial/\partial t = 0\ (1/T)$$

$$u\frac{\partial}{\partial x} = 0\ (\frac{A}{T})\frac{1}{d}$$

$$(u\ \partial/\partial x)\ /\ (\partial/\partial t) = A/d$$

If A/d >>1, then $u\frac{\partial}{\partial x} >> \frac{\partial}{\partial t}$ and the flow is quasi-steady. If A/d <<1, $\partial/\partial t$ >> $u\frac{\partial}{\partial x}$ and the nonlinear inertial terms can be neglected. If A/d = 0(1), then both terms must be kept. This parameter in its various representations is sometimes termed the Keulegan-Carpenter number (N_{KC}).

b) $Ad/\nu T$ is analagous to the term Ud/ν in steady flow (R_s). $Ad/\nu T$ then is the oscillatory Reynolds number (R_0), since the maximum orbital velocity (u_m) under a linear water wave is $u_m = \frac{\pi A}{T}$.

If R_s is important for steady flows, then R_0 is expected to be important in unsteady flows, especially if A/d >> 1.

c) $\nu T/d^2$ is a dimensionless ratio of the squares of the linear, oscillatory laminar boundary layer thickness (δ) to current meter dimension, since

$$\delta \simeq \sqrt{\nu T}.$$

This expression is applicable only for small A/d. For turbulent flows, this parameter should have no influence on current meter behavior.

For combined steady and oscillatory flows, we choose the following six characteristic parameters to represent our system: the free stream velocity (U), the peak-to-peak amplitude of oscillation (A), the period of oscillation (T), current meter dimension (d), kinematic viscosity (ν), and angle between steady and oscillatory flow (ϕ). As in the previous cases of pure steady and

pure oscillatory flows, we assume zero vertical component to these flows, since our tests were for purely horizontal flows. In near-surface applications where vertical oscillatory motions are appreciable, this ϕ-dependence must be included.

From these six characteristic parameters, we select four of the possible dimensionless groups available. We list six groups whose importance we can test experimentally:

$$UT/A, \quad UT/d, \quad \nu T/d^2, \quad Ad/T\nu, \quad Ud/\nu, \quad A/d, \quad \phi$$

All groupings have been previously discussed with the exception of UT/d, which is an inverse Strouhal Number (St), and UT/A. St is a description of the shedding frequency for von Karman vortex streets, observed behind a circular cylinder in the range of Reynolds numbers between 60 and 5,000 (Schlichting, 1968). The Strouhal frequency, f_s, depends only on the steady Reynolds number, where:

$$St = f_s d/U$$

The Strouhal number is generally used as a description of a particular property of the flow (defining the shedding frequency). A related frequency parameter can be defined as a flow similarity parameter.

$$S_s = {}^{fd}/_U$$

where f is the frequency of a superimposed flow velocity and U is a steady flow speed. The parameter A/d is related to S_0, when u_m is substituted for the steady velocity U. In this case, $S_0 = d/A$, hence A/d can be viewed as an unsteady inverse Strouhal parameter. UT/A is proportional to the ratio of the steady velocity U, to the maximum orbital velocity, u_m ($= \frac{\pi A}{T}$). McCullough (1978) and others use this non-dimensional quantity to indicate sensor performance.

75

Experiments on EMCM response to ambient flow fields were divided into five primary categories. Specific questions addressed in each category depend on flow characteristics described in the theoretical development presented earlier. An outline of the five major categories with the principal scientific problems addressed under each category is presented below to provide the framework for presentation of results. Implications of these results are addressed in the discussion section.

Category 1: PURE STEADY FLOW

    Model 1: Single segment regression
        a) Comparison of calibration results $(\hat{\alpha}, \hat{\beta})$ with manufacturer's specifications.
        b) Variability in sensitivity between x- and y-axes.
        c) Effect of not scrubbing probe.
        d) Comparison of pre- and post-deployment calibration.
        e) Miscellaneous comparisons.

    Model 2: Double segment regression

    Model 3: Multiple regression results.

    Summary

Category 2: PURE OSCILLATORY FLOW

        a) Comparison of oscillatory and steady sensitivities.
        b) Functional dependence of oscillatory sensitivity.

Category 3: COMBINED STEADY/OSCILLATORY FLOW

        a) Effects of combined steady/oscillatory flow on steady response.
        b) Effects of combined steady/oscillatory flow on oscillatory response.

Category 4: HORIZONTAL COSINE RESPONSE

Category 5: GRID TURBULENCE RESPONSE

To clarify our terminology, we define electronic offset as the measured voltage derived from an immersed sensor with no water flowing past it. Numerical offset refers to the value of $\hat{\alpha}$ calculated from the raw data after removing the electronic offset. For a purely linear instrument, $\hat{\alpha}$ would be

76

zero. A non-zero $\hat{\alpha}$ reflects a nonlinear instrument response. All tests of statistical significance presented here are at the 95% level, unless stated otherwise. Therefore, a "significant" result passes a 95% statistical test. Sensitivity refers to the relationship between voltage and velocity, with units of (volts m^{-1} sec), while gain is the inverse of this quantity. Sensitivity was studied here because voltage was the dependent variable. For field data, gain is the quantity used in analysis to obtain velocity estimates from voltage measurements.

Category 1: PURE STEADY FLOW

Twenty-one current meter calibrations performed on sixteen current meters under steady flow conditions form the basis for interpretation of steady flow behavior. Six of these calibrations were for 10.5 cm diameter spheres; the remainder were for 4.0 cm diameter spheres (Table 5). Number of data points per calibration and speed increment varied slightly as a function of calibration facility (Table 7). In most cases, both axes were calibrated. Expected (manufacturer's) calibration constants are included with the experimental constants. Two models used in the steady calibration studies are discussed separately below.

Model 1: $y = \alpha + \beta'x + \varepsilon$

Dimensional analysis shows the important dimensionless grouping to be the Reynolds number, Re = Ud/ν, where d is the sphere diameter. We can relate the output voltage, y, to the velocity U, x, by incorporating the value d/ν into β', such that $y = \alpha + \beta x + \varepsilon$, where $\beta = \beta'd/\nu$. Alternatives to this development will be discussed shortly. Values for $\hat{\alpha}$, $\hat{\beta}$, and $\hat{\varepsilon}$ were calculated for each run, and estimates of the variance of ε ($\hat{\sigma}^2$) tabulated (Table 7).

TABLE 7. Steady Flow Results - Model 1
(Single Regression)

Date	Probe S/N	Axis	$\hat{\alpha}$	CALCULATED Var($\hat{\alpha}$)	$\hat{\beta}$	Var($\hat{\beta}$)	$\hat{\sigma}^2$	N	R^2	SPECIFICATIONS α	β	Remarks
12/2/83	B498	X	-0.0408	0.000141	1.346	0.000177	0.00179	52	0.995	0	1.667	Post-deployment (probe dirty)
		Y	0.225	0.0233	1.152	0.0339	0.155	52	0.620	0	1.667	
16/3/82	B498	X	-0.0502	0.000135	1.699	0.000282	0.000946	52	0.998	0	1.667	Pre-deployment (probe clean)
		Y	-0.0449	0.0000640	1.684	0.000131	0.000804	46	0.998	0	1.667	
7/10/82	B499	X	-0.0171	0.0000607	1.544	0.0000743	0.000694	50	0.999	0	1.667	
		Y	-0.00269	0.0000767	1.612	0.0000974	0.000968	52	0.998	0	1.667	
7/10/82	B500	X	0.00604	0.0000683	1.511	0.0000862	0.000831	48	0.998	0	1.667	
		Y	-0.00338	0.0000498	1.653	0.0000643	0.000629	50	0.999	0	1.667	
13/3/82	B501	Y	-0.0437	0.000188	1.589	0.000331	0.000715	44	0.997	0	1.667	
16/9/82	S-468	X	-0.0337	0.000183	1.629	0.000337	0.00110	24	0.997	0	1.667	
		Y	0.00635	0.0000295	1.579	0.0000544	0.000178	24	0.9995	0	1.667	
16/9/82	S-468	X	-0.0195	0.000186	1.564	0.000443	0.000509	12	0.998	0	1.667	Probe not scrubbed before run
16/9/82	S-469	X	-0.0335	0.000131	1.623	0.000241	0.000790	24	0.998	0	1.667	WHOI tow tank
		Y	-0.0332	0.000123	1.580	0.000218	0.000714	24	0.998	0	1.667	
17/11/82	S-469	X	-0.0874	0.000159	1.696	0.000202	0.00201	52	0.997	0	1.667	MIT tow tank; after probe repair
		Y	-0.0636	0.000104	1.677	0.000132	0.00131	52	0.998	0	1.667	
17/9/82	S-471	X	-0.0333	0.0000815	1.591	0.000154	0.000503	24	0.999	0	1.667	Pre-deployment
		Y	-0.0295	0.0000681	1.579	0.000121	0.000395	24	0.999	0	1.667	
14/2/83	S-471	X	-0.0490	0.0000906	1.471	0.000116	0.00116	52	0.997	0	1.667	Post-deployment (deployed 4/10/82-3/11/82) (Probes cleaned)
		Y	-0.0525	0.0000670	1.575	0.0000843	0.000848	52	0.998	0	1.667	
17/9/82	S-472	X	-0.0285	0.000278	1.625	0.000498	0.000898	14	0.998	0	1.667	Probe not scrubbed before run
		Y	-0.0162	0.0000365	1.248	0.0000650	0.000121	14	0.9995	0	1.667	
17/9/82	S-472	X	-0.0362	0.000176	1.630	0.000311	0.000912	23	0.998	0	1.667	
		Y	-0.0215	0.0000385	1.577	0.0000679	0.000223	24	0.999	0	1.667	
17/9/82	S-473	X	-0.0316	0.000170	1.622	0.000313	0.00103	24	0.997	0	1.667	
		Y	-0.0447	0.000190	1.625	0.000337	0.00110	24	0.997	0	1.667	
12/2/83	S-538	X	-0.0704	0.0000933	1.487	0.000118	0.00118	52	0.997	0	1.667	
		Y	-0.0612	0.0000641	1.624	0.0000809	0.000816	52	0.999	0	1.667	
18/11/82	S-561	X	-0.0727	0.000109	1.685	0.000138	0.00137	52	0.998	0	1.667	
		Y	-0.0686	0.000102	1.663	0.000130	0.00129	52	0.997	0	1.667	
17/12/79	S-110	Y	-0.0499	0.0000806	1.100	0.0000751	0.000532	24	0.999	0	1.00	
17/12/79	S-112	Y	0.00939	0.0000920	0.898	0.0000964	0.000575	20	0.998	0	1.00	
17/12/79	S-114	Y	-0.0441	0.0008873	1.049	0.0000813	0.000576	24	0.998	0	1.00	
28/5/82	WES 615-9	X	-0.0291	0.000139	2.140	0.000510	0.000950	24	0.998	0	2.00	
		Y	-0.00826	0.000248	1.979	0.000939	0.00180	24	0.995	0	2.00	
8/10/82	615-12'F', B532	X	-0.198	0.0000762	1.225	0.0000998	0.00426	56	0.996	0	1.250	
29/10/82		Y	-0.219	0.0000073	1.239	0.0000219	0.000252	35	0.9995	0	1.250	

Table 7. Steady flow results from Model 1 for current meters calibrated as part of this study.

a) Comparison of calibration results $(\hat{\alpha}, \hat{\beta})$ with manufacturer's specifi-

cations: Manufacturers' specifications of calibration factors α, β (table 7)

were compared with the values from the tow tank tests. All meters were cali-

brated for zero offset (α) by the manufacturer; experimental rms deviation

from this was 0.042 volts (or approximately 2.5 cm/sec in a calibration equa-

tion for U). This offset persists in spite of the data analysis technique used

which eliminates the zero-flow offset (see section on data analysis). The

apparent (numerical) offset of 0.042 volts is an indicator of non-linearity in

sensor response, because the electronic (true) offset was removed during data

analysis (see Data Reduction section).

Sensitivity differed significantly between the manufacturer's specifica-

tions, β, and the calibrations, $\hat{\beta}$. Root-mean-square deviation of $(\beta - \hat{\beta})$ for

all "normal" runs was 0.086 volts/m/sec, or 5.3% of the average manufacturer's

specification. Maximum deviations for "normal" runs of about 11% were observed

on four occasions. The majority of these instruments had not been deployed

prior to calibration, so the instruments should have been close to factory

specifications. "Normal" runs are those where probes were properly scrubbed

before calibration, and which had no biological growth.

b) Variability in sensitivity between x- and y-axes: As an indication of

imbalance, we assessed difference in sensitivity between x- and y-axes of the

same instrument. For "normal" runs (as defined in the previous section),

root-mean-square difference in sensitivity between axes was 0.077 volts/cm/sec,

or about 4.8% of the average manufacturer's sensitivity. Thus sensitivity

imbalances on a particular instrument are of the same order as the differences

in measured sensitivity from the manufacturer's specifications.

c) Effect of not scrubbing probe: New probes, or probes having been stored for a period of time, must be lightly scrubbed before use to prevent dirt or surface films from affecting the sensor performance (Marsh-McBirney operator's manual). As a test of this effect, two new probes were calibrated without performing this scrubbing, then recalibrated immediately after scrubbing. The x-axis of probe S-468 was subjected to this experiment. Sensitivity changed from 1.564 volts/m/sec before scrubbing, to 1.629 volts/m/sec after scrubbing, a difference of 4.2%. Probe S-472 underwent the same test. The x-axis varied from 1.625 to 1.630 volts/m/sec pre- and post-scrubbing, respectively, a change of only 0.3%, (not statistically significant). However, for the y-axis, sensitivity changed from 1.248 to 1.577 volts/m/sec for pre- and post-scrubbing, respectively, a change of 21%, well beyond the 95% confidence limits. This large deviation may have been due to a thin (invisible) film over the y-axis electrodes, changing the conductance of those electrodes. The large error demonstrates the need for careful scrubbing not only when the instrument is new, but also when field activities risk contaminating the probes. We can not speculate on the possible nature of the non-conductive film.

d) Comparison of pre- and post-deployment calibrations: As part of the study, a sensor was calibrated both before and after a deployment which exceeded one month in duration. The probe (S/N B498) was well-calibrated prior to the deployment (3 March 1982). Following the deployment, the instrument was calibrated in its dirty, field-retrieved state. The probe was altered by a filamentous brown algae which had adhered to the metal surfaces of the probe (the stainless steel support and the electrode tips). The sphere itself was protected by antifouling compound, with little significant growth on it. A period of one week elapsed between the time of probe retrieval and calibration.

During this time, the biological growth dried. Consequently, the dried biological fouling might be expected to yield a poorer calibration than living fouling, if conductance differences introduced by dessication are significant. As stated below, however, the effect of biological growth appears to be one of changing the flow characteristics surrounding the electrode, rather than altering conductance between the water and the electrode.

Post-deployment calibration showed a significant departure from pre-deployment calibrations. Root-mean-square difference in sensitivity was 0.45 volts/m/sec, a 26% decrease. Offset for the y-channel was also significantly altered. Error variance for the y-axis of the dirty probe was much higher than for clean probes. Error variance for the dirty x-axis was nearly as low as for the clean probe, suggesting that the difference in sensitivity is not just due to noisy sensor response. The probe was scrubbed subsequently to remove biological growth, and a few calibration points obtained which were in close agreement with the pre-deployment sensitivity. The cause of sensitivity differences appears to be the change in flow behavior due to the presence of biological growth (a hydrodynamic rather than an electrical effect). Permanent degradation of the electrodes did not occur.

e) Miscellaneous comparisons: Probe S-471 was calibrated once at MIT and once at WHOI. Estimates for y-axis sensitivity were nearly identical. Sensitivity of the x-axis differed by 8%, significant at the 95% level. As indicated in table 7, S471 was deployed at the C.E.R.C. Field Research Facility from 4 October 1982 through 3 November 1982. The 8% change in x-axis sensitivity evidently occurred as a result of the deployment, reinforcing the need for periodic recalibration of EMCM's.

Model 2: The second model investigated is a double regression, of the form: $y_1 = \alpha_1 + \beta'_1 x + \epsilon_1$ for $x \leq x_c$

$y_2 = \alpha_2 + \beta'_2 x + \epsilon_2$ for $x > x_c$

We define x_c as that point which minimizes the error variance of the resulting fit. The model is chosen to test the hypothesis that there is a unique Reynolds number which represents transition of the boundary layer to turbulent flow. If this dynamical effect is dominant, then the minimum error variance should be located near $(Re)_c$. If the transition is not present in this Reynolds number regime, or if its effect does not influence the calibration results, then x_c should shift from instrument to instrument.

Improvement in fit to data (lowered error variance) will necessarily result from use of this double regression model, in a manner similar to that occurring using higher order polynomial fits. The improved fits, even if of no particular dynamical significance, still may be useful for calibration purposes. The order of the polynomial or number of line segments one assigns to calibrations depends on the ultimate use of the data. If the error variance is low enough for modeling requirements using a single regression model, then the extra computational cost associated with an improved fit may not be worthwhile. One must be careful to use a higher order model only if improvement in fit is significant.

As in the single regression case, we set the independent variable, x, to be the velocity U, instead of the dynamically correct Re, such that:

$$\beta_1 = d/\nu \ \beta'_1$$

$$\beta_2 = d/\nu \ \beta'_2$$

Regression coefficients $\hat{\beta}_1$ and $\hat{\beta}_2$ are tabulated (Table 8), along with values of $\hat{\sigma}^2$ and x_c. In all cases, $\hat{\sigma}^2$ is less than that of a single regression. There is no clear pattern for the behavior of $\hat{x}_c$. For the 10.5 cm diameter spheres, the mean value of $\hat{x}_c$ is 0.96 m/sec (Re = 1×10^5). For the smaller 4.0 cm spheres, the average value of $\hat{x}_c$ is 0.78 m/sec (Re = 3.1×10^4).

TABLE 8. Steady Flow Results – Model 2 (Double Regression)

Date	Probe S/N	Axis	$\hat{\beta}-\gamma_1$	$\hat{\beta}_1$	$\hat{\beta}_1+\gamma_1$	Var($\hat{\beta}_1$)	$\hat{\beta}_2-\gamma_2$	$\hat{\beta}_2$	$\hat{\beta}_2+\gamma_2$	Var($\hat{\beta}_2$)	X_c m/sec	(Rel)$_c$	$\hat{\sigma}^2$
16/3/82	B498	X	1.434	1.552	1.669	0.00345	1.624	1.697	1.770	0.00132	0.5	52,500	0.000674
		Y	1.340	1.502	1.605	0.00263	1.655	1.696	1.737	0.000419	0.4	42,000	0.000419
12/2/83	B498	X	1.349	1.378	1.407	0.000211	0.700	1.029	1.359	0.0271	1.2	126,000	0.00124
		Y	1.380	1.404	1.427	0.000141	1.156	1.266	1.377	0.00302	1.1	115,000	0.000317
7/10/82	B499	X	1.549	1.566	1.583	0.0000726	1.140	1.278	1.416	0.00475	1.2	126,000	0.000344
		Y	1.603	1.624	1.646	0.000114	1.364	1.440	1.517	0.00145	1.1	115,000	0.000492
7/10/82	B500	X	1.521	1.538	1.555	0.0000716	1.273	1.354	1.435	0.00164	1.1	115,000	0.000174
		Y	1.681	1.693	1.704	0.0000344	1.292	1.438	1.583	0.00531	1.2	126,000	0.000213
13/3/82	B501	Y	1.476	1.516	1.556	0.000401	1.595	1.770	1.944	0.00760	0.80	84,000	0.000357
8/10/82 (635-12F)	B532	X	1.154	1.251	1.348	0.00234	1.069	1.159	1.249	0.00201	0.9	94,500	0.00200
		Y	1.209	1.238	1.267	0.000216	0.901	1.118	1.335	0.01180	0.7	73,500	0.0000801
16/9/82	S-468	X	1.500	1.542	1.583	0.000428	1.632	1.801	1.970	0.00715	0.7	28,000	0.000573
		Y	1.593	1.654	1.716	0.000946	1.557	1.586	1.614	0.000206	0.4	16,000	0.000138
16/9/82	S-469	X	1.533	1.554	1.575	0.000112	1.283	1.604	1.926	0.0258	1.0	40,000	0.000221
		Y	1.498	1.526	1.555	0.000200	1.934	2.030	2.126	0.0230	1.0	40,000	0.000200
17/11/82	S-469	X	1.547	1.559	1.571	0.0000365	1.746	1.813	1.880	0.00112	1.0	40,000	0.000362
		Y	1.557	1.580	1.603	0.000134	1.612	1.667	1.722	0.000755	1.0	40,000	0.000464
17/9/82	S-471	X	1.511	1.538	1.565	0.000185	1.713	1.813	1.914	0.00254	0.9	36,000	0.000157
		Y	1.465	1.490	1.515	0.000154	1.605	1.638	1.671	0.000274	0.4	16,000	0.000153
14/2/83	S-471	X	1.365	1.393	1.420	0.000191	1.447	1.499	1.552	0.000692	0.9	36,000	0.000845
		Y	1.466	1.497	1.528	0.000237	1.572	1.617	1.662	0.000503	0.9	36,000	0.000542
17/9/82 (Not scrubbed)	S-472	X	1.567	1.609	1.652	0.000455	1.512	1.763	2.013	0.0157	0.75	30,000	0.000596
		Y	1.207	1.232	1.256	0.000146	1.189	1.325	1.462	0.00466	0.95	38,000	0.0000738
17/9/82	S-472	X	1.499	1.542	1.584	0.000451	1.625	1.773	1.921	0.00550	0.75	30,000	0.000480
		Y	1.484	1.510	1.536	0.000168	1.598	1.645	1.669	0.000312	0.60	24,000	0.0000880
17/9/82	S-473	X	1.529	1.556	1.582	0.000174	1.720	1.733	2.267	0.0711	1.0	40,000	0.000490
		Y	1.469	1.504	1.540	0.000316	1.694	1.819	1.945	0.00395	0.8	32,000	0.000340
12/2/83	S-538	X	1.319	1.346	1.373	0.000182	1.551	1.578	1.606	0.000187	0.7	28,000	0.000324
		Y	1.488	1.511	1.534	0.000134	1.645	1.678	1.711	0.000269	0.7	28,000	0.000427
18/11/82	S-563	X	1.498	1.524	1.551	0.000176	1.719	1.760	1.801	0.000426	0.8	32,000	0.000490
		Y	1.540	1.556	1.573	0.0000707	1.640	1.697	1.753	0.000798	1.0	40,000	0.000349
17/12/79	S-110	Y	0.949	0.964	0.978	0.0000519	1.116	1.139	1.150	0.0000763	0.8	32,000	0.0000463
17/12/79	S-112	Y	0.928	0.944	0.959	0.0000615	0.759	0.931	1.102	0.00732	1.0	40,000	0.000424
17/12/79	S-114	Y	0.911	0.922	0.933	0.000314	1.042	1.072	1.102	0.000226	0.5	20,000	0.000163
28/5/82	WES 635-9	X	2.087	2.154	2.222	0.00114	2.250	2.410	2.570	0.00639	0.6	24,000	0.000499
		Y	1.821	1.915	2.008	0.00218	1.731	1.919	2.107	0.00883	0.4	16,000	0.001541

Table. 8   Steady flow results from Model 2 for current meters calibrated as part of this study. $\hat{\gamma}_1$ and $\hat{\gamma}_2$ are 95% confidence extremes calculated from an F-test.

83

The spread in these values of $\hat{x}_c$ is so great that little significance can be attached to them. In other words, $\hat{x}_c$ does not appear to represent a well-defined transition from laminar to turbulent flow around the sphere.

For most smaller spheres, the higher Reynolds number segment has a higher sensitivity than the lower segment. This is not necessarily true for the larger (10.5 cm diameter) spheres. In most cases, values of $\hat{\beta}_1$ are significantly different from $\hat{\beta}_2$.

Results of the pre- and post-deployment calibrations of B498 show similar trends to those found in the single regression analysis. Largest deviation of the "dirty" response from the "clean" response is in the higher Reynolds' number segments. This suggests that the post-deployment change in sensitivity was hydrodynamic; the biological growth distorted the flow field such that the flow deviation was more pronounced at higher Re.

Model 3: A model of the form:

$$y = \alpha + \beta_1 x_1 + \beta_2 x_2 + \varepsilon$$

was used for the analysis. The two independent variates x_1 and x_2 are:

$$x_1 = Ud/\nu = Re$$

$$x_2 = (Ud/\nu)^{-1/2} = Re^{-1/2}$$

Motivation for this regression is to evaluate the dependence of the output voltage on the laminar boundary layer thickness, which is proportional to $(Re)^{-1/2}$. Results from this regression show no significant improvement in fit compared to Model 1, based on x_1 alone. This result suggests that the probe is either insensitive to the thin laminar boundary layer, or the boundary layer structure is turbulent, and the dependence on $(Re)^{-1/2}$ no longer holds.

Summary:

The three models applied to pure steady flow calibrations can be summarized as follows:

a) For steady flow around clean probes, error variances average 0.00098 volts ^{2} (for single regression model, equivalent to a standard deviation of 3 cm/sec in velocity), and an average of 0.000579 volts^2 (for double segment regression, equivalent to a standard deviation of 2 cm/sec in velocity).

b) Manufacturer specifies accuracies of $\pm$ 2%. Deviation from specified linearity exceeded the manufacturer's specifications.

c) Fouling, dirty electrodes, and other situations can degrade sensor performance more than stated above.

Category 2: PURE OSCILLATORY FLOW

As an intermediate step to determining the response of electromagnetic sensors to combined steady and oscillatory flows, we calibrated four sensors under pure oscillatory flow conditions (tables 9 and 10). Wave periods and oscillation amplitudes spanned the full range of values discussed under the Methods section, with oscillatory velocities ranging from 0.04 to 0.5 m/sec. The number of pure oscillatory runs varied from 20 to 40.

a) Comparison of oscillatory and steady sensitivities: First, each sensor was examined by observing the dependence of peak voltage to maximum oscillatory velocity (table 9). For S110x, the oscillatory sensitivity was 1.024. For S110y the oscillatory sensitivity was 1.091 versus 1.100 in pure steady, an excellent agreement. For B501y, the oscillatory sensitivity is 1.688, versus 1.589 for pure steady flow. This 6% increase is significant. For B532x, oscillatory sensitivity is 1.20, versus a steady value of 1.225. For B532y, oscillatory sensitivity is 1.22, while the steady value is 1.239.

85

TABLE 9

UNSTEADY EFFECTS ON UNSTEADY SENSITIVITY

PURE OSCILLATORY FLOW

(PEAK VOLTAGE VS. PEAK VELOCITY)

	AXIS	$\hat{\alpha}$	VAR$(\hat{\alpha})$	$\hat{\beta}$	VAR $(\hat{\beta})$	$\hat{\sigma}^2$	R^2	N
S110	X	0.00288	1.12×10^{-5}	1.024	3.59×10^{-4}	6.77×10^{-5}	0.9946	18
	Y	0.00676	1.38×10^{-6}	1.091	5.93×10^{-5}	1.41×10^{-5}	0.9986	30
B532	X	0.0232	1.85×10^{-5}	1.20	1.5×10^{-3}	1.85×10^{-4}	0.978	24
	Y	0.0150	0.761×10^{-5}	1.22	5.8×10^{-4}	6.94×10^{-5}	0.992	23
B501	Y	0.00468	2.12×10^{-5}	1.688	9.36×10^{-4}	4.74×10^{-5}	0.997	20
S563	X	0.0229	0.643×10^{-4}	1.695	5.33E-4	1.4×10^{-6}	0.997	20
	Y	0.0262	0.195×10^{-4}	1.507	1.84E-4	4.2×10^{-5}	0.999	20

Table 9. Unsteady effects on unsteady sensitivity for pure oscillatory flow, calculated from the oscillatory velocity, u_m, and observed voltage.

PROBE	AXIS	(A/d)	$(Re)_0$	Tv/d^2	$\hat{\beta}$ (table 9)
S563 Mean Sensitivity	X	1.873	1.873	1.873	1.695
(N=40) $\hat{\alpha}$	X	2.053	1.987	1.745	
VAR $(\hat{\alpha})$	X	0.00197	0.00173	0.00618	
$\hat{\beta}$	X	-0.500	-0.224×10^{-4}	0.154×10^{-4}	
VAR $(\hat{\beta})$	X	0.0110	0.390×10^{-10}	0.745×10^{-10}	
$\hat{\sigma}^2$	X	0.0108	0.0143	0.0209	
R^2	X	0.558	0.418	0.150	
S563 Mean Sensitivity	Y	1.720	1.720	1.720	1.507
(N=40) $\hat{\alpha}$	Y	1.971	1.808	1.642	
VAR $(\hat{\alpha})$	Y	0.00354	0.00320	0.0153	
$\hat{\beta}$	Y	-0.6921	-0.149×10^{-4}	0.906×10^{-5}	
VAR $(\hat{\beta})$	Y	0.0197	0.406×10^{-10}	0.176×10^{-9}	
$\hat{\sigma}^2$	Y	0.0195	0.0352	0.0447	
R^2	Y	0.575	0.232	0.0252	
B501 Mean Sensitivity	Y	1.736	1.736	1.736	1.688
(N=20) $\hat{\alpha}$	Y	1.796	1.783	1.793	
VAR $(\hat{\alpha})$	Y	0.00141	0.00133	0.00760	
$\hat{\beta}$	Y	-0.0537	-0.335×10^{-5}	-104.1	
VAR $(\hat{\beta})$	Y	0.941×10^{-3}	0.535×10^{-11}	$2.48 \times 10^{+4}$	
$\hat{\sigma}^2$	Y	0.00273	0.00299	0.00358	
R^2	Y	0.277	0.208	0.0518	
S110 Mean Sensitivity	Y	1.198	1.198	1.198	1.091
(N=29) $\hat{\alpha}$	Y	1.380	1.312	1.140	
VAR $(\hat{\alpha})$	Y	0.000824	0.000916	0.00343	
$\hat{\beta}$	Y	-0.0712	0.00003	13.873	
VAR $(\hat{\beta})$	Y	0.000100	0.0000	175.4	
$\hat{\sigma}^2$	Y	0.004862	0.00795	0.0134	
R^2		0.652	0.431	0.0390	
B532 Mean Sensitivity	X	1.230	1.230	1.230	1.20
(N=23) $\hat{\alpha}$	X	1.564	1.494	0.732	
VAR $(\hat{\alpha})$	X	0.0191	0.0112	0.0347	
$\hat{\beta}$	X	-0.342	-0.209×10^{-4}	866.0	
VAR $(\hat{\beta})$	X	0.0147	0.409×10^{-8}	0.897×10^{-5}	
$\hat{\sigma}^2$	X	0.1222	0.112	0.121	
R^2	Y	0.266	0.327	0.275	
B532 Mean Sensitivity	Y	1.093	1.093	1.093	1.22
(N=23) $\hat{\alpha}$	Y	1.348	1.264	0.948	
VAR $(\hat{\alpha})$	Y	0.00502	.00354	0.0123	
$\hat{\beta}$	Y	-0.246	-0.129×10^{-4}	$0.245 \times 10^{+3}$	
VAR $(\hat{\beta})$	Y	0.00348	0.122×10^{-10}	0.292×10^5	
$\hat{\sigma}^2$	Y	0.0291	0.0323	0.0485	
R^2	Y	0.453	0.393	0.0888	

Table 10. Unsteady effects on unsteady sensitivity for pure oscillatory flow, as a function of the nondimensional parameters A/d, (Re)$_0$, and Tv/d^2.

The average difference in sensitivity between steady and oscillatory calibrations is 2.6%, within the uncertainties in the calibrations. No consistent pattern of undersensitivity was observed in the calibrations.

b) Functional dependence of oscillatory sensitivity: Dependence of oscillatory sensitivity was also calculated for A/d, $(Re)_o$, and $T\nu/d^2$ (table 10), for six axes of the four current meters tested. Mean sensitivity for each of the axes was determined, consistently showing an increased sensitivity compared to the value calculated from plots of u_m versus voltage (table 9). This increase in sensitivity is partly numerical, resulting from lack of inclusion of a numerical offset in this calculation. This difference in mean sensitivity averaged 8.4% for the four different sensors, the greatest difference being in S563. This difference in sensitivity resulting from lack of inclusion of numerical offset demonstrates the important role of $\hat{\alpha}$.

For all four sensors, sensitivity is significantly correlated with A/d and $(Re)_o$, but not with $T\nu/d^2$. This latter lack of dependence suggests the unimportance of laminar boundary layer thickness ($\sqrt{\nu T}$) on oscillatory flow past spheres with given roughness and for $A/d \gg 1$. In most cases, sensitivity decreases with increasing A/d and increasing $(Re)_o$, a behavior which has no obvious physical explanation.

In addition to the standard statistical model tests, the interdependence of all three dimensionless groupings with oscillatory sensitivity was examined using T^2-statistics (Cooley and Lohnes, 1971). These statistics also show that gain is dependent on both A/d and $(Re)_o$, but not $\nu T/d^2$.

Category 3: COMBINED STEADY/OSCILLATORY FLOW

To simulate surf zone and inner shelf hydrodynamics in the laboratory environment, tests were conducted using combined steady and oscillatory motions. Steady motions were simulated using the tow cart at the MIT facility,

while oscillatory motions were created with a specially-constructed slosher
(figure 12). Oscillatory motion was rectilinear in a horizontal plane to
simulate shallow water orbital motions. Most tests were conducted with
colinear steady and oscillatory motions; some were conducted with oscillatory
motions at right angles to the steady motion. Two current meters underwent
this extensive steady/oscillatory testing: a sensor with a 10.5 cm diameter
sphere (B501) and a sensor with a 4.0 cm diameter sphere (S563).

Results are divided into two sections: a) the effect of combined steady/
oscillatory flow on steady response (table 11), and b) the effect of combined
steady/oscillatory flow on oscillatory response (table 12). Pure oscillatory
and pure steady sensitivities are listed in tables 9 and 7, respectively, for
comparison.

a) Effects of combined steady/oscillatory flow on steady response: Steady
flow calculations (table 7) using Model 1 show a sensitivity ($\hat{\beta}$) of 1.685 for
the x-channel of S563, and 1.589 for the y-channel of B501. These can be
contrasted to the results of combined steady/oscillatory tests (table 11).
For S563, the mean steady sensitivity is 1.538 when towed in the reverse
direction, and 1.533 when towed in the forward direction. This difference is
not statistically significant, so we can assign an average sensitivity of
1.535 to this instrument in these tests, representing a 9.9% reduction from
the pure steady value. The calculated $\hat{\beta}$ relating the steady sensitivity to
different non-dimensional groupings is significantly different from zero only
for $(Re)_s$ and UT/A, but not for A/d, $(Re)_o$ or UT/d (see table 13 for F-test
values differentiating significance levels as a function of number of degrees
of freedom).

TABLE 11

UNSTEADY EFFECTS ON STEADY SENSITIVITY

COMBINED STEADY/OSCILLATORY FLOWS

PROBE	VARIABLE	AXIS	A/d		(Re)$_o$		UT/d		(Re)$_s$		UT/A	
			Reverse	Forward	Reverse	Forward	Reverse	Forward	Reverse	Forward	Reverse	Forward
S563	Mean Sensitivity	X	1.538	1.533	1.538	1.533	1.538	1.533	1.538	1.533	1.538	1.533
(N=52)	$\hat{\alpha}$	X	1.568	1.551	1.562	1.551	1.529	1.525	1.469	1.461	1.516	1.515
	VAR$(\hat{\alpha})$	X	0.000252	0.000269	0.000198	0.000207	0.000834	0.000838	0.000156	0.000141	0.107E-3	0.114E-3
	$\hat{\beta}$	X	-0.0114	-0.00700	-0.658E-5	-0.491E-5	1.680	1.645	0.319E-5	0.339E-5	0.646E-3	0.547E-3
	VAR$(\hat{\beta})$	X	0.0000264	0.0000282	0.921E-11	0.965E-11	30.59	30.74	0.252E-12	0.228E-12	0.408E-7	0.434E-7
	$\hat{\sigma}^2$	X	0.00354	0.00378	0.00356	0.00373	0.00389	0.00391	0.00215	0.00195	0.00323	0.00344
	R^2	X	0.0899	0.0336	0.0860	0.0476	0.0018	0.0018	0.448	0.503	0.170	0.121
B501	Mean Sensitivity	Y		1.484		1.484		1.484	1.484			1.484
(N=24)	$\hat{\alpha}$	Y	1.453		1.464		1.417		1.414		1.454	
	VAR$(\hat{\alpha})$	Y	0.00252		0.00176		0.960E-3		0.00121		0.000913	
	$\hat{\beta}$	Y	0.0243		0.120E-5		0.00171		0.130E-5		0.00261	
	VAR$(\hat{\beta})$	Y	0.00138		0.499E-11		0.490E-6		0.337E-12		0.508E-5	
	$\hat{\sigma}^2$	Y	0.00503		0.00507		0.00387		0.00403		0.00479	
	R^2	Y	0.0232		0.0157		0.249		0.217		0.0695	

Table 11. Unsteady effects on steady sensitivity, for combined steady/oscillatory flows. Tests were run in both the forward and reverse directions. Dependence on nondimensional groupings A/d, (Re)$_o$, UT/d, (Re)$_s$, and UT/A is illustrated.

90

TABLE 12

UNSTEADY EFFECTS ON UNSTEADY SENSITIVITY

COMBINED STEADY/OSCILLATORY FLOWS

PROBE S563, VARIABLE X, CHAN X

	u_H Forward (N=52)	u_H Reverse (N=52)	$(Re)_s$ Forward	$(Re)_s$ Reverse	UT/A Forward	UT/A Reverse	A/d Forward	A/d Reverse	UT/d Forward	UT/d Reverse	$(Re)_o$ Forward	$(Re)_o$ Reverse
Mean Sensitivity			1.867	1.898	1.867	1.898	1.867	1.898	1.867	1.898	1.867	1.898
$\hat{\alpha}$	0.0148	0.0188	1.490	1.587	1.471	1.559	2.20	2.300	1.261	1.495	2.157	2.214
$VAR(\hat{\alpha})$	0.0000227	0.0000211	0.0164	0.0140	0.00186	0.00219	0.0169	0.0119	0.0521	0.0459	0.0131	0.00977
β	1.564	1.540	0.177E-4	0.145E-4	0.0119	0.0102	-0.126	-0.152	121.7	80.79	-0.771E-4	-0.842E-4
$VAR(\hat{\beta})$	0.00153	0.00142	0.266E-10	0.227E-10	0.706E-6	0.835E-6	0.00177	0.00125	1911.	1683.	0.607E-9	0.454E-9
$\hat{\sigma}^2$	0.000409	0.000380	0.227	0.194	0.0559	0.0661	0.238	0.168	0.243	0.214	0.234	0.176
R^2	0.970	0.971	0.191	0.157	0.801	0.713	0.152	0.271	0.134	0.0720	0.164	0.238

PROBE 8501, VARIABLE Y, CHAN Y

	u_H Forward (N=20)	u_H Reverse (N=20)	$(Re)_s$ Forward	$(Re)_s$ Reverse	UT/A Forward	UT/A Reverse	A/d Forward	A/d Reverse	UT/d Forward	UT/d Reverse	$(Re)_o$ Forward	$(Re)_o$ Reverse
Mean Sensitivity			1.680	1.761	1.680	1.761	1.680	1.761	1.680	1.761	1.680	1.761
$\hat{\alpha}$	0.0387	0.0516	1.87	2.13	1.668	1.861	1.853	2.083	1.750	2.044	1.914	2.04
$VAR(\hat{\alpha})$	0.379E-3	0.415E-3	0.0116	0.00981	0.00886	0.0111	0.0214	0.0248	0.0112	0.991E-2	0.0126	0.0166
β	1.406	1.403	-0.340E-5	-0.667E-5	0.00104	-0.00867	-0.135	-0.251	-0.177E-2	-0.714E-2	-0.135E-4	-0.160E-4
$VAR(\hat{\beta})$	0.0119	0.0130	0.324E-11	0.273E-11	0.492E-4	0.618E-4	0.0118	0.0136	0.572E-5	0.506E-5	0.357E-10	0.472E-1
$\hat{\sigma}^2$	0.00110	0.00120	0.0388	0.0327	0.0465	0.0584	0.0429	0.0496	0.0452	0.0399	0.0363	0.0480
R^2	0.902	0.894	0.166	0.475	0.0012	0.0633	0.0794	0.204	0.0295	0.359	0.221	0.231

Unsteady effects on unsteady sensitivity for combined steady/oscillatory flows. Tests were run in the forward and reverse directions, and functional dependence for u_H, $(Re)_s$, UT/A, A/d, UT/d, and $(Re)_o$.

91

TABLE 13.

F-statistics for analysis of variance test of
null-hypothesis that the population correlation equals
zero (P = 0.95).

N $(p=2)$	F^{p-1}_{N-p}	R^2
10	5.32	0.400
12	4.96	0.332
14	4.75	0.284
18	4.60	0.223
20	4.41	0.197
21	4.38	0.187
22	4.35	0.177
23	4.32	0.171
24	4.30	0.163
27	4.24	0.145
29	4.21	0.135
30	4.20	0.130
35	4.12	0.111
40	4.08	0.0970
44	4.06	0.0881
46	4.05	0.0843
48	4.04	0.0807
50	4.04	0.0776
51	4.04	0.0762
52	4.03	0.0746
56	4.01	0.0691

Table 13. Confidence intervals for 95% levels derived from F-statistics for
analysis of variance test of null-hypothesis that the population correlation is zero.
Values calculated from tables in Abramowitz and Stegun, 1972.

For sensor B501, the mean steady sensitivity during oscillatory tests was 1.484, a reduction of 7.1% from the pure steady value of 1.589. The calculated $\hat{\beta}$ relating steady sensitivity to non-dimensional parameters is significant only for UT/d and $(Re)_s$, but not for A/d, $(Re)_o$, or UT/A.

Thus the combined motion has a demonstrable effect on steady response. It decreases the sensitivity of the sensor to steady components, by an average of 8.5% for the two instruments tested here. This reduction agrees with an expected decrease in sensitivity due to the complex wake structure set up by oscillatory motions. Steady sensitivity is a function only of the steady Reynolds number, $(Re)_s$, and not of (A/d), $(Re)_o$, UT/d or UT/A. This positive correlation between sensitivity and Reynolds number is consistent with the notion of boundary layer compression with increasing $(Re)_s$. Lack of consistent correlation of $\hat{\beta}$ with UT/A (a measure of steady speed to oscillatory speed) is contrary to results reported by McCullough (1978).

Error variance $(\hat{\sigma}^2)$ for S563 is increased in the combined steady/oscillatory tests compared to the pure steady results. In pure steady results, error variance $(\hat{\sigma}^2)$ is 0.00137 (volts)^2, while fits for (A/d), $(Re)_o$, UT/d and UT/A show an error variance of nearly three times this value (increasing the r.m.s. error by 70%). Fits to $(Re)_s$ show an increase in error variance of only 50%, for an increase in r.m.s. error of 22%.

For B501, the error variance $(\hat{\sigma}^2)$ for all fits is increased nearly the same amount over that for pure steady flow. Whereas pure steady error variance is 0.000715 (volts)^2, error variances increase over the range of 7 times (for $(Re)_o$ results) to only 5 times (for UT/d), with an average increase of 6.4 (translating to an increase in r.m.s. error of 250%!). The behavior of this larger sphere in combined steady/oscillatory flows was not as good as the smaller sphere (S563), as indicated by error variance estimates.

b) Effects of combined steady/oscillatory flow on oscillatory response: As discussed in the previous section two current meters were tested under combined steady/oscillatory flow. The x-axis of the small sphere (S563) and the y-axis of the large sphere (B501) form the basis for interpreting steady/oscillatory flow effects on unsteady (oscillatory) response.

For both sensors, the peak voltage was related to peak velocity (u_m) as in pure oscillatory flows. For S563y, the pure oscillatory sensitivity is 1.695, the pure steady value is 1.685, and the oscillatory sensitivity for combined steady/oscillatory flow is 1.55. The worst case combined steady/ oscillatory sensitivity differs from the pure oscillatory value by 9.1%, with oscillatory sensitivity decreasing in combined steady/oscillatory flows. Mean sensitivity for the forward and reverse runs as a function of the non-dimensional groupings is 1.883, an increase in sensitivity of 12% over the pure steady case. Part of this apparent increase is due to not including a numerical offset in the sensitivity calculations; the data reduction technique eliminates the electronic offset. This apparent difference in oscillatory response reinforces the need for including a numerical offset in data reduction procedures.

For S563, the unsteady sensitivity is significantly related to all non-dimensional groupings ($(Re)_s$, A/D, UT/d and $(Re)_o$) except for UT/A. This lack of correlation with UT/A is surprising, since it is the ratio of steady to oscillatory velocities, a ratio used by others to define sensor sensitivity to unsteady flows.

For sensor B501y, the sensitivity calculated from a regression of maximum orbital speed against maximum voltage is 1.40 for combined steady/oscillatory flow. This can be compared to a pure oscillatory sensitivity of 1.638 and a pure steady value of 1.589. The oscillatory sensitivity in combined steady/

oscillatory flow shows a reduction of 21% and 14% as compared to pure oscillatory and pure steady cases, respectively. The difference between the combined steady/oscillatory and pure oscillatory sensitivity is significantly different at the 95% level, while the difference with the pure steady value is significant at the 90% level.

Mean sensitivity for B501 calculated without using an offset has a value of 1.72 (averaged over forward and reverse tows). This is significantly higher than the sensitivity calculated for pure steady flows, but not those from pure oscillatory flows. As in the tests of S563, mean sensitivities were higher (greater sensitivity) than calculated using a numerical offset, because the offset in both S563 and B501 are positive. Oscillatory sensitivity for B501 is significantly correlated with $(Re)_s$, UT/d and $(Re)_o$, but not with UT/A or A/d.

In summary, combined steady/oscillatory motion has several effects on unsteady response. First, it reduces the response of the instrument in oscillatory flows by 10-20%, in accord with the idea of increased complexity of wake structure around the sphere. Second, oscillatory sensitivity is correlated with $(Re)_s$, $(Re)_o$ and UT/d (an inverse Strouhal parameter), but not with UT/A or A/d. Lack of consistent dependence on UT/A is puzzling, since this non-dimensional grouping, representing the ratio of steady to oscillatory velocity, has been successfully used in the past to define current meter behavior.

Category 4: HORIZONTAL COSINE RESPONSE

Two sensors were calibrated for horizontal cosine response: a large sphere (B498) and a small sphere (S563). Hardware for performing these calibrations is discussed under the methods section. Calibrations were performed at 5° increments (for S563) or 10° increments (for B498) from 0° to 360°, with each orientation towed at three different steady speeds.

95

Data analysis proceeded as for steady tow tests. Electronic offset was removed by referring voltage to the no-flow (not zero voltage) level. Errors due to this convention will be partly a reflection of the numerical offset, signaling a non-linear sensitivity. The experimental set-up enables us to accurately measure relative angle changes, with accuracies of a fraction of a degree using machined spacers (figure 11). Absolute direction referenced to the axis of the MIT tow carriage was difficult to establish to better than 2-3°. To circumvent this problem, we applied a post-calibration correction, minimizing the mean square error of the measured cosine response to predicted cosine response, as a function of angle. Solved in a least-square sense, the result was an optimal estimate of the absolute orientation of the current meter with respect to the tow cart axis. Because of the possible Re-dependence on cosine response, each axis was calibrated at three values of Re, and the positive axis (positive flow) was analyzed separately from the negative axis (negative flow).

The smaller, 4.0 cm diameter sphere (S563) was tested at Reynolds numbers of 6400, 20,200 and 38,700. Twelve combinations were tested: each axis in each sense of flow (positive and negative) at each of three Reynolds numbers. According to the least squares criterion mentioned above, the mean deviation of the absolute zero angle to estimated zero angle (sensor lined up along tow tank axis) was -1.9°. Root-mean-square deviation about the zero value was 3.9°. Standard deviation of the true sensor orientation about the mean orientation error was 3.6°, based on the small sample population (12 events).

For the small sphere, the average sensitivity (over all angles) for each of the axes and at each of three Re is shown in Table 14. Results for positive tow directions were indistinguishable from those for negative tow directions. Results indicate a mean sensitivity, which is dependent on Re, with sensitivity increasing with Re. Sensitivities are consistently lower than comparable values for on-axis steady tow results (table 7), by 3-12%.

96

TABLE 14

SENSOR S563 MEAN SENSITIVITY

HORIZONTAL COSINE RESPONSE
(Volts/m/sec)

	6,400	<u>Re</u> 20,200	38,700
X-Axis	1.501	1.560	1.632
Y-Axis	1.485	1.540	1.609

Table 14. Sensor S563 mean sensitivity in horizontal cosine tests, run
at three Reynold's numbers on both axes.

This lowered sensitivity suggests an inter-cardinal undersensitivity in horizontal cosine response, with greatest undersensitivity at low Re. Detailed examination of horizontal cosine response demonstrates this inter-cardinal undersensitivity, and its trend with Re. This examination also shows two further features. First, because of the non-linear response observed in these meters, response to off-axis flows near 90° shows large errors in normalized gains. Secondly, there is a shoulder-like structure in the cardinal sensitivity, particularly for lower Re experiments. Directly near 0° relative flow, sensitivity is low, then rises as relative angle increases to about 20°, finally turning to undersensitivity as angle increases further. This near-cardinal behavior is likely due to asymmetries in sensor geometry as the protruding electrode is slowly rotated away from the forward stagnation point.

Root-mean-square errors in horizontal cosine response (minimized according to the procedure outlined earlier in this section) varies as a function of axis and Re (table 15). Errors did not vary according to direction of tow (positive versus negative flows). Errors increase with tow speed (Re), for both axes, varying by a factor of two or three. In terms of velocity, these errors range from 0.01 to 0.03 m/sec, comparable in magnitude to those arising from steady tow results. Residual errors plotted as a function of tow angle relative to the stagnation point are larger as the sensor is rotated away from head-on tow directions, for all Re. This may be a partial reflection of the numerical offset resulting from non-linear sensitivity.

Tests for B498 show similar results. As in the previous case, twelve combinations were examined: each of two axes for two flow senses (positive and negative) for each of three Re. Tests on this sensor were for flow Re of 16,800, 53,000, and 101,500. Using the least-square error minimization procedure outlined earlier, the mean correction for current meter orientation

98

TABLE 15

SENSOR S563 RMS ERRORS

HORIZONTAL COSINE RESPONSE
(Volts)

	Re		
	6,400	20,200	38,700
X-Axis	0.016	0.038	0.047
Y-Axis	0.015	0.034	0.037

Table 15. Sensor S563 root-mean-square errors in horizontal cosine tests run, at three Reynold's numbers on both axes.

was −1.3°, with a standard deviation of 1.4°. Root−mean−square deviation about assumed zero orientation was 1.8°, showing our orientation procedures resulted in only a small mis−orientation.

For this larger sphere, the mean sensitivity varied as a function of Re (table 16), although not in as predictable a manner as the smaller sphere. Up to a Re of 53000, the mean sensitivity increased, but decreased slightly at a Re of 101,500. For the smaller sphere, sensitivity increased steadily up to a Re of 38,700. Mean sensitivity for all horizontal cosine tests were less than those for on−axis steady flow tests (table 7) by 8 to 29%, demonstrating the inter−cardinal undersensitivity observed in the smaller sensor. Greatest under−sensitivity occurs at low Re. Detailed examination of individual combinations illustrates this undersensitivity. These curves also show the large errors in normalized sensitivity for relative flow angles of 90°, mirroring the effect of non−linear response and numerical offset. For low Re, there is also evidence of the cosine "shoulder", responding to asymmetries in electrode position near the forward stagnation point.

Root−mean−square errors, minimized as discussed earlier, show definite relationships to Re (table 17). Errors steadily increase as Re increases, ranging from a low value of 0.011 volts to a high of 0.046 volts. Translated to velocity, these r.m.s. errors range from 0.01 m/sec up to 0.03 m/sec. Residues, calculated from measured voltages subtracted from those calculated from a true cosine response, are largest for off−axis flows, least for nearly head−on condi−tions. These results are consistent with those determined from the smaller sensor, S563.

Category 5: GRID TURBULENCE RESPONSE

To test the effect of free−stream turbulence on the response of EMCM's, two grids with different grid parameters (table 6) were towed in front of the 4.0 cm diameter EMCM sensor (S563). The experiment was neither complete nor

TABLE 16

SENSOR B498 MEAN SENSITIVITY

HORIZONTAL COSINE RESPONSE
(Volts/m/sec)

	$\underline{Re}$		
	16,800	53,000	101,500
X-Axis	1.313	1.479	1.470
Y-Axis	1.435	1.565	1.550

Table. 16.   Sensor B498 mean sensitivity in horizontal cosine tests, run at three Reynold's numbers on both axes.

TABLE 17

SENSOR B498 RMS ERRORS

HORIZONTAL COSINE RESPONSE
(Volts)

	Re		
	16,800	53,000	101,500
X-Axis	0.013	0.018	0.041
Y-Axis	0.011	0.018	0.046

Table 17. Sensor B498 root-mean-square errors in horizontal cosine tests, run at three Reynold's numbers on both axes.

exhaustive; it was designed only to investigate whether further study was desirable. Consequences of these results are presented in the Discussion section. Results from the turbulence study were subjected to Model 1 and Model 2 analysis, as described in the Methods section (table 18).

Model 1 parameters are $\hat{\alpha}$, $\hat{\beta}$, $\hat{\sigma}^2$. Results using each grid are compared to results from steady tow tests where no grids were used. Model 1 shows that the sensitivity for each of the grids was lower than in runs without the grid. Grid 1 sensitivity differed by 24%, while grid 2 differed by 45%. Error variance for Grid 1 was significantly higher than that for pure steady flow, while error variance for grid 2 was less than that for pure steady flow.

Model 2 results ($\hat{\beta}_1$, $\hat{\beta}_2$, $\hat{x}_c$, $\hat{\sigma}_T^2$) are somewhat more complicated. For the low Re segment, grid 1 sensitivity is not significantly different from the pure steady case (at the 95% confidence level), while the sensitivity for grid 2 is significantly different from the pure steady value. Sensitivity variances for low Re segments are higher for the grid results than pure steady case. For the high Re segment, both grid 1 and grid 2 sensitivities are significantly different from the pure steady results. Variance in sensitivity is also larger for grid results than for pure steady results. Error variances for the combined fit ($\hat{\sigma}_T^2$) are lower for the pure steady case than for the grid tests in model 2.

As discussed previously, no independent measure of the velocity field behind the grid was made (hot film, impellor, etc.). True relative velocity was determined from cart speed, raising the possibility that flow blockage by the grid may have occurred. Simple theory (appendix 1) shows that grid 1 results can be explained by flow blockage, despite lack of obvious visual signs of blockage during test runs. However, grid 2 results cannot be explained by our simple theory of flow blockage. Although our theory may be in error, the higher turbulent intensities present in grid 2 tows may cause the change in

103

TABLE 18

S563: Grid-generated turbulence

	X-AXIS				Y-AXIS
	No Grid	Grid 1 Reverse	Grid 2 Forward	Both Grids	No Grid
	$N=52$	$N=27$	$N=24$	$N=51$	$N=52$
α	-0.0727	0.00196	-0.0605	-0.0666	-0.0686
$\text{Var}(\hat{\alpha})$	0.000109	0.000684	0.00115	0.00300	0.000102
$\hat{\beta}$	1.685	1.273	0.931	1.173	1.663
$\text{Var}(\hat{\beta})$	0.000138	0.000813	0.00174	0.00340	0.000130
$\hat{\sigma}^2$	0.00137	0.00443	0.00115	0.0364	0.00129
R^2	0.998	0.998	0.958	0.877	0.997
$\hat{\beta}_1-2\hat{\gamma}_1$	1.498	1.427	0.767		1.540
$\hat{\beta}_1$	1.524	1.480	0.883		1.556
$\hat{\beta}_1+2\hat{\gamma}_1$	1.551	1.534	1.000		1.573
$\text{Var}(\hat{\beta}_1)$	0.000176	0.0007603	0.00341		0.0000707
$\hat{\beta}_2-2\hat{\gamma}_2$	1.719	0.969	1.169		1.640
$\hat{\beta}_2$	1.760	1.109	1.346		1.697
$\hat{\beta}_2+2\hat{\gamma}_2$	1.801	1.248	1.522		1.753
$\text{Var}(\hat{\beta}_2)$	0.000426	0.00489	0.00779		0.000798
$\hat{X}_c$ $(\text{Re})_c$	0.8	0.9	0.9		1.0
$\hat{\sigma}_T^2$	0.000490	0.00177	0.00257		0.000349

Table 18. Grid-generated turbulence effects on steady sensitivity, for two experimental grids. 'No grid' values taken from tables 7 and 8. $\hat{\gamma}_1$ and $\hat{\gamma}_2$ are the 95% confidence extremes derived from an F-test statistic.

sensitivity. Without _in situ_ measurements of turbulent intensities, it is difficult to assess how characteristic grid 2 turbulence intensities are of field conditions, although surf zone turbulence intensities can be 20% or higher. These experiments suggest that further experimentation on the effects of free-stream turbulence on current meter sensitivity is required before we place too much confidence either in these present test results, or in EMCM data from highly turbulent surf zones.

DISCUSSION

Experiments on the dynamic response of electromagnetic current meters demonstrate a complex behavior in steady and oscillatory flows which must be considered in interpretation of these data. Tests were conducted in a carefully controlled laboratory environment, under repeatable conditions. While not reproducing field conditions, one would expect field behavior of the sensors to be no better than, and probably inferior to, laboratory conditions. Results from this study suggest areas for future research to elucidate specific sensor response, which the present study was not adequately equipped to study (e.g., high Re flow simulation, complete grid turbulence studies, very large A/d behavior, etc.). Flow sensor errors observed in this experimental study should encourage investigators to properly and thoroughly evaluate instrumental errors (for any flow sensor). Considering the errors found in this study, EMCM sensors are useful for a variety of environmental applications. For other more rigorous applications, these sensors may not be suitable. To determine the sensor's utility for any application, a careful error analysis is required, using the present results to estimate statistical variability.

This discussion section summarizes the major findings of this study, emphasizing characteristic sensor response to varying flow fields. We discuss the physical behavior of flow around a spherical sensor, and why this shape is not an optimal choice for near-planar flow fields. We present alternatives for processing emcm data to account for the various dynamical tendencies of these flow sensors. Finally we briefly apply these results to a few examples of dynamical interest, estimating errors in dynamical terms based on kinematic errors observed in the laboratory.

Because of the complicated flow around a sphere, one would expect its use as an EMCM would have limitations. Not only is the boundary layer structure a function of flow Re, but wake structure around blunt bodies is also complex. Add to this large roughness elements, nonuniformly distributed about the sphere, and the wake structure becomes even more complicated. As discussed in detail earlier, this complicated flow structure under steady conditions leads one to expect nonlinearities in sensitivity, even for protruding electrodes, since wake structure is as important as boundary layer thickness. In fact, sensitivity of these sensors is nonlinear, demonstrated by the presence of a numerical offset (differentiated from an electronic offset) and the better two-segment linear-fit model (Model 2) as compared to the single segment best-fit model (Model 1). The cutoff in the Model 2 results was not linked to any boundary layer phenomenon, such as transition point between laminar and turbulent flow. This is partly attributed to the influence of protruding electrodes and mounting gear, which cause a transition at a lower Re (3×10^4 to 1×10^5) than predicted from experiments on smooth spheres (Re=3×10^5). The scatter in these transition values and significant difference in critical Re for large versus small spheres, however, argue against the interpretation

of $\hat{x}_c$ as the transition Reynolds number. In fact, $\hat{x}_c$ may be soley a statistical result, not a dynamical one. The better fit obtained using multi-segment or polynomial models can be useful for calibration and analysis purposes, even if it is not linked to any clearly defined dynamical effect.

Although single-segment linear models relating voltage output to tow speed show significant fits, mean errors are on the order of one to five cm/sec. Differences in sensitivity of 10% between axes and departures from manufacturer calibrations emphasize the necessity of careful, frequent calibrations for sensitive experiments.

The nonuniform distribution of roughness elements and complicated flow structure lead to a Re-dependent horizontal cosine response. Undersensitivity as high as 25% leads to rms errors in velocity (for a particular Re) of one-to-three cm/sec. Largest residues or errors occur when flow is 90° away from head-on. This characteristic is due largely to wake structure and position of electrodes within or outside the wake. Furthermore, response is sensitive to small changes in flow direction near the cardinal axis, as an electrode rotates from its position at the forward stagnation point. This Re-dependent behavior gives rise to a calibration "shoulder" in the horizontal cosine response.

Steady flow sensitivity may also be affected by free-stream turbulence intensity and scales. Although experiments in this study are not conclusive, they suggest differences in steady sensitivity of up to 45% when free-stream turbulence intensities exceed about 1%, and energetic turbulent scales are the order of the roughness (electrode) size. Implications of this result for inner shelf and surf zone measurements are profound, since turbulence scales and intensities vary widely over short separations. This possibility reinforces

the need for careful, controlled follow-up studies to examine this behavior in detail. Previous studies of this effect (Bivins, 1975; Bivins and Appell, 1976; and Griffiths, 1979) have suffered from non-homogeneous turbulent field and limited range of turbulence scales and intensities. If sensor performance is as dependent on turbulent properties as suggested here, then the spherical EMCM's have limited utility in surf zone studies (where turbulence intensities commonly exceed 20%) unless the sensor dependence on turbulent properties can be predicted empirically or theoretically.

Steady flow around a sphere is distorted by roughness elements, whether they be electrodes, mounting brackets, or biological growth. In addition, the untreated metallic surfaces on the emcm sensor head (the mounting brackets and electrode faces) are prone to biological growth. Tests show a 26% decrease in sensitivity following a two-month deployment. Once the sensor was lightly scrubbed to remove biological growth, sensitivity returned to its pre-deployment level. This suggests that the gain variation was either hydrodynamic or electronic (through electrode differences). Since gain was more altered at large Re than small Re, most of the fouling effect was hydrodynamic.

Flow around spheres becomes more complex when oscillatory motions are introduced, especially when orbital amplitudes are only slightly larger than, or smaller than, the sphere diameter. As flow reverses, the boundary layer must redevelop, the wake structure must stabilize, and pressure gradients readjust. Time scales for these processes can be of the order of the orbital period, causing a chaotic, unsteady flow structure. For particular periods, forces are exerted on the sphere which can cause sphere movement if the sphere is not rigidly attached.

Our experiments showed no significant differences between pure oscillatory and pure steady sensitivities. Oscillatory sensitivity is significantly correlated with A/d and $(Re)_o$, but not Tv/d^2, suggesting laminar boundary layer thickness is not important in EM sensor behavior. Sensitivity generally decreases with increasing A/d and increasing $(Re)_o$, which behavior has no obvious physical explanation. Finally, oscillatory behavior showed the importance of including the numerical offset in sensitivity calculations, since neglect of this offset resulted in an average 8% change in apparent oscillatory sensitivity (increased sensitivity since offsets were all positive).

Flow structure around spheres is increasingly complicated under combined steady and oscillatory flows. Intuitively one can see the effect if $u_m > U$, since flow would actually reverse over an oscillation, similar to pure oscillatory conditions. However, even for $u_m < U$, unsteady effects will alter significantly the measurement of steady flow components, changing local pressure distributions around the sphere. Since inner shelf and surf-zone environments are generally characterized by combined wave/current flows, our tests were particularly relevant.

Steady flow was combined with horizontal oscillatory flow, both for colinear and perpendicular conditions. Under these combined conditions, steady sensitivity decreased by 7–10%, with a dependence on the nondimensional grouping of $(Re)_s$, but not consistently with A/d, $(Re)_o$, UT/d or UT/A. Sensitivity increased with $(Re)_s$. Error variance increased in these combined flows as well, increasing by up to 70%, and sometimes more.

As with the steady case, oscillatory sensitivity decreased under combined flow conditions over the range of 9–21%. This decrease in sensitivity is consistent with the notion of complicated wake behavior. Oscillatory sensitivity is significantly correlated with $(Re)_s$, UT/d and $(Re)_o$, with less correlation with A/d and none with UT/A. Lack of dependence on UT/A was not expected.

Combined steady/oscillatory flows are shown to alter response of spherical EMCM's, attributable in large part to changes in wake structure under this complex flow situation. Although induced currents, or streaming, were not directly observed in this study, changes in numerical offsets and variable sensitivities combine to produce an apparent steady flow. Numerical offsets of up to 4 cm/sec were calculated, which would result in an apparent steady flow if not properly accounted for. These apparent flows never exceeded 10 cm/sec.

The complicated response of EMCM's to varying hydrodynamical conditions makes analysis of EMCM data difficult. Several options are available. The most commonly used option is to ignore these dynamical effects, and apply either the manufacturer's calibrations or steady flow calibrations. This study clearly shows that such an option is foolish unless an error analysis indicates that the required accuracies are much less than the errors in response. The second option is to use results from this study to calculate errors associated with any particular use of the data, and judge if those errors are acceptable. If accuracy is still sufficient for a given use, then the data can be used for that application with appropriate errors. If accuracy is not good enough, then either a more precise calibration is required (such as a multi-segment or polynomial model fit, or even a more complete dynamical gain description), or another instrument must be selected.

The third option is to provide a complete dynamical description of current meter response to ambient flows, and correct the data according to this response. This approach requires either a complete understanding of dynamical behavior of spherical sensors, or extensive and exhaustive testing of each current meter used. For instance, if deviation from the horizontal cosine is

known (as it is here), we can model that response with an analytic representation and correct our results in an iterative fashion (e.g., Smith, 1978). For example, if our calibration is inverted to express velocity (U) as a function of voltage (v), we obtain:

$$U = \alpha' + \beta'v$$

where:
$$\alpha' = -\alpha/\beta$$
$$\beta' = +1/\beta$$

and α, β are offset and sensitivity calculated from our Model 1. We can put in a correction factor to account for horizontal non-cosine response:

$$U = (\alpha' + \beta'v) G(\theta)$$

where $G(\theta)$ is a normalized gain function describing deviations from cosine behavior. This equation is solved iteratively, resulting in an increased complexity in data analysis with hopes of rapid convergence. Similar corrections can be made for vertical cosine response, $G(\phi)$, and combined vertical and horizontal directional response, $G(\theta,\phi)$, to substantially increase accuracy.

Similar corrections can be made for frequency response (e.g., Nielsen and Cowell, 1981). If the frequency response of an instrument is tested, then corrections for non-constant transfer function can be made. Generally users of EMCM's specify a time constant for a particular application, depending on the frequency band of interest. These time constants arise from analog electrical filter characteristics of the particular instrument. It is erroneously assumed that the frequency response for an instrument guarantees a constant transfer function, $L(f)$, and an ability to resolve scales that are contributing to high frequency components. In fact, spatial averaging prevents resolution of many of these higher frequency components, in a manner often approximated using Taylor's frozen turbulence hypothesis. Given the averaging volume of an EM sensor

111

(approximately 2-3 sphere diameters in scale), one can compute the frequency cut-off for energetic turbulent flows in any steady current U. Secondly, the filter cut-off is often the -3 db point of the filter, when the transfer function has decreased to a level of 50% the unfiltered value. This is of little concern if energetic motions are confined to frequencies well below the cut-off frequency, but can lead to aliasing and erroneous spectral estimates when frequency of energetic motions is close to or higher than the cut-off frequency. Corrections for the frequency response can be made easily in the frequency domain, by inverting the transfer function. Corrections can also be done in the time domain by deconvolution, generally an expensive procedure. A safe strategy to avoid these problems is to assure that the cut-off frequency is well above any energetic motions which would be sensed by the current meter.

In a manner similar to the two examples presented above, an analysis package could account for hydrodynamical gain variability relying on dimensional analysis and empirical test results. For instance, a calibration equation could take the form:

$$U = (\alpha' + \beta'v) \, G(\theta, \, Ud/\nu, \, Ad/T\nu, \, A/d)$$

where θ is the angle of the sensor relative to direction of steady flow. Empirical results are then used to relate the gain, β', to each of the dimensionless groupings, using linear prediction techniques. Alternatively, corrections could be made in the frequency domain, where the correction factor would have to be inter-related as in the above formulation.

The problems with this approach are manifold. First, the present study shows few relations which are sensor independent. Lack of a general relationship between gain and all non-dimensional parameters forces the necessity of complete calibration of each meter, a time-consuming and expensive process. Such corrections are also computationally expensive, increasing data analysis costs. Clearly, use of this approach requires good justification that the

results are worth the effort. Where such a justification is provided, a less expensive solution might be to use an alternate sensor or measurement technique. Furthermore, if the behavior of the gain function G is related complexly to turbulent scales and intensity, the above exercise is futile.

Other processing alternatives exist. For instance, depending on the ratio UT/A (steady Re divided by oscillatory Re), one could assign a gain for the steady component which is of neutral sensitivity (no oscillatory flow) or undersensitive (comparable oscillatory flow). Similarly, for the oscillatory component, a variable gain could be applied depending on this same ratio. Such gain corrections would best be applied as spectral corrections: once the spectrum is calculated, mean flows are corrected for undersensitivity and non-cosine response, while oscillatory gains are corrected and distinguished from steady gains. This must proceed on a meter-by-meter, axis-by-axis basis, of course.

To illustrate the impact of these hydrodynamically-dependent flowmeter responses on various applications of these data, we consider briefly four cases: a) estimation of velocity for kinematic purposes; b) use of arrays of EMCM's for log-law estimates of u_*; c) use of EMCM's for directional wave estimation; and d) estimation of higher order velocity moments for sediment transport purposes.

a) Estimation of velocity for kinematic purposes – For measurement of pure steady or pure oscillatory flows, the EMCM is accurate. Standard errors for these calibrations are small, with standard deviations of one to five cm/sec. Errors can be reduced significantly by higher-order fits, using either multiple-segment linear regression or higher-order polynomial regression. Using different gains for each axis, careful calibrations should yield r.m.s. errors of less than 1-2 cm/sec, for limited Re ranges. Care must be taken to

minimize effects of biofouling on degradation of gain. Deviations from cosine response can be easily accounted for in numerical analysis procedures, either in real time or following the experiment. These accuracies, however, all depend on obtaining good electronic zeroes or offsets in the field.

Combined steady/oscillatory flow considerably degrades sensor response, and steady gains commonly may have errors of 10% or so. Similar results exist for oscillatory gains. Some improvement in gain uncertainty can result from careful calibrations. Errors are larger than for pure steady or pure oscillatory flows by a factor of two or more. Magnitude of errors also depends on the impact of free-stream turbulence on sensor performance. The present study suggests sensitivity depends on turbulent intensity and scale. Since the present experiments were neither complete nor exhaustive, this effect is only a possible source of degradation in sensor performance, which must be examined more fully.

b) Use of arrays of EMCM's for log-law estimates of u_* - For suitably behaved boundary layers, there is a constant stress region whose turbulence level can be calculated a variety of ways: logarithmic-law, eddy correlation, and inertial range dissipation estimates. Examining the logarithmic law only, we need to consider the appropriate statistics for obtaining significant estimates of u_*. The friction velocity, u_*, is obtained from a least-square fit of mean velocities at a number of vertical positions above the bottom. We can use the F-test to establish a null hypothesis limits for our estimates of u_*, by calculating the probability that u_* is different from $2u_*$ or 0 at the 95% confidence level. To do this, we evaluate:

$$F_{N-p}^{p-1} = \frac{R^2 (N-p)}{(1-R^2)(p-1)}$$

where p is 2, and N is the number of current sensors in the vertical array

used to test the fit. For $N = 3$, we need an R^2 value of 0.994 before the null-hypothesis is invalidated. For $N = 4$, we need an R^2 of 0.902 before the null-hypothesis is invalidated. For the case of $N = 2$, R^2 cannot be tested because there will always be a perfect fit between two points. Tests for 95% confidence limits on any multiple of u_* can be made using the t-test, if $VAR(u_*)$ is known or calculated.

Numerical experiments for the EM sensors tested here show that this fit is possible for pure steady flows with low free-stream turbulence levels if the EMCM's are carefully calibrated. For sensors which are exposed to high-intensity free-stream turbulence or for sensors with significant unsteady, oscillatory components, these criteria may be rarely met. For gain uncertainties of 10% or more, and unstable electrical or numerical offsets, these criteria preclude the use of EMCM's for precise (95% confidence limits) estimates of u_*.

For similar reasons, and adding on the other error sources associated with determining an appropriate vertical reference direction, eddy correlation techniques are difficult to apply to field data acquired with EMCM's if strong oscillatory motion is present or possibly if free-stream turbulence levels exceed a low threshold.

c) Use of EMCM's for directional wave information - Aubrey (1981) and Grosskopf et al. (1983) discuss the use of EMCM's for directional wave estimation, when deployed in conjunction with a pressure sensor. The current meter data can be used to determine the frequency spectrum of the sea surface elevation, as well as the directional properties of waves. For use as indicators of sea surface variance, the unsteady gain of the instrument must be well known. Aubrey (1981) and Aubrey and Goud (1983), show sea surface variances calculated using pressure data and velocity data agree well (within

10%), suggesting that for these conditions the steady gain applied is close to the true oscillatory gain. As long as the ratio of the gains from the two axes is constant, the directional information will be affected only slightly. Mean direction will be unchanged, but the directional distribution will be altered. Comparison of sea surface variance for pressure and velocity data provides a useful check on current meter performance and extent of fouling.

Because directional estimates rely on ratios of products of pressure and velocity auto- and cross-spectra, gains for each of these functions must be known to at least a common multiple. For instance, separate gains for x- and y-axis are required to obtain good directional information. The 5–10% difference in gain between sensor axes observed in this study uniformly degrades directional estimates. Preferably, gains derived from combined steady/oscillatory calibrations should be applied, rather than those from pure steady, although this is difficult and expensive to do routinely. Accurate offsets are also crucial to good directional estimates, as an incorrect offset will bias the estimate.

If free-stream turbulence levels are critical to EMCM calibration, flow sensors should be removed from the more energetic part of the turbulent bottom boundary layer. Finally, directional estimates can be seriously degraded by biofouling, as indicated by the present experiments on a "dirty" probe following a two-month deployment, compared to that same probe before deployement. Gain degradation was different for the x- and y-axes, indicating that any directional information derived from such a sensor would be in error after biofouling began. Biofouling apparently does not always degrade directional estimates, as reported in Grosskopf et al. (1983).

d) Estimation of higher order velocity moments for sediment transport purposes – A common use of current meter data is estimation of sediment transport rates using a higher-order moment of the velocity signal. For

116

instance, the velocity skewness, $\langle u^3 \rangle$, is commonly taken to be proportional to sediment transport rate. If we know the errors in estimating u, we can make estimates of errors in $\langle u^3 \rangle$.

As a simple model, we assume that:

$$u = u' + \epsilon$$

where u is the true velocity, u' is the observed velocity, and ϵ is the error in the observation. We can then calculate $\langle u^2 \rangle$:

$$u^2 = u \cdot u = u'^2 + 2u'\epsilon + \epsilon^2$$

and then $\langle u^3 \rangle$:

$$u^3 = u'^3 + 3\epsilon u'^2 + 3\epsilon^2 u' + \epsilon^3$$

In this latter case, our relative error is approximately $3\epsilon(u')^2/(u')^3 \approx 3\epsilon/u'$ whereas the relative error in u is ϵ/u'. Our relative error in $\langle u^3 \rangle$ therefore is 3 times that in u. For a ratio $\epsilon/u' = 0.1$ (a 10% error in gain), relative error in $\langle u^3 \rangle$ is about 0.331, an unacceptable error in many situations. For an error ratio $\epsilon/u' = 0.45$ (characteristic of the error observed in a dirty probe calibration and in a free-stream turbulence calibration), the relative error in $\langle u^3 \rangle$ is greater than 2.05, for a signal-to-noise ratio of less than one-half.

This error analysis is not sophisticated enough to represent all errors in estimation of higher order velocity moments, but it is indicative of the magnitude of the problem of estimating dynamical quantities from imperfect kinematical observations. A more complete analysis must properly account for the many sources of error present in em measurement systems, both electronic and hydrodynamic. An improved analysis we have been developing, represents the velocity as follows:

$$u = \left[(\alpha' + \epsilon_\alpha) + (\beta + \epsilon_\beta)v + \epsilon\right]\left[G(\overline{X}_i) + \epsilon_G\right]$$

where the subscripts refer to the source of the error terms, and the $\overline{X}_i$ are dependent on various nondimensional groupings of hydrodynamic origin. This

117

model forces consideration of joint error probabilities, not only for the calibration constants but also for the functional gain operator G. Using data acquired in this study, for simple forms of $G(\theta)$ where a deviation from horizontal cosine response is the only contributor to the gain function, we have calculated errors in u, u^2, and u^3. These numerical exercises show signal-to-noise ratios for $\langle u^3 \rangle$ typically of order 0.5 to 1.0 for combined steady/oscillatory flows. This modeling is proceeding with an attempt to better define the appropriate error sources due to hydrodynamic terms.

SUMMARY

The dynamic response of electromagnetic current meters (manufactured by Marsh-McBirney, Inc.) has been clarified through a comprehensive laboratory measurement program combined with a thorough literature review. Elucidation of the behavior of these flowmeters under a variety of dynamic conditions has been neglected in the past. Since flow past a spherical body has considerable hydrodynamic complexity for different dynamic conditions, a careful laboratory study was carried out for pure steady, pure oscillatory (horizontal plane), and combined steady/oscillatory conditions at two test facilities. Test results indicate that flowmeter behavior under pure steady flow is excellent in the absence of high levels of free-stream turbulence, with an r.m.s. error of 1-5 cm/sec. These errors could be reduced with a higher-order polynomial regression fit. Pure oscillatory response was also excellent, with r.m.s. errors of 1-2 cm/sec, and sensitivity which is correlated with the oscillatory Reynolds number, $(Re)_o$, and the Keulegan-Carpenter number, (A/d). Combined steady/oscillatory flows degraded current meter performance with larger residual errors (1-6 cm/sec) and significant differences in sensitivity (up to 20%). Horizontal cosine response showed systematic deviations from pure

cosine behavior, with a notable inter-cardinal undersensitivity and cosine "shoulder" at lower Reynolds numbers. Error analysis shows these current sensors are adequate for many kinematic measurements, but may lead to excessive errors when using velocity to calculate dynamical quantities (such as bottom friction, Reynolds Stress, or log-layer friction velocities). A careful error analysis must precede any use of these meters for estimating dynamical quantities. These studies pointed out a potential difficulty in using these meters in areas of large ambient turbulence levels (20% turbulent intensities), which are characteristic of many near-bottom shallow water environments. Further study is needed to clarify this behavior.

RECOMMENDATIONS

Recommendations emanating from this study can be divided into two different categories. First, based on results in this study, recommendations are made for field use of these electromagnetic current sensors, and subsequent data analysis. Second, recommendations for future research on the response of these sensors, and for research into the development of alternative sensors for inner shelf and surf zone research, are enumerated.

Recommendations for use of EMCM's:

1) Pre- and post-calibrations of sensors are essential for many research-quality data requirements. Complete steady calibration tests are essential, spanning the Reynolds number range to be expected in the field. If pre- and post-calibrations differ substantially, then field results must be used with appropriate caution.

2) Limit deployments to one or two months maximum between calibrations, visiting the field site frequently to prevent biological fouling of the sensor and adjacent hardware. Gentle scrubbing of insulating, electrode, and sensor supports should minimize biological growth which might affect both the flow

characteristics surrounding the sensor, and the sensitivity of the sensor to that flow. Although this frequent calibration might not be convenient, it is essential for high quality research data and must be considered as part of the cost for acquiring such high quality data.

3) Prior to installation of a current sensor, gently scrub the electrode tips and the sensor head with a mild detergent as described by Marsh-McBirney in their literature. This will help assure complete surface wetting to more realistically mimic laboratory calibration factors. This scrubbing should be done before every laboratory calibration as well.

4) Allow immersion of the sensor in the water for at least one-half hour before acquiring data, either in the laboratory or in the field.

5) Perform zero-level tests (offsets) of all instruments in the field and laboratory, preferable at frequent intervals. This will allow correction for any zero-offset drift (which was not observed in our tests during limited deployment intervals), and immediately raise an alarm if large offset shifts occur. This zero-offset should be measured in the field, with a device which impedes flow past the sensor, and large enough to encompass the averaging volume of the sphere. The zero offset is particularly important for directional wave estimation since this offset error is directly tied to wave direction accuracy.

6) Protect the sensor head from grease or abrasion while it is out of the water. Impact and surface films can affect the sensitivity of the instrument.

7) Install the em sensors at least three diameters from the bottom, or any other material with a significantly different electrical conductivity.

8) Minimize flow disturbances due to instrument frames, mounting brackets, etc.

9) In data reduction, include corrections for horizontal angular response if such response is distinctly non-sinusoidal. Such corrections can be made in an iterative fashion, but are expensive since the response correction is a function of Reynolds number.

10) Develop a software methodology to test all hydrodynamic models for which EMCM's are used with sophisticated error analysis to see how errors propagate into the results. This error analysis will enable the user to determine necessary accuracies for current measurement for future experiments. Then and only then can the performance of any given current meter be assessed in light of the requirement of accuracy.

11) When implementing a calibration on the computer, be sure the instrument has been calibrated with the entire data acquisition system to account for voltage losses, roundoff, etc. in the data acquisition system.

12) For deployments where vector quantities are required, orient as precisely as possible, and re-orient periodically to check for changes in orientation over the deployment period.

Recommendations for future research:

1) Complete a well-designed investigation of the effects of free-stream turbulence scale and intensity on current meter response. This investigation should have two primary thrusts: first to evaluate the effects of free-stream turbulence on current meter sensitivity; second, to evaluate the averaging and aliasing characteristics of em sensors.

2) Investigate the response of em sensors to broad-band forcing, using carefully designed laboratory conditions.

3) Evaluate the utility of prolate spheroids (e.g., Greer, 1980) as geometries for em sensors, primarily for near-bottom flows under near-horizontal conditions, where their poor vertical cosine response will not come into play.

These would have to be fully tested similar to that undergone by spherical sensors, but have inate advantages due to their improved boundary layer characteristics compared to the normal spheroid.

4) Consider alternative sensors for inner shelf and surf-zone current measurement. Alternatives would include Helmholtz-coil sensors, which have been used with some success before (e.g., Olson, 1972). Acoustic doppler and travel-time sensors may also be useful, with lower errors than encountered with EMCM's. Although bubbles maybe a problem with acoustic sensors, this aspect has not been adequately documented in the field or laboratory. Encourage manufacturers of acoustic sensors to configure their products in a manner to minimize mounting distortions and make the instruments more versatile for surf-zone use.

ACKNOWLEDGEMENTS

REFERENCES

Abramowitz, M. and I.A. Stegun. 1972. <u>Handbook of mathematical functions</u>. Dover, NY, 1046 pp.

Achenbach, E., 1968. Distribution of local pressure and skin friction around a circular cylinder in cross-flow up to Re = 5 x 10^6. J. Fluid Mech., v. 34, p. 625-639.

Achenbach, E., 1971. Influence of surface roughness on the cross-flow around a circular cylinder. J. Fluid Mech., v. 46, p. 321-335.

Achenbach, E., 1972. Experiments on the flow past spheres at very high Reynolds numbers. J. Fluid Mech., v. 54, p. 565-575.

Achenbach, E., 1974. The effects of surface roughness and tunnel blockage on the flow past spheres. J. Fluid Mech., v. 65, p. 113-125.

Achenbach, E., 1974. Vortex shedding from spheres. J. Fluid Mech., v. 62, p. 209-221.

Appell, G.F., 1977. Current meter performance in a near surface simulated environment. Exposure, v. 5, no. 2, p. 5-9.

Appell, G.F., 1977. Performance of advanced ocean current sensors. IEEE Oceans '77, October 17-19.

Aubrey, D.G., 1981. Field evaluation of Sea Data directional wave gage (Model 635-9). Woods Hole Oceanographic Institution Technical Report, WHOI-81-28, 52 pp.

Aubrey, D.G., 1983. Surf zone measurements: precision and accuracy. In Proc. of a Conference of Coastal Current Measurement, C.E.R.C.

Aubrey, D.G. and M.G. Goud, 1983. Coastal Sediment Transport, Popponesset Beach, MA. Woods Hole Oceanographic Institution Technical Report No. WHOI -83-26, 132 pp.

Bailey, A.B., 1974. Sphere drag coefficient for subsonic speeds in continuum and free-molecule flows. J. Fluid Mech., v. 65, p. 401-410.

Bevir, M.K., 1970. The theory of induced voltage electromagnetic flow meters. Jour. Fluid Mech., v. 43, p. 577-590.

Bivins, L.E., 1975. Turbulence effects on current measurement. MS thesis, Univ. of Miami, Coral Gables, FL, 104 pp.

Bivins, L.E. and G.F. Appell, 1976. Turbulence effects on current measuring transducers. Exposure, v. 3, no. 6.

Bradshaw, P., 1974. Aero Rept. 74-10, Imperial College, London.

Clifford, A.A., 1973. Multivariate error analysis. Applied Science Publishers, LTD., London, 112 pp.

Comte-Bellot, G. and S. Corrsin, 1966. The use of a contraction to improve the isotropy of grid-generated turbulence. J. Fluid Mech., v. 25, p. 657-682.

Cooley, W.W. and P.R. Lohnes, 1971. Multivariate data analysis. John Wiley and Sons, Inc., New York, 364 pp.

Corrsin, S., 1963. Turbulence: Experimental methods. In Encyclopedia of Physics, S. Flugge (ed.), vol. VIII, Fluid Dynamics II, Springer-Verlag, p. 524-590.

Cunningham, P.M., R.T. Guza and R.L. Lowe, 1979. Dynamic calibration of electromagnetic flow meters. Proceedings of Oceans '79, IEEE and MTS, p. 298-301.

Cushing, V., 1961. Induction flowmeter. Rev. Sci. Instr., v. 29, p. 692.

Cushing, V., 1965. Electromagnetic flowmeter. Rev. Sci. Instr., v. 36, p. 1142-1148.

Cushing, V., 1974. Water current measurement. Geoscience, Wolff and Mercanti (eds.), Chapter 4, John Wiley and Sons, NY.

Cushing, V., 1976. Electromagnetic water current meter. Proceedings of Oceans '76, IEEE and MTS, p. 25C-1 to 25C-17.

Dibble, T.L. and C.K. Sollitt, 1981. Frequency response characterization of current meters. IEEE Oceans '81, p. 250-256.

Draper, N.R. and H. Smith, 1966. Applied regression analysis. John Wiley and
   Sons, Inc., 407 pp.

Fernholz, H.-H., 1978. External flows. In P. Bradshaw (ed.), Turbulence,
   Springer-Verlag, NY, 339 pp.

Gibbings, J.C., 1959. Aeron. Res. Council of London, Paper 462.

Greer, M.N., 1980. Development and application of a field instrumentation
   system for the investigation of surf zone hydrodynamics. Woods Hole
   Oceanographic Institution Technical Report, WHOI-80-36, 159 pp.

Griffiths, G., 1979. The effect of turbulence on the calibration of
   electromagnetic current sensors and an approximation of their spatial
   response. Institute of Oceanographic Sciences Report No. 68, Wormley,
   14 pp. + figures.

Gross, T.F. and A.R.M. Nowell, 1983. Mean flow and turbulence scaling in a
   tidal boundary layer. Cont. Shelf Res., v. 2, p. 109-126.

Grosskopf, W.G., D.G. Aubrey, M.G. Mattie and M. Mathiesen, 1983. Field
   intercomparison of nearshore directional wave sensors. IEEE, Journal of
   Oceanographic Engineering.

Guelke, R., 1944. The measurement of water velocities by means of
   electromagnetic induction. Admiralty Research Laboratory.

Guelke, R.W. and C.A. Schoute-Vanneck, 1947. The measurement of sea water
   velocities by electromagnetic induction. Jour. Inst. Elect. Engrs.,
   v. 94, p. 71-74.

Güven, D., C. Farell and V.C. Patel, 1980. Surface-roughness effects on the
   mean flow past circular cylinders. J. Fluid Mech., v. 98, p. 673-701.

Heathershaw, A.D., 1976. Measurements of turbulence in the Irish Sea Benthic
   Boundary Layer. In The Benthic Boundary Layer, pp. 11-31, I.N. McCave
   (ed.), Plenum Publ. Co., NY.

Hinze, J.O., 1959. Turbulence. McGraw-Hill, NY, 586 pp.

Jenkins, S.A., 1980. Viscous flow near a sphere under surface gravity waves. Ph.D. Dissertation. Univ. of Calif., San Diego, CA, 158 pp.

Jones, I.S.F., 1980. Electromagnetic current meters. In Dobson, Hasse and Davis (eds.), Air-Sea Interaction, Plenum Publishing Corp., NY, p. 219-229.

Kalvaitas, A.N., 1977. Current sensor dynamic testing. Polymode News, no. 28 (unpublished manuscript).

Landau, L.D. and E.M. Lifschitz, 1959. Fluid Mechanics, Addison-Wesley Publishing Co., Inc., Reading, MA, 536 pp.

Lavelle, J.W., R.A. Young, D.J.P. Swift and T.L. Clarke, 1978. Near bottom sediment concentration and fluid velocity measurements on the inner continental shelf, New York. Jour. Geophys. Res., v. 83, p. 6052-6062.

Laws, E.M. and J.L. Livesey, 1978. Flow through screens. Ann. Rev. of Fluid Mech., v. 10, p. 247-266.

Longuet-Higgins, M.S., and N. Barber, 1946. The measurement of water velocity by electromagnetic induction: An electrode flow meter. Admiralty Research Laboratory Report ARL/102.22/R 1/W, Teddington, Middlesex, England, 31 pp.

McBirney, T.R., 1975. Azimuth and tilt response of a spherical elecromagnetic water velocity sensor. Technical note 2, Marsh-McBirney Inc., Rockville, MD, 7 pp.

McCullough, J.R., 1974. In search of moored current sensors. Marine Technology Society, 10th Annual Conference, Washington, D.C., p. 31-54.

McCullough, J.R., 1978. Near-surface ocean current sensors: problems and performance. Proc. of a working conference on Current Measurement. Tech. Report DEL-SG-3-78, College of Marine Studies, Univ. Delaware, Newark, DE 19711, p. 9-33.

Mercier, J.A., 1973. Large amplitude oscillations of a circular cylinder in a low-speed stream. Stevens Institute of Technology, Hoboken, NJ, Ph.D. Dissertation, 134 pp.

Mero, T., G. Appell and R.S. McQuivey, 1977. Marine dynamics and its effect on current measuring transducers. NBS flow measurement symposium, February 23-25, Gaithersburg, MD.

Nakamura, Y. and Y. Tomonari, 1982. The effects of surface roughness on the flow past circular cylinders at high Reynolds numbers. J. Fluid Mech., v. 123, p. 363-378.

Naudascher, E. and C. Farell, 1970. Unified analysis of grid turbulence. Jour. Eng. Mech. Div., ASCE, v. 96, p. 121-141.

Nielsen, P. and P.J. Cowell, 1981. Calibration and data correction procedures for flow meters and pressure transducers commonly used by the Coastal Studies Unit. Coastal Studies Unit Tech. Report No. 81/1, Department of Geography, University of Sidney, Sidney, N.S.W. 2006, 27 pp.

Olson, J.R., 1972. Two component electromagnetic flow meter. Marine Tech. Society Journal, v. 6, p. 19-24.

Roshko, A., 1961. Experiments of the flow past a circular cylinder at very high Reynolds number. J. Fluid Mech., v. 10, p. 345-356.

Schlichting, H., 1968. Boundary-layer theory, 6th edition. McGraw-Hill Book Co., New York, NY, 748 pp.

Seymour, R., 1974. Resistence of spheres in oscillatory flows. Ph.D. Dissertation, Univ. of Calif., San Diego, 86 pp.

Shercliff, J.A., 1962. The theory of electromagnetic flow measurement. Cambridge University Press, New York, NY.

Smith, J.D., 1978. Measurement of turbulence in oceanic boundary layers. Proc. of a working conference on Current Measurement. Tech. Report DEL-SG-3-78, College of Marine Studies, Univ. Delaware, Newark, DE 19711, p. 95-128.

Stratford, B., 1959. The prediction of separation of the turbulent boundary layer. J. Fluid Mech., v. 5, p. 1-16.

Tan-Atichat, J., H.M. Nagib, and R.I. Loehrke, 1982. Interaction of
free-stream turbulence with screens and grids: a balance between
turbulence scales. J. Fluid Mech., v. 114, p. 501-518.

Tani, I. and H. Sato, 1956. J. Phys. Soc. of Japan, v. 11, p. 1284-1291.

Tani, I., 1969. Boundary-layer transition. Annual Review of Fluid Mechanics,
v. 1, p. 169-196.

Tani, I., R. Hama and S. Mituisi, 1940. Aeron. Res. Inst., Tokyo Imp. Univ.,
Report 199.

Townsend, A.A., 1962. The behavior of a turbulent boundary layer near
separation. J. Fluid Mech., v. 12, p. 536-

Vennard, J.K. and R.L. Street, 1975. Elementary Fluid Mechanics. John Wiley
and Sons, NY.

Williams, A.J. and J. Tochko, 1977. An acoustic sensor of velocity for
benthic boundary layer studies. In Bottom Turbulence, J.C.J. Nihoul
(ed.), Elsevier, NY, p. 83-97.

Williams, E.J., 1930. The induction of electric currents in a moving liquid
by magnetic fields and its application to blood flow. Proc. Phys. Soc.
(London), A42, p. 466-483.

Wooding, R.A., E.F. Bradley and J.K. Marshall, 1973. Drag due to regular
arrays of roughness elements of varying geometry. Boundary-layer
meteorology, v. 5, p. 285-308.

Yalin, M.S., 1972. Mechanics of sediment transport. Pergamon Press, NY,
290 pp.

APPENDIX I

ANALYSIS OF THE BLOCKAGE BEHIND GRIDS

Calculations of the magnitude of possible blockage behind a towed grid can be made in analogy to ideal propellor theory (e.g., Vennard and Street, 1975).

We consider steady, 2-D flow past a porous grid: Far upstream of the grid the pressure is p_∞ and the velocity is u_∞. The drag created by the grid causes the streamlines to diverge around the grid. The ideal flow theory applies upstream and a short distance downstream of the grid. Farther downstream the flow approximates a 2-D turbulent wake.

To analyze the flow consider "dividing streamlines" as shown:
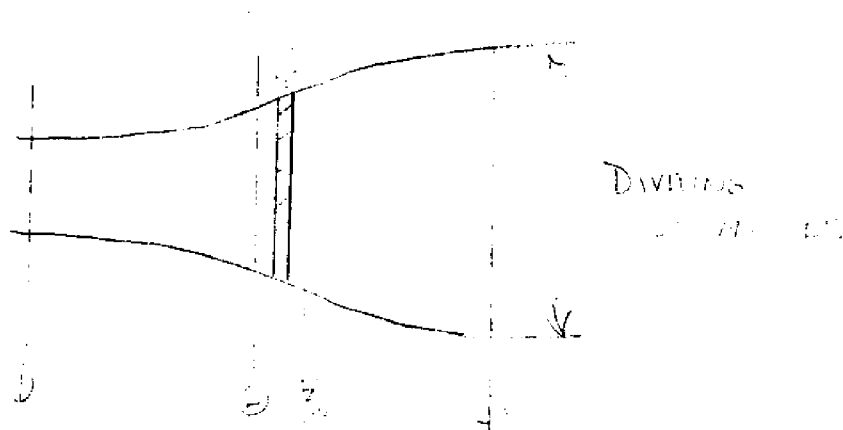
At station 1, the pressure is equal to p_∞ and the velocity is equal to u_∞. At station 4, there is no curvature in the streamlines and the pressure must therefore be equal to the ambient pressure, p_∞. The velocity at station 4 is less than u_∞. Somewhere beyond station 4, the ideal theory ceases to apply, turbulent lateral transport of momentum becomes important, and a turbulent wake analysis is appropriate.

Conservation of mass requires that $u_2 = u_3$. Application of the momentum principle between stations 2 and 3 yields

$$p_2 - p_3 = \tfrac{1}{2} C_D \rho u_2{}^2 \tag{1}$$

where ρ is the water density and C_D is the drag coefficient of the grid.

Application of the momentum principle between stations 1 and 4 yields approximately

$$\rho Q u_1 - \tfrac{1}{2} C_D \rho u_2{}^2 L = \rho Q u_4 \tag{2}$$

where L is the length of the grid and Q is the flow rate per unit depth passing between the dividing streamlines. The pressure forces acting on the control volume have been neglected in equation 2 because they are presumably small compared to the momentum fluxes.

Conservation of mass requires that $Q = u_2 L$, and under previous assumptions $u_1 = u_\infty$. Equation 2 therefore becomes

$$(u_\infty - u_4) = \tfrac{1}{2} C_D u_2. \tag{3}$$

Application of Bernoulli's equation between sections 1 and 2 and between sections 3 and 4 yields

$$p_\infty + \tfrac{1}{2}\rho u_\infty{}^2 = p_2 + \tfrac{1}{2}\rho u_2{}^2 \tag{4}$$

$$p_\infty + \tfrac{1}{2}\rho u_4{}^2 = p_3 + \tfrac{1}{2}\rho u_3{}^2. \tag{5}$$

The difference between equations 4 and 5 is

$$\tfrac{1}{2}\rho(u_\infty{}^2 - u_4{}^2) = p_2 - p_3 \tag{6}$$

where the fact that $u_2 = u_3$ has been used. Combining equations 6 and 1, we have

$$(u_\infty{}^2 - u_4{}^2) = C_D u_2{}^2. \tag{7}$$

130

Substitution of equation 7 into equation 3 yields finally

$$\frac{u_4}{u_\infty} = \frac{1 - \frac{1}{4}C_D}{1 + \frac{1}{4}C_D} \qquad (8)$$

The application of Bernoulli's equation between sections 3 and 4 seems questionable, but the corresponding analysis for propellors apparently works well. The inertia terms in the momentum equation must be large compared to the stress terms between sections 3 and 4, so that the flow is effectively inviscid.

The above analysis works well when the porous grid is replaced by a series of closely spaced jets directed against the flow. The jets approximate a line source of momentum and their effect on the flow is completely analagous to that of the drag on the grid.

Batchelor (An Introduction to Fluid Dynamics, p. 375) obtains the following simple expression for the drag coefficient of a porous plate:

$$C_D = \left(\frac{1 - \beta}{\beta} \right)^2 \qquad (9)$$

where ß = open area/total area. Using equations 8 and 9, we obtain:

GRID   1   ß = 0.59 C_D = 0.483 $\frac{u_4}{u_\infty}$ = 0.785

GRID   2   ß = 0.86 C_D = 0.0265 $\frac{u_4}{u_\infty}$ = 0.987

Experiments indicate that station 4 occurs at a downstream distance from the grid of order L. Further downstream, the velocity is expected to change gradually back to u_∞. Especially near the centerline, this change is very

gradual, so that u_4 is a good estimate of the centerline velocity for a reasonably long region downstream of the grid, so u_4 is assumed to be a good estimate of the actual velocity at the sensor during the tests, where the cart speed is u_∞.

For grid 1, we found a reduction in sensitivity of 24%, which corresponds nearly exactly to the prediction of $u_4/u_\infty = 0.785$, or $1 - u_4/u_\infty = 0.22$. It therefore appears that nearly all of the reduction in sensitivity is due to flow blockage, given this simple analysis.

For grid 2, we found a reduction in sensitivity of 45%, which clearly cannot be explained by flow blockage.

All calculations indicate that the turbulence intensity produced by grid 2 was higher than the turbulence intensity produced by grid 1. Therefore, the reduction in sensitivity for grid 2 is consistent with a source in ambient turbulence, while the reduction for grid 1 was produced by flow blockage.

APPENDIX 2

SAMPLE REGRESSION PLOTS

Seventeen sample plots of various calibration tests are presented to illustrate the experimental scatter in results. All examples presented are for the same current meter (S563), a MM551M with probe diameter of 4 cm. Samples cover pure steady tests, pure oscillatory tests, combined steady/ oscillatory tests, as well as grid turbulence and horizontal cosine response experiments.
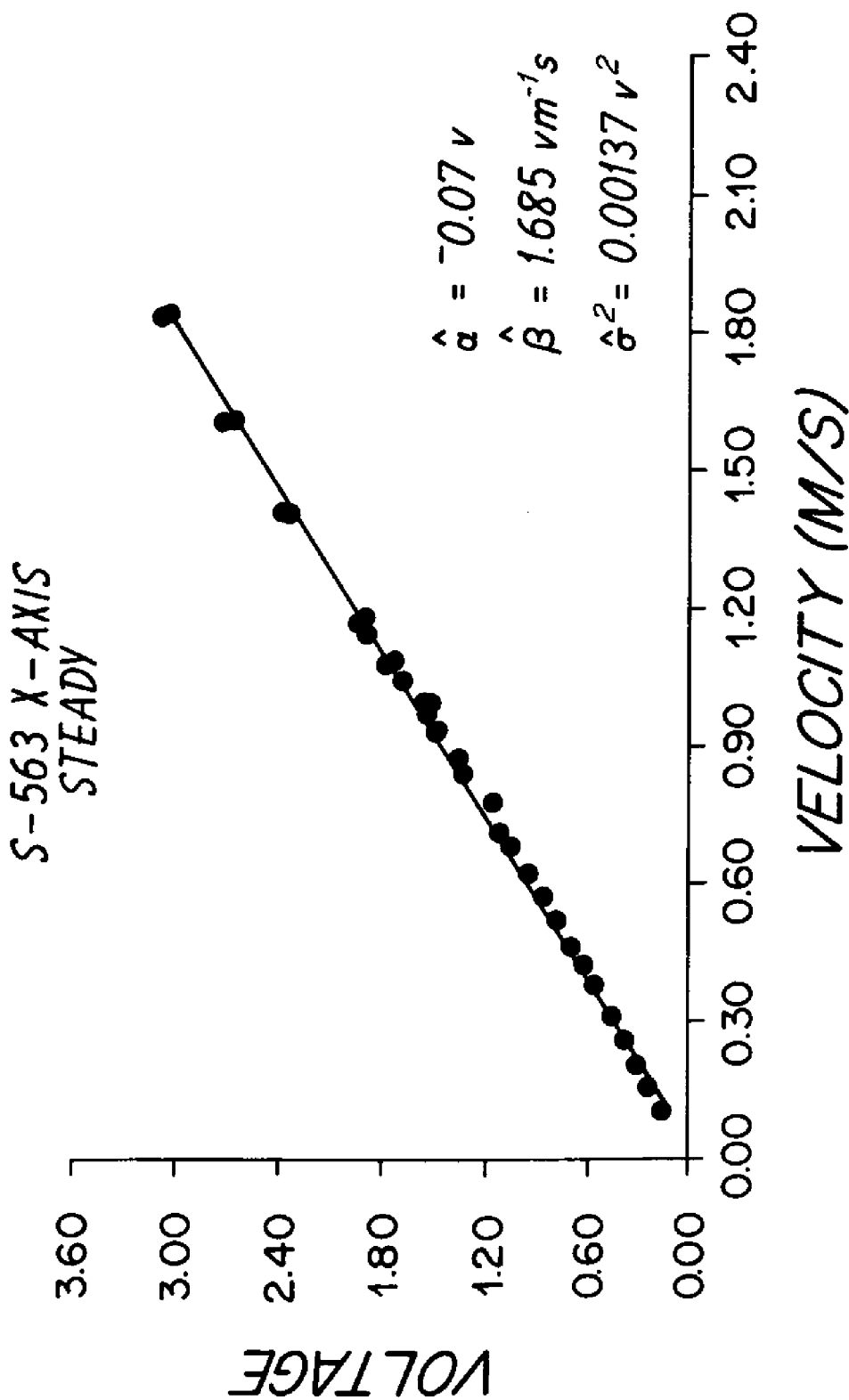
Figure A-1   Output voltage versus tow velocity for x-axis of S563 for pure
steady conditions. As in following figures, regression
estimates of fit are indicated on the figure; specific informa-
tion can also be obtained from tables in the body of the report.
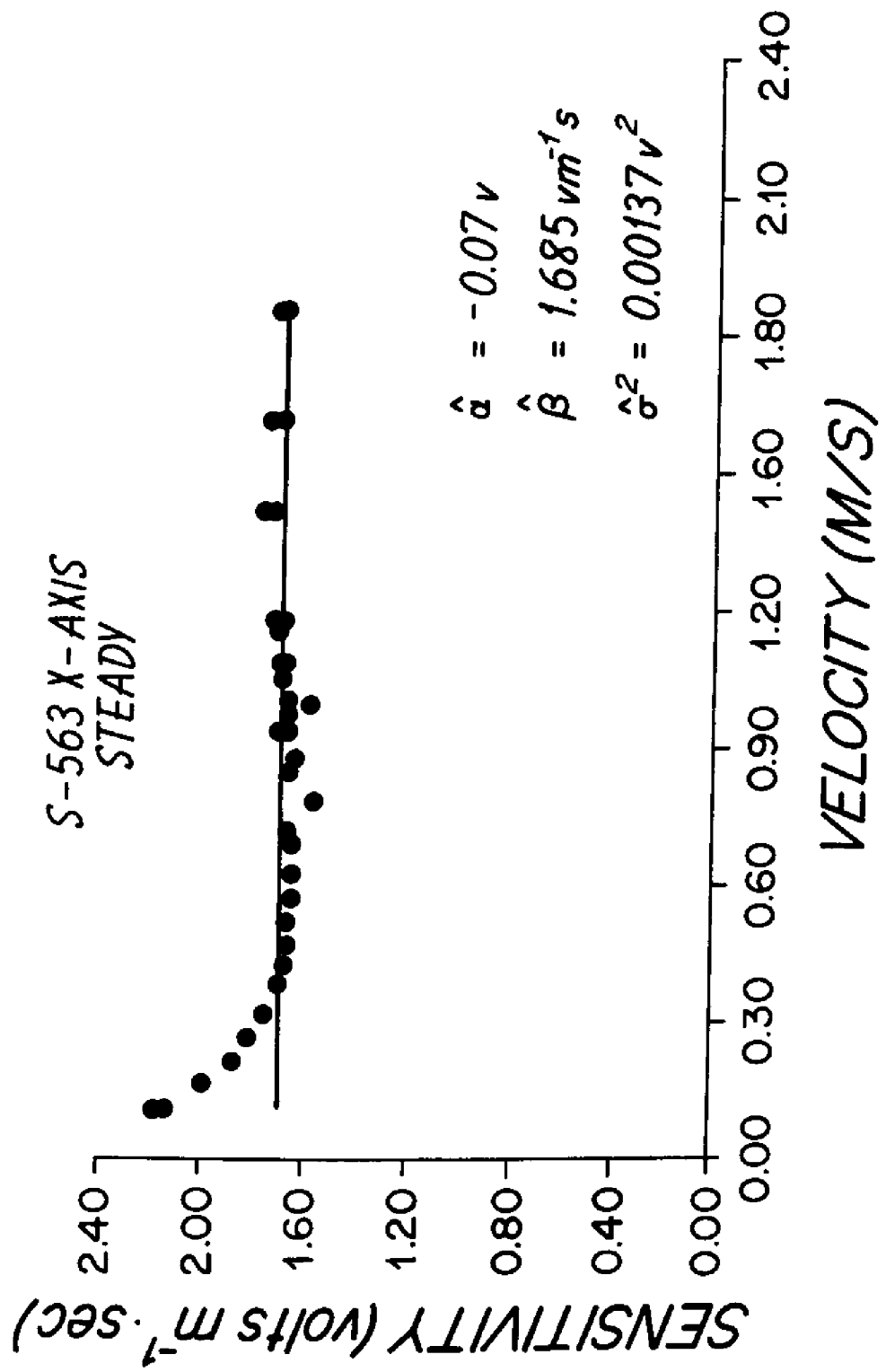
Figure A-2   Steady sensitivity versus tow velocity for same test as in A-1.
Deviation from best fit indicated at low velocities is due to
non-linear sensitivity at low velocities.

Figure A-3   Model 2 results for the same tow tests of the previous figures, with a critical velocity of 0.8 m/sec (representing the smallest error variance of any critical velocity).

136
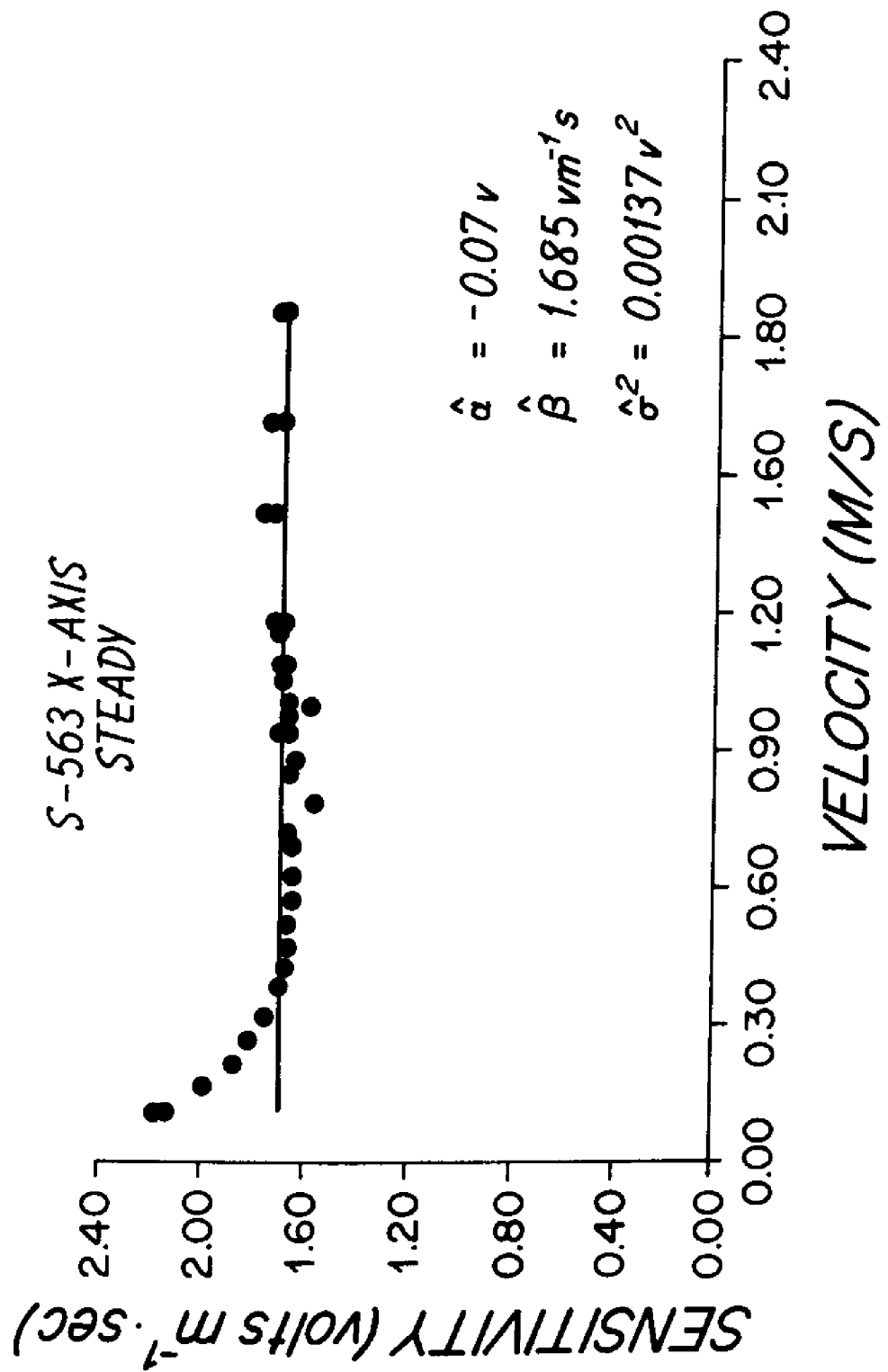
Figure A-2   Steady sensitivity versus tow velocity for same test as in A-1.
Deviation from best fit indicated at low velocities is due to
non-linear sensitivity at low velocities.

Figure A-3   Model 2 results for the same tow tests of the previous figures, with a critical velocity of 0.8 m/sec (representing the smallest error variance of any critical velocity).
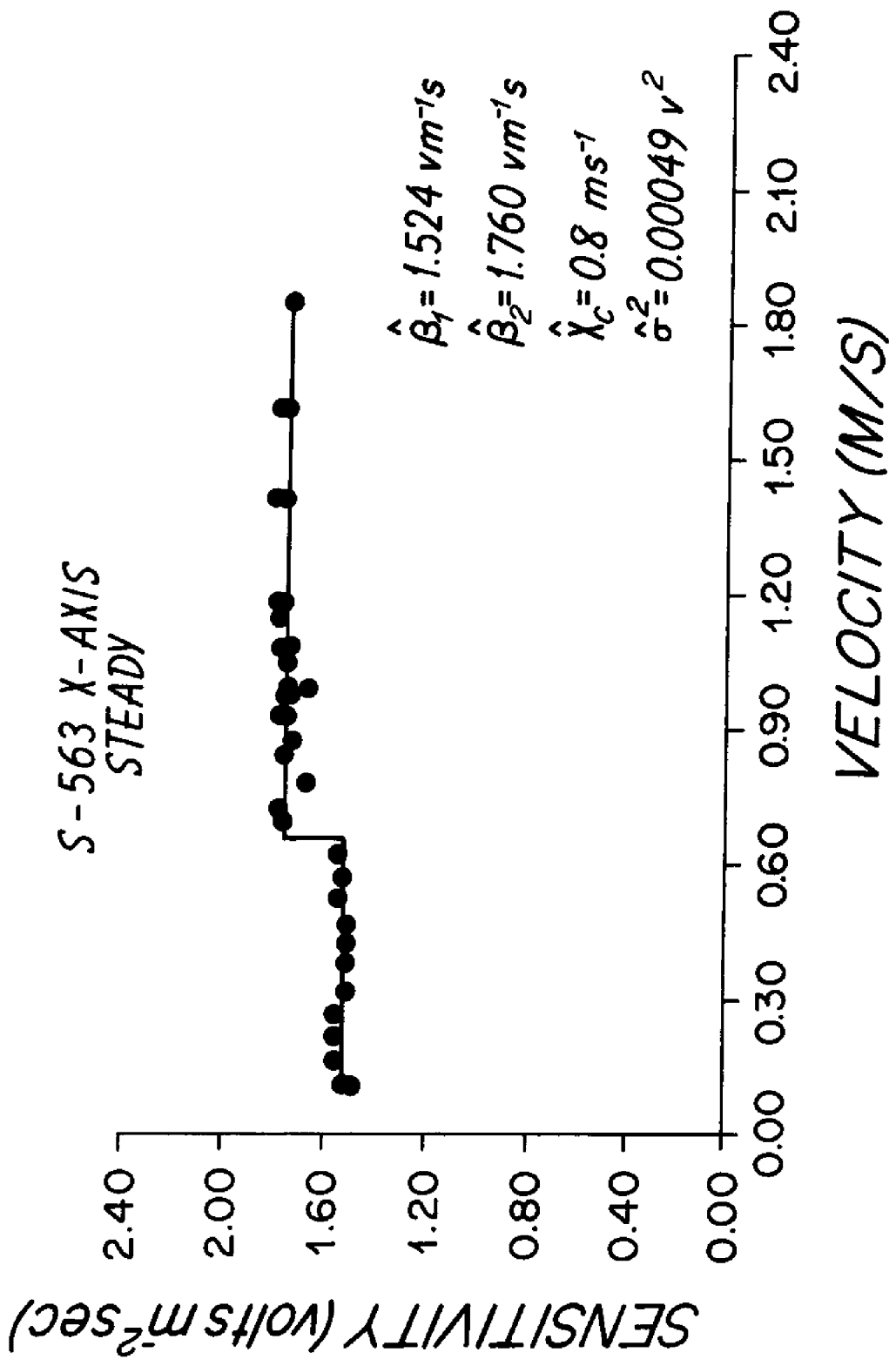
Figure A-4 Sensitivity versus tow velocity for tests shown in A-3, where two-segment fit has eliminated the poor low velocity response of the instrument.

S-563 X-AXIS
PURE OSCILLATORY

$\hat{\alpha} = 0.02\ v$

$\hat{\beta} = 1.695\ vm^{-1}s$

$\hat{\sigma}^2 = 0.000014\ v^2$
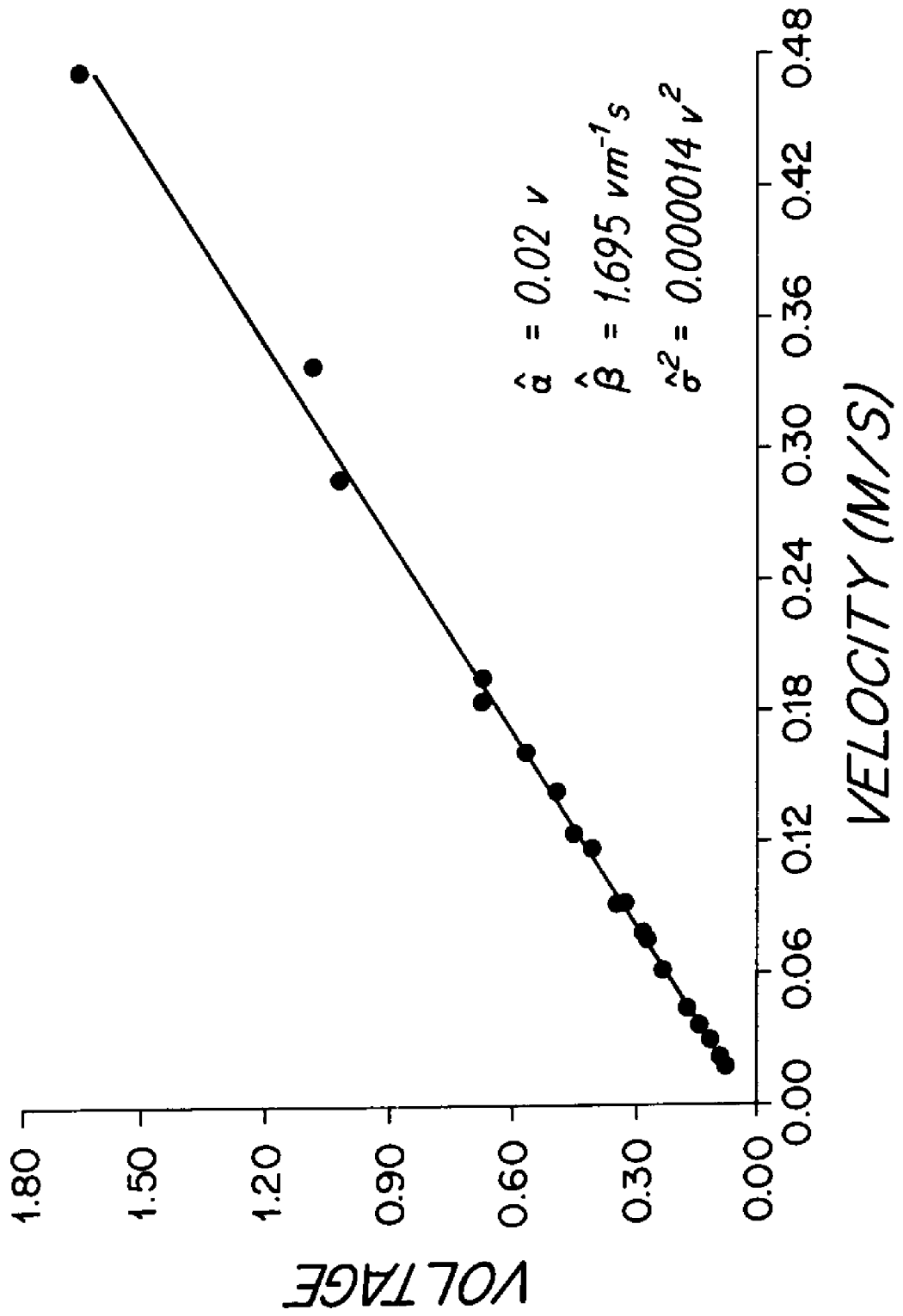
Figure A-5   Output voltage versus peak orbital velocity for pure oscillatory flow.
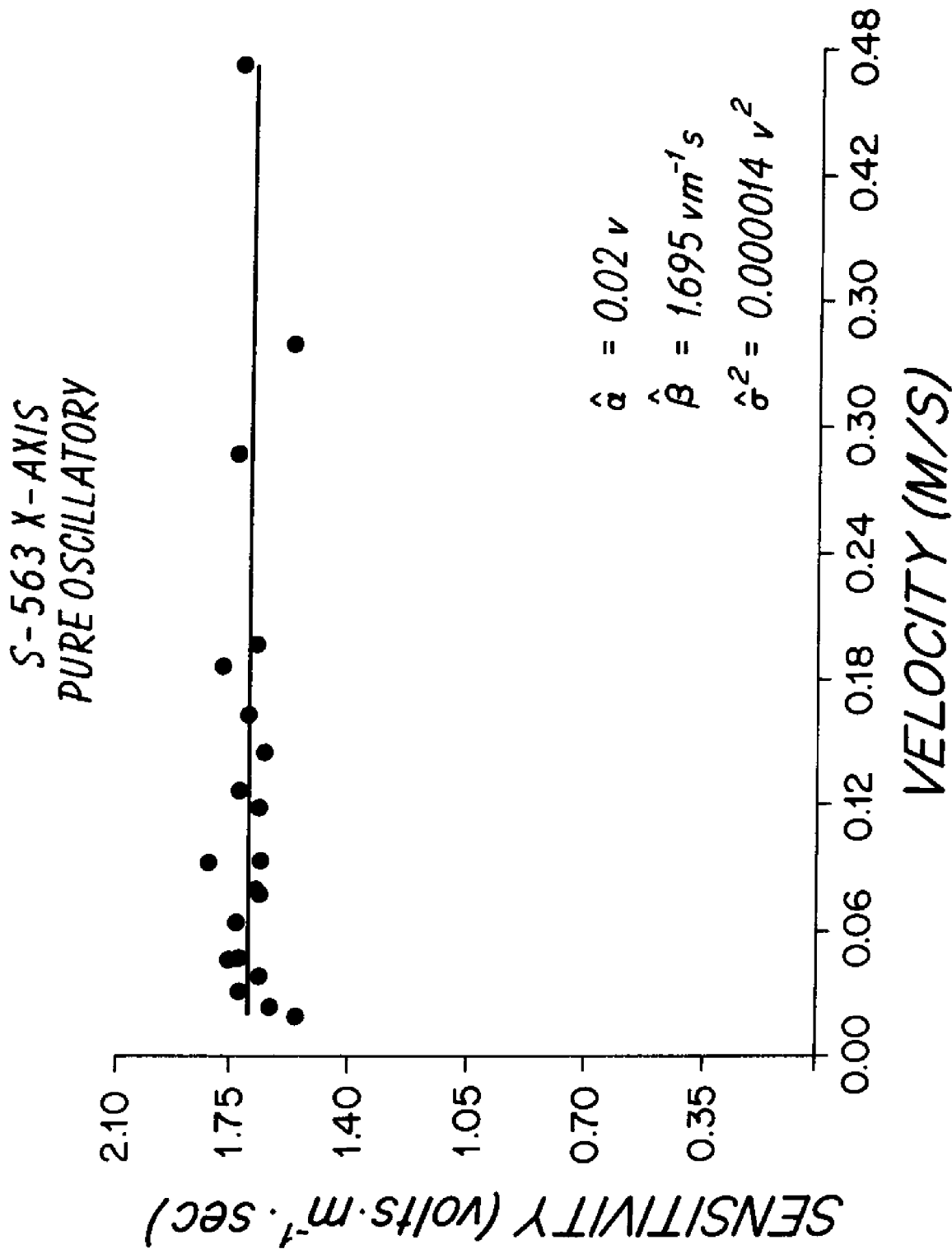
Figure A-6   Oscillatory sensitivity versus peak orbital velocity for the case presented in A-5.

139
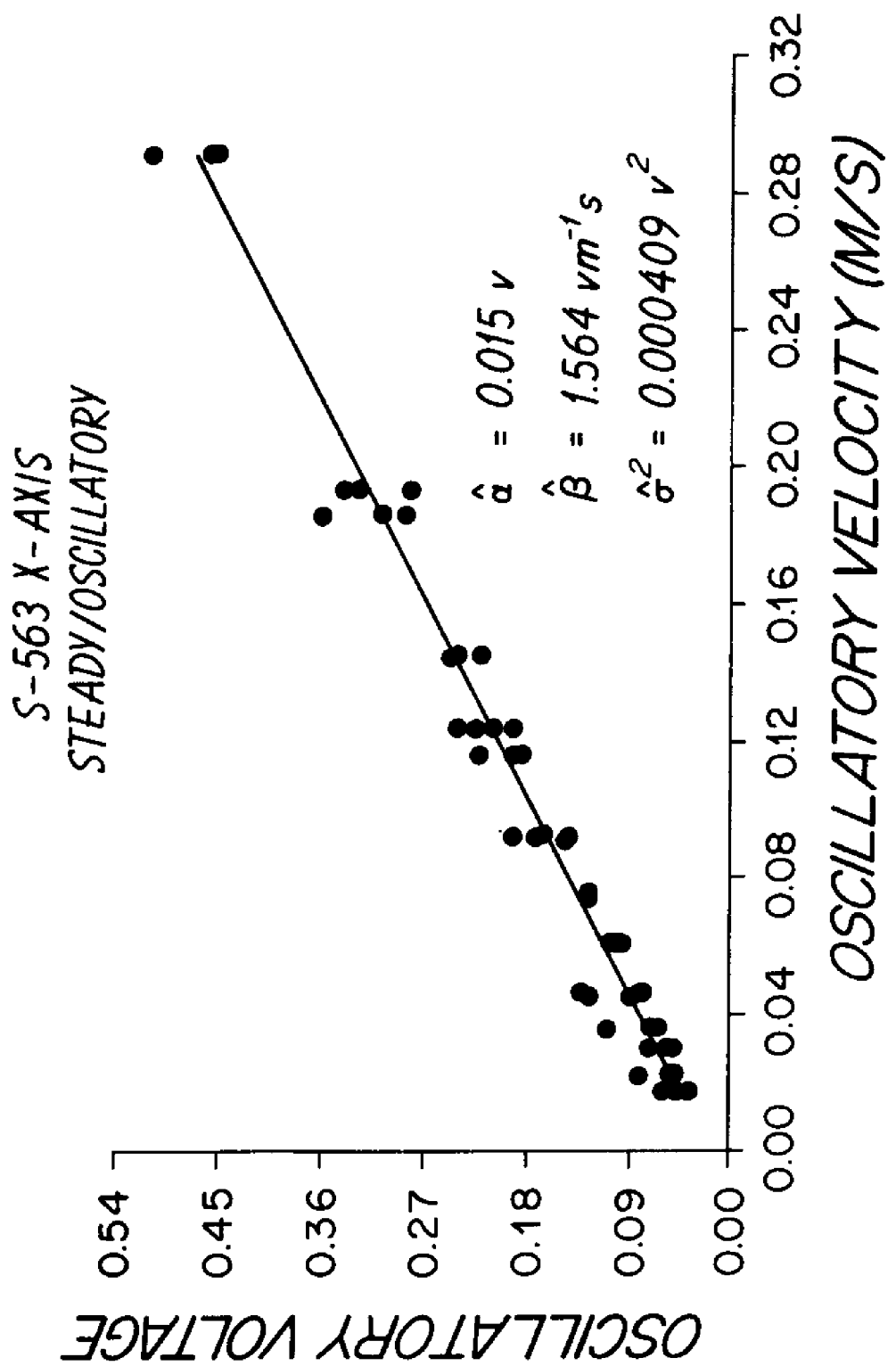
Figure A-7   Oscillatory voltage versus peak oscillatory velocity under
combined steady/oscillatory flow conditions. Although the
regression is excellent, the sensitivity is lower than in the
pure oscillatory case.
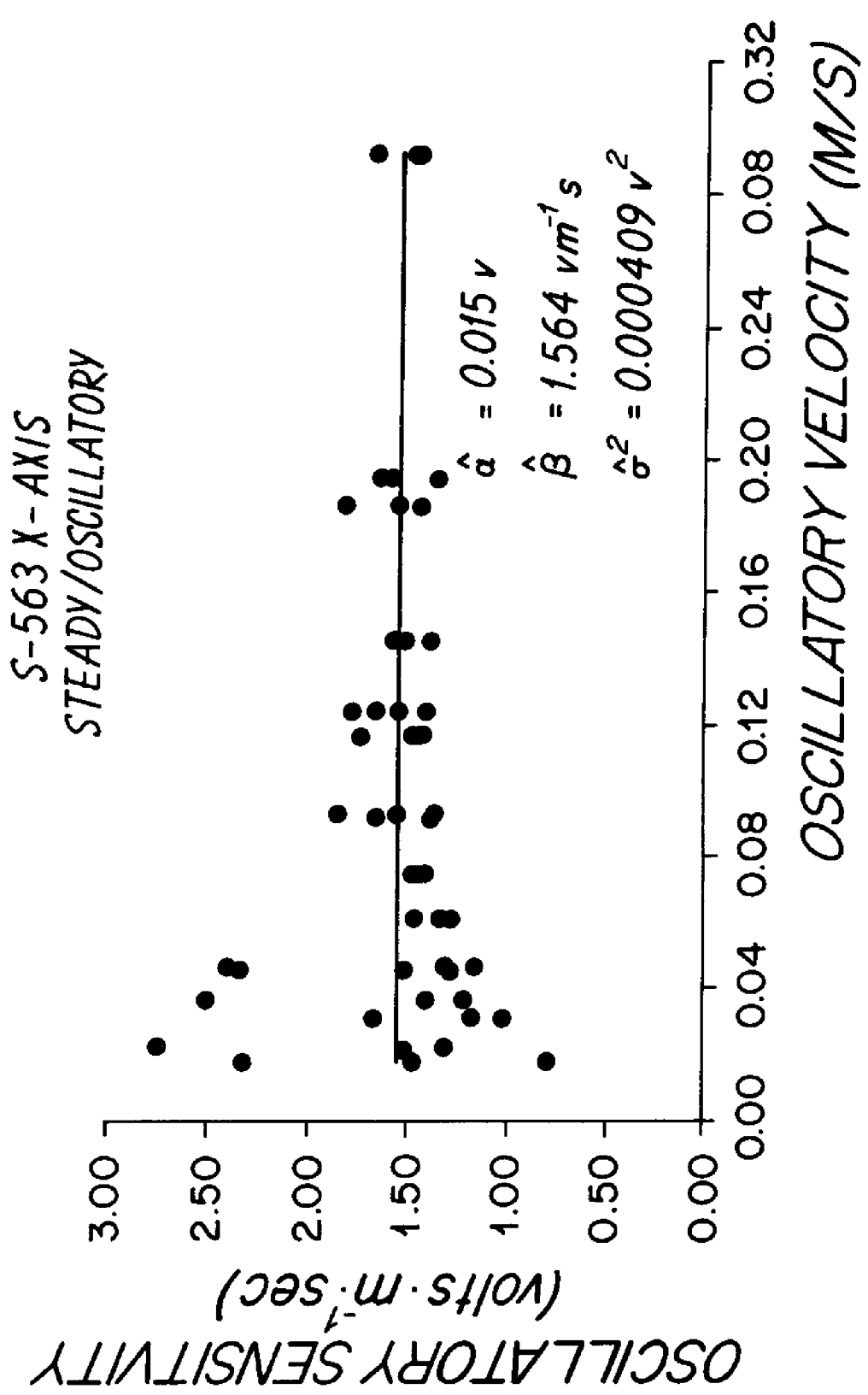
Figure A-8   Oscillatory sensitivity versus peak oscillatory velocity under
conditions described in A-7. Note considerable scatter at low
velocities, where the ratio UT/A is large (large steady velocity
as compared to oscillatory velocity).
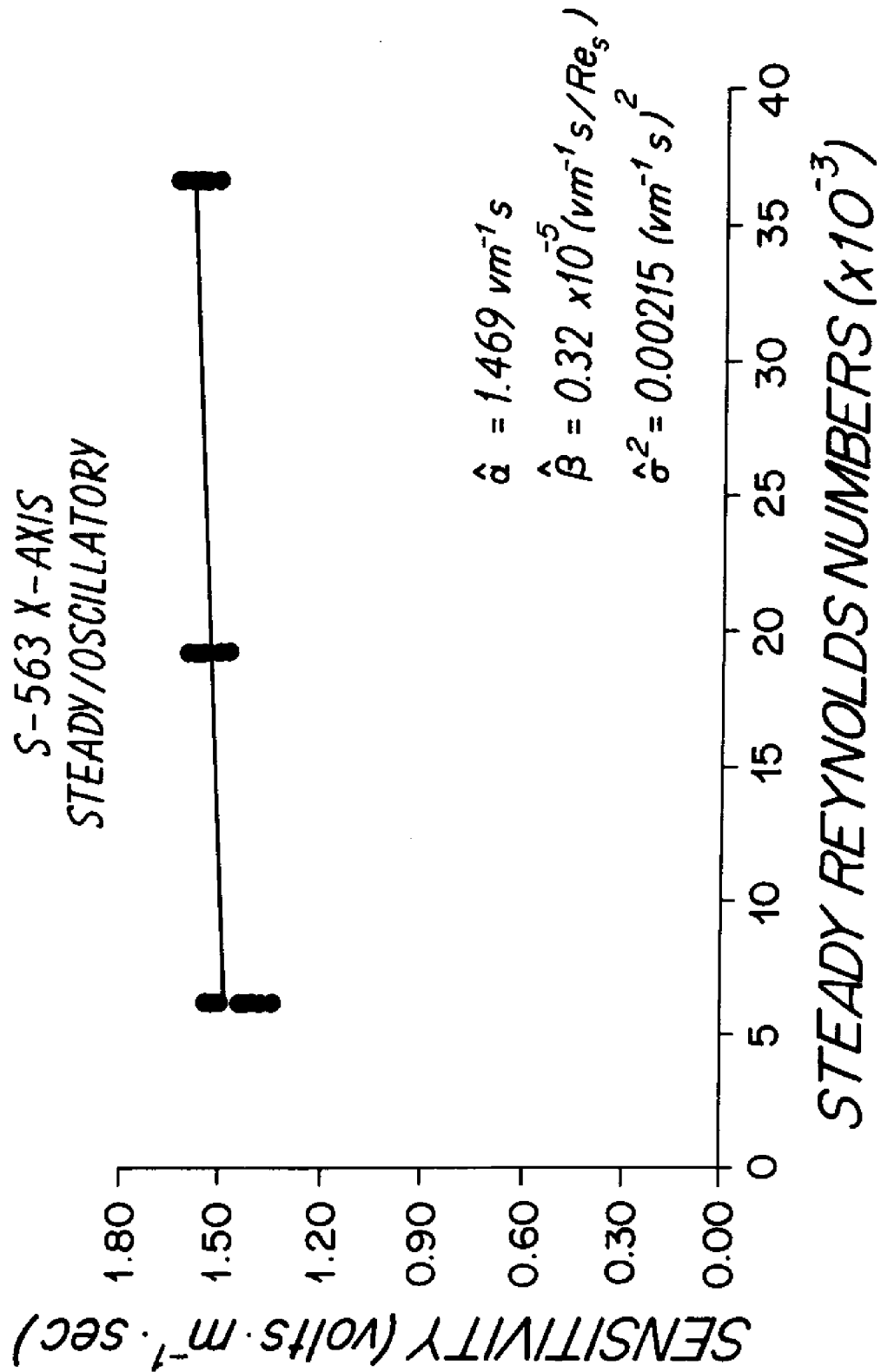
Figure A-9   Steady sensitivity as a function of steady Reynold's number for combined steady/oscillatory flow conditions. Sensitivity increases with Re.
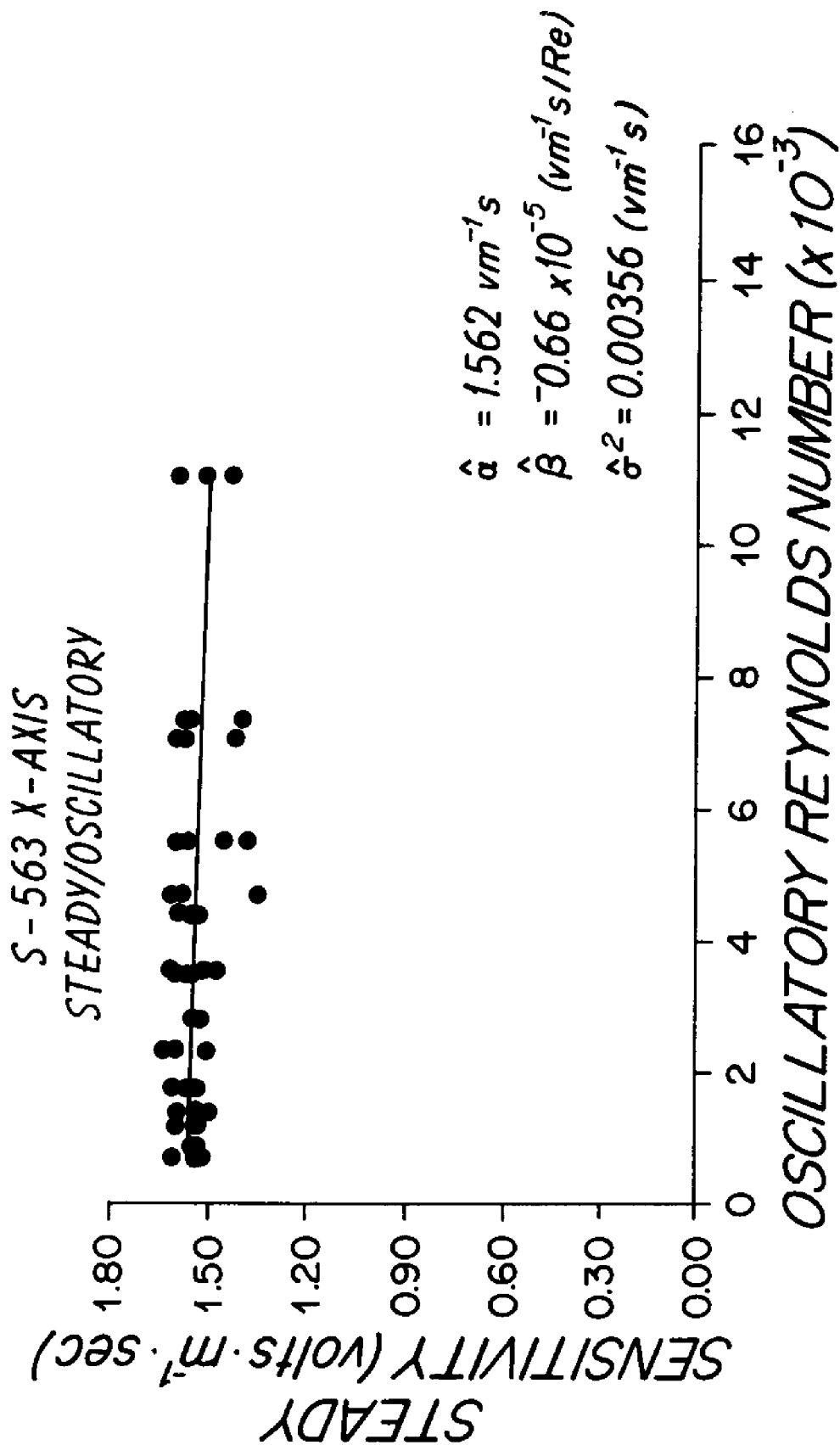
Figure A-10   Steady sensitivity versus oscillatory Reynold's number for
               combined steady/oscillatory flow conditions. This regression
               fit is not significantly different from zero.
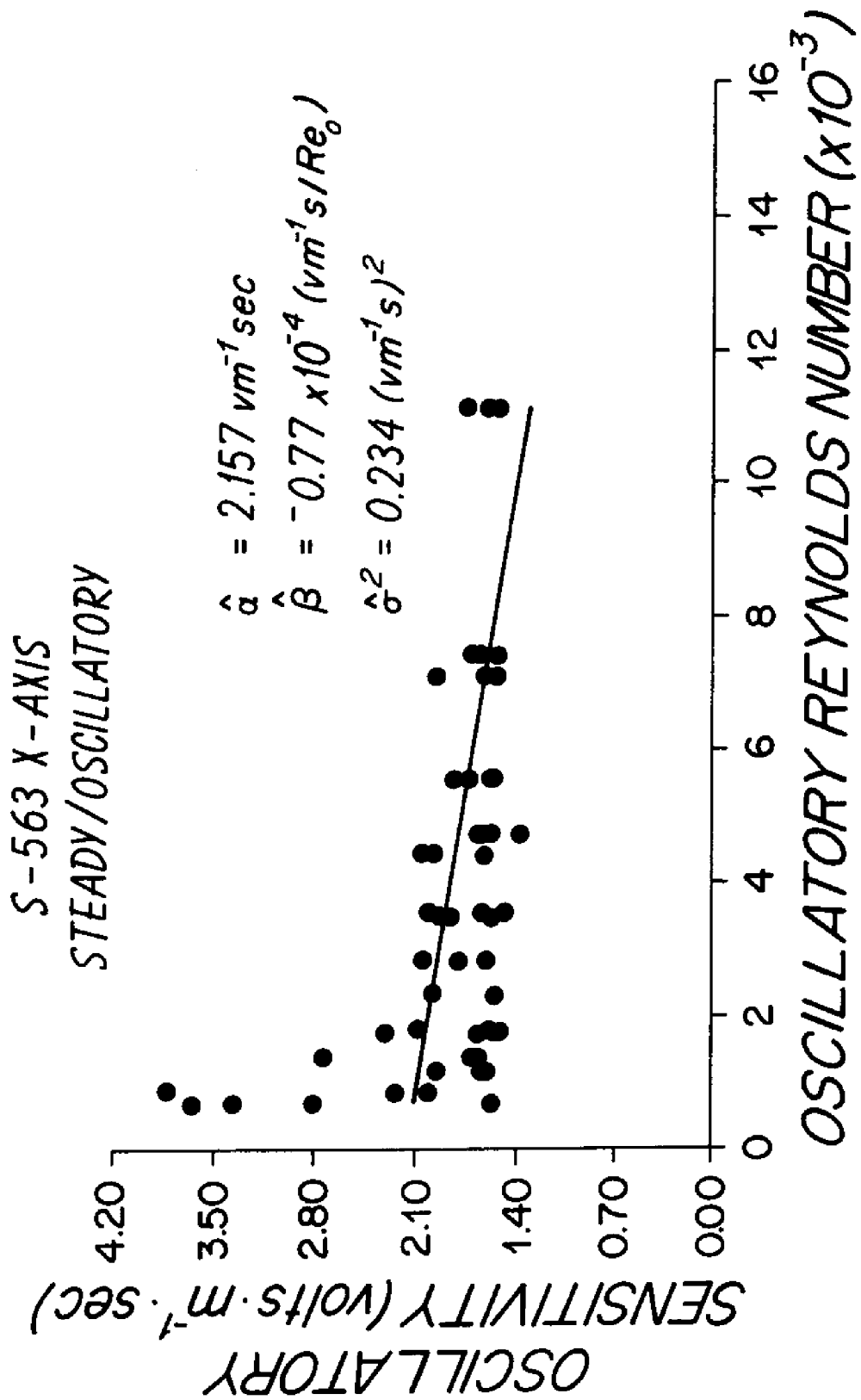
Figure A-11   Oscillatory sensitivity versus oscillatory Reynold's number for combined steady/oscillatory flow conditions.   Sensitivity decreases increasing $(Re)_0$, consistent with the hypothesis that wake structure may affect sensitivity.   Most scatter is at low values of $(Re)_0$.
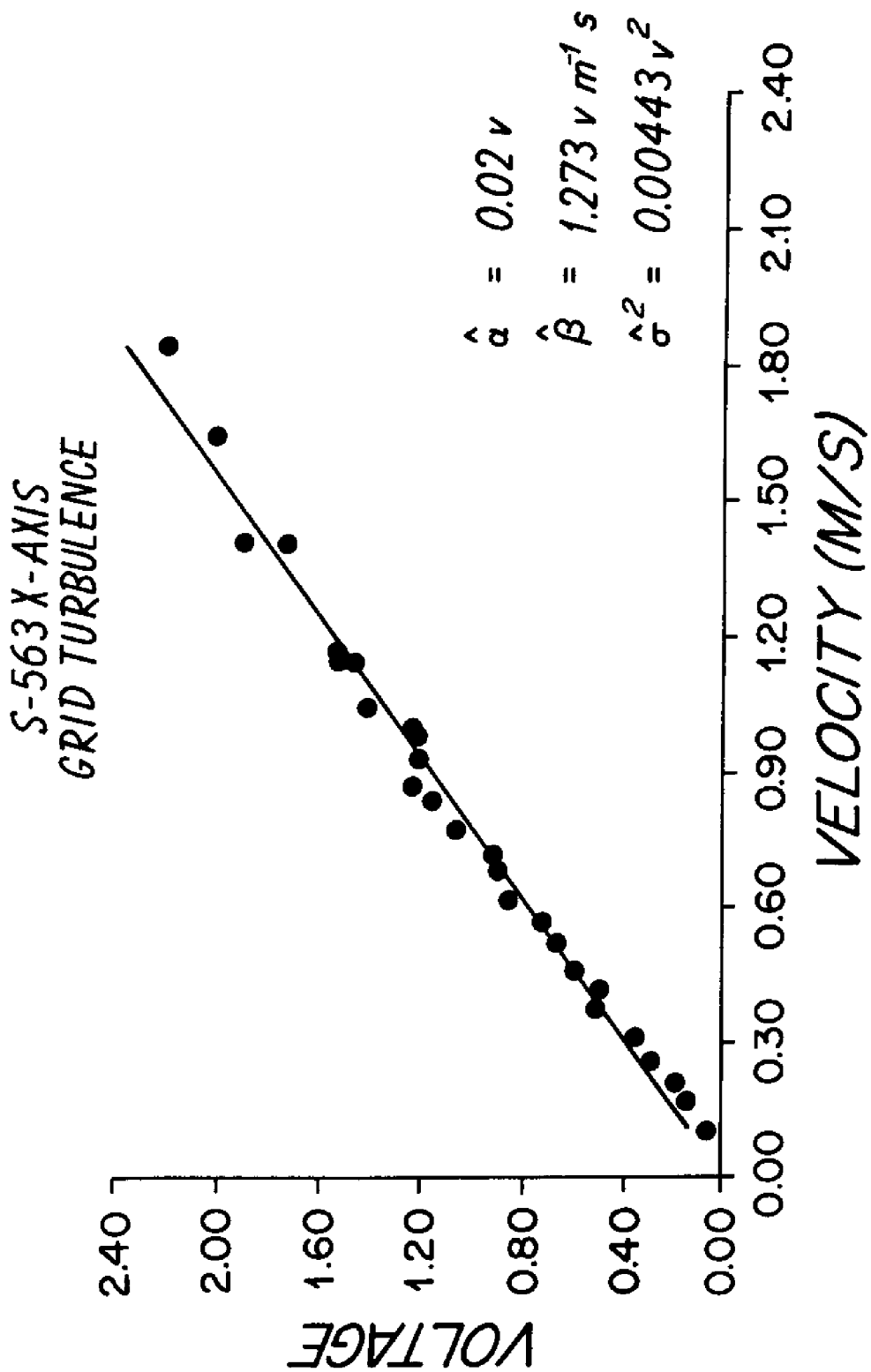
Figure A-12   Output voltage versus tow velocity behind Grid 1 turbulence.
Scatter is low, as is sensitivity compared with the pure steady
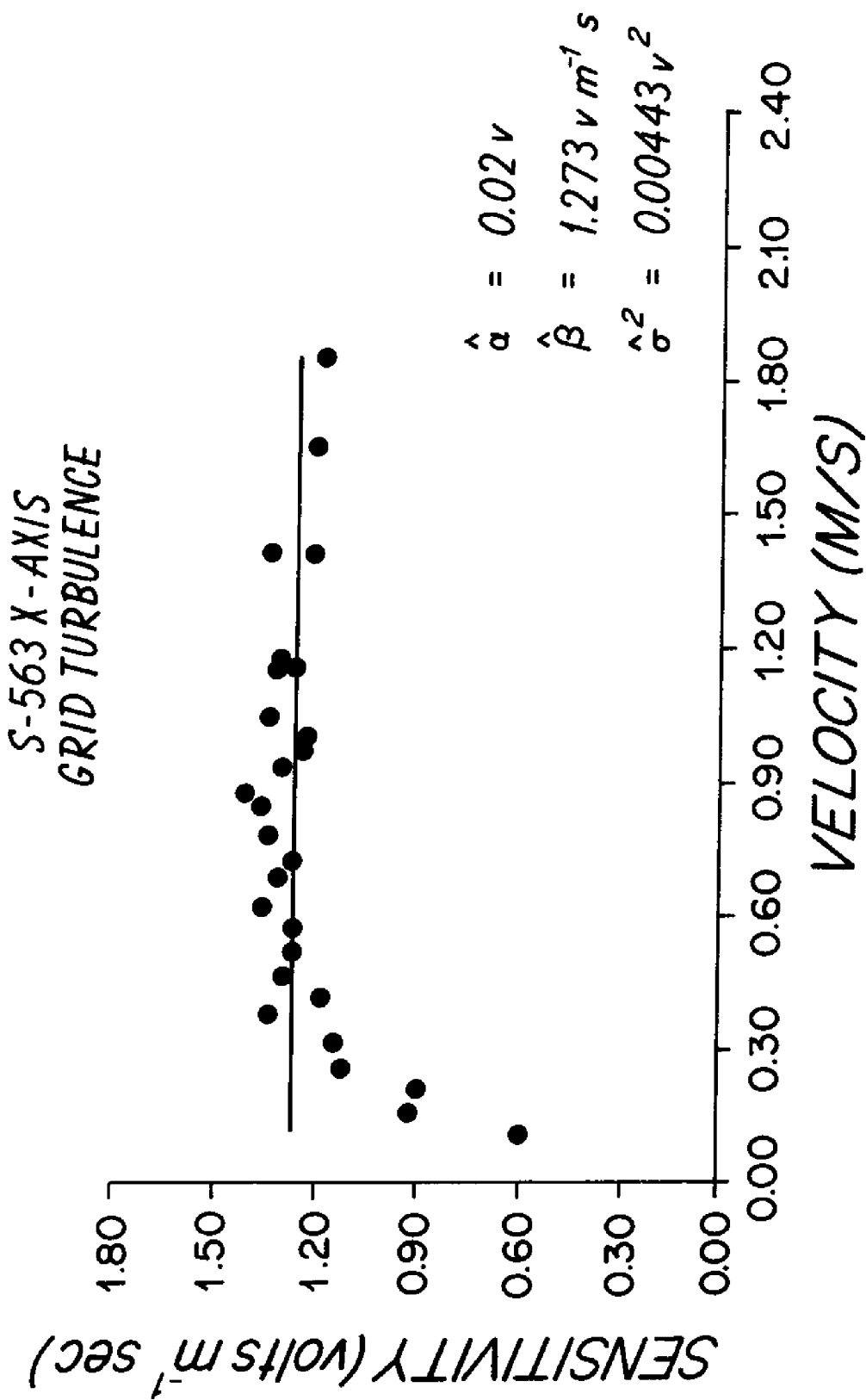case. This decrease in sensitivity can be explained by flow
blockage.

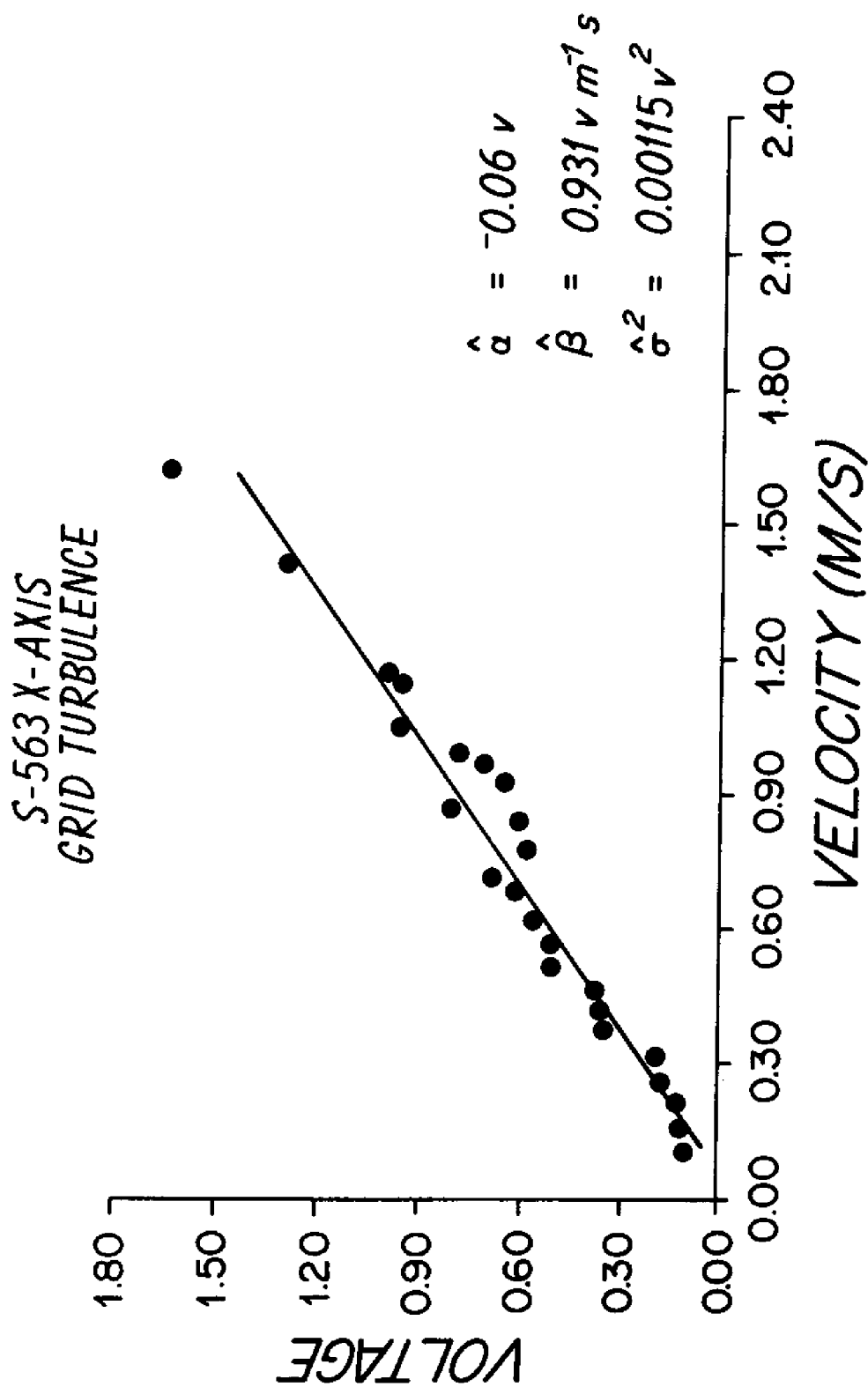Figure A-13   Sensitivity versus tow velocity for the case described in A-12.

Figure A-14   Output voltage versus tow velocity behind Grid 2 turbulence.
Scatter is relatively low, while sensitivity is much decreased
compared to pure steady conditions.   This decrease cannot
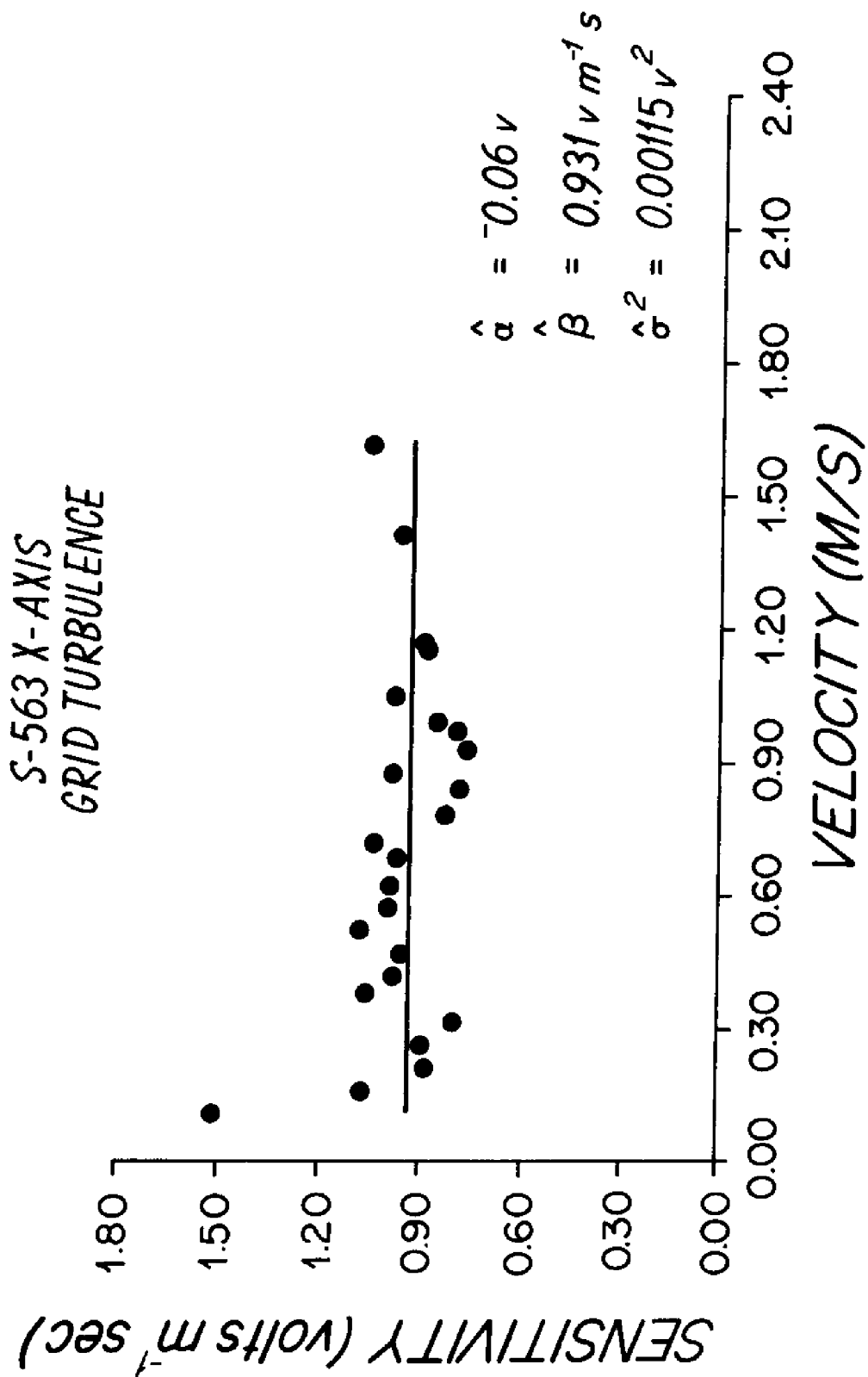readily be explained by flow blockage.

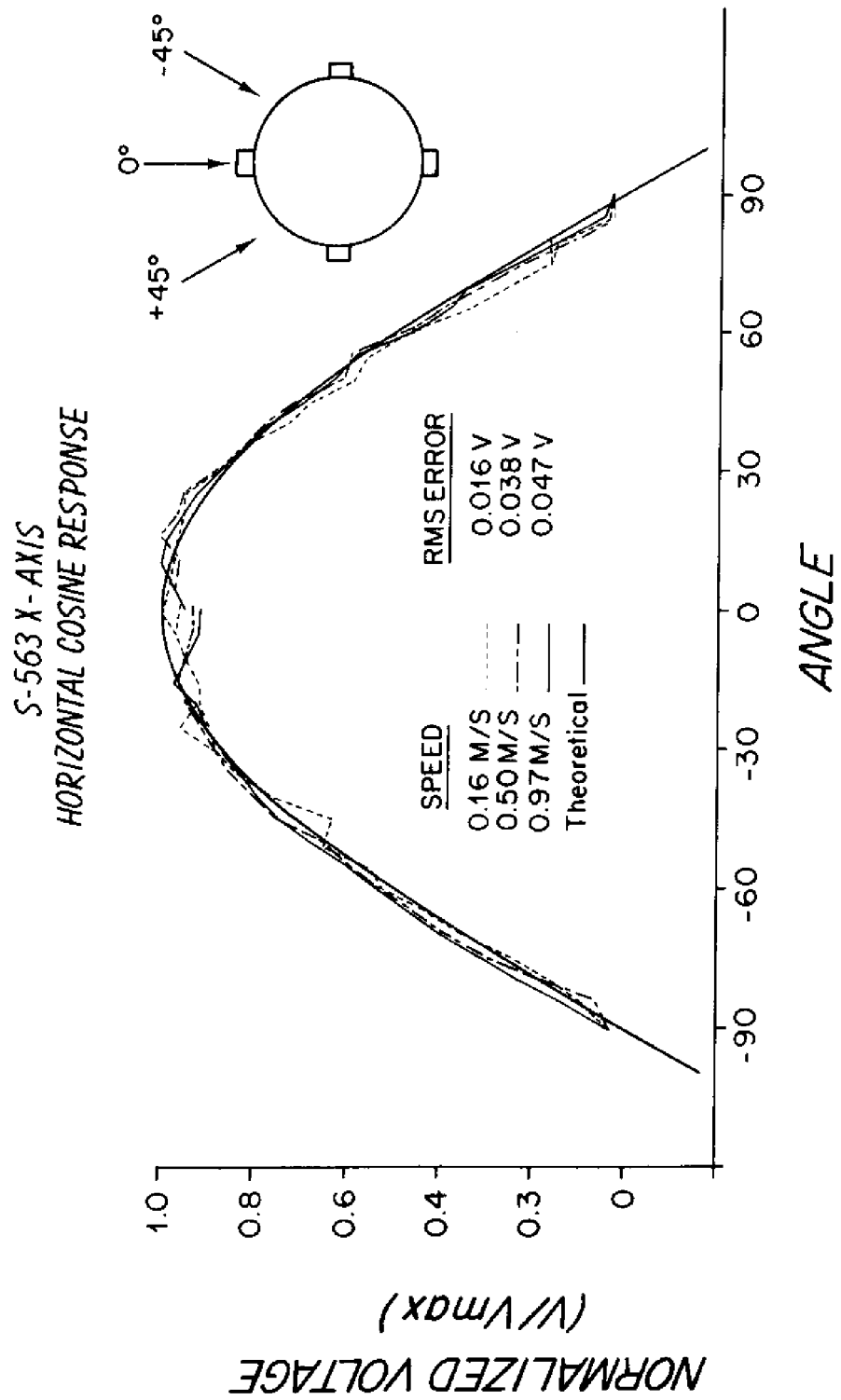Figure A-15   Sensitivity versus tow velocity for the case described in A-14.

Figure A-16   Horizontal angular response for S563, x-axis, at three different tow speeds. Note "shoulder" about the 0° flow direction indicative of asymmetry of roughness distribution on sphere at low angle of attack.
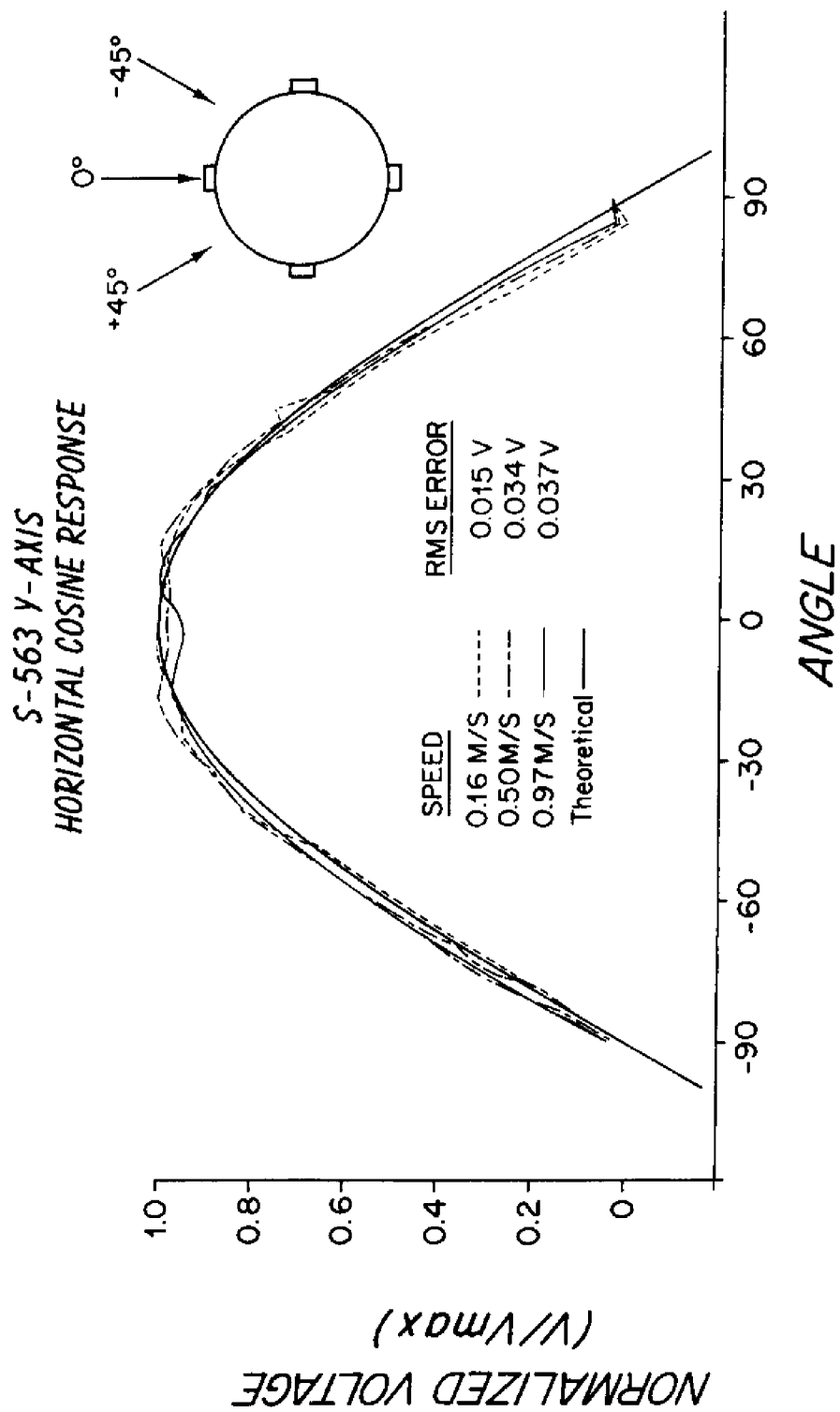
Figure A-17   Horizontal angular response for S563, y-axis, at three different
tow speeds. Note "shoulder" about the 0° flow direction indica-
tive of asymmetry of roughness distribution on sphere at low
angle of attack.

REPORT DOCUMENTATION PAGE	1. REPORT NO. WHOI-84-20	2.	3. Recipient's Accession No.

4. Title and Subtitle	5. Report Date
Dynamic Response of Electromagnetic Current Meters	May 1984
	6.

7. Author(s) David G. Aubrey, Wayne D. Spencer, John H. Trowbridge	8. Performing Organization Rept. No. WHOI-84-20

9. Performing Organization Name and Address	10. Project/Task/Work Unit No.
Woods Hole Oceanographic Institution Woods Hole, Massachusetts 02543	11. Contract(C) or Grant(G) No. (C) DACW/2-82-C-0014 (G) NA80-AA-D-00077

12. Sponsoring Organization Name and Address U. S. Army Corps of Engineers, Coastal Engineering Research Center, Waterways Experiment Station, Vicksburg, Ma; and the NOAA National Office of Sea Grant	13. Type of Report & Period Covered Technical
	14.

15. Supplementary Notes

This report should be cited as: Woods Hole Oceanog. Inst. Tech. Rept. WHOI-84-20.

16. Abstract (Limit: 200 words)

The dynamic response of electromagnetic current meters (manufactured by Marsh-McBirney, Inc.) has been clarified through a comprehensive laboratory measurement program combined with a thorough literature review. Since flow past a spherical body has considerable hydrodynamic complexity for different dynamic conditions, a careful laboratory study was carried out for pure steady, pure oscillatory (horizontal plane), and combined steady/oscillatory conditions at two test facilities. Test results indicate that flowmeter behavior under pure steady flow is excellent in the absence of high levels of free-stream turbulence, with an r. m. s. error of 1 - 5 cm/sec. Pure oscillatory response was also excellent, with r. m. s. errors of 1 - 2 cm/sec. Combined steady/oscilatory flows degraded current meter performance with larger residual errors (1 - 6 cm/sec) and significant differences in sensitivity (up to 20 %). Horizontal cosine response showed systematic deviations from pure cosine behavior, with a notable inter-cardinal undersensitivity and cosine "shoulder" at lower Reynolds numbers. Error analysis shows these current sensors are adequate for many kinematic measurements, but may lead to excessive errors when using velocity to calculate dynamical quantities (such as bottom friction, Reynolds Stress, or log-layer friction velocities).

17. Document Analysis a. Descriptors

1. Current meters
2. Dynamic calibrations
3. Hydrodynamics

b. Identifiers/Open-Ended Terms

c. COSATI Field/Group

18. Availability Statement	19. Security Class (This Report) UNCLASSIFIED	21. No. of Pages 150
Approved for publication; distribution unlimited.	20. Security Class (This Page)	22. Price